UNIVERSITÀ DEGLI STUDI DI CATANIA
in convenzione con
UNIVERSITÀ DEGLI STUDI DI PALERMO

Dottorato di Ricerca in Scienza dei Materiali & Nanotecnologie
XXIX Ciclo

Maria José Lo Faro

# *Silicon Nanowires: the Route from Synthesis towards Applications*

Tutor: Prof. F. Priolo
Co-Tutor: Dott.ssa A. Irrera
Coordinatore: Prof.ssa M. G. Grimaldi

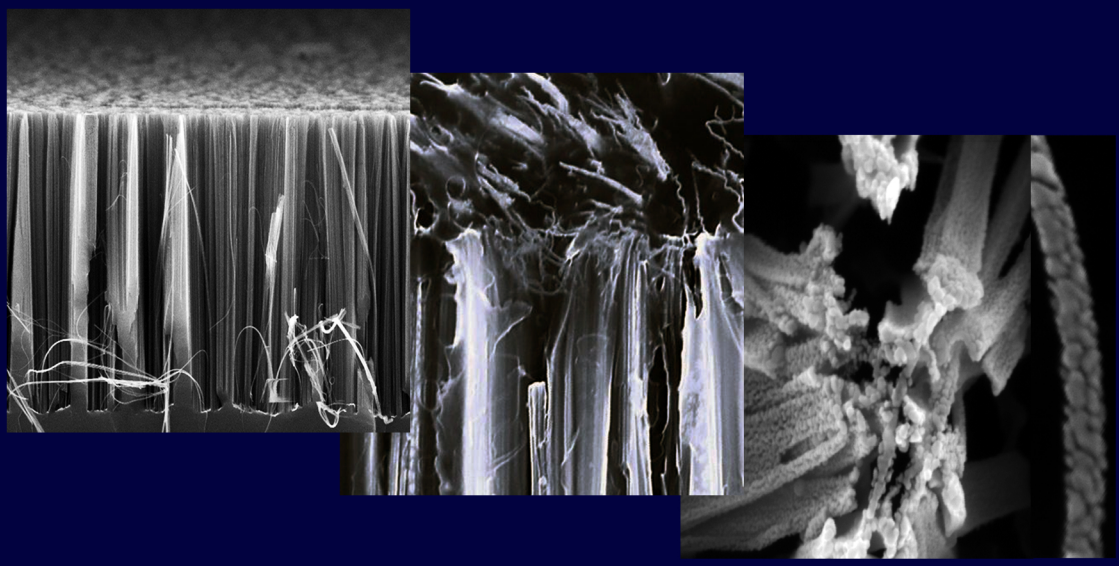

Università degli Studi di Catania
in convenzione con

Università degli Studi di Palermo

Dottorato di Ricerca in
Scienza dei Materiali e Nanotecnologie - XXIX Ciclo

Maria José Lo Faro

# Silicon Nanowires: the Route from Synthesis towards Applications

Tutor: Prof. F. Priolo
Co-Tutor: Dott.ssa A. Irrera
Coordinatore: Prof.ssa M. G. Grimaldi

Tesi per il conseguimento del titolo di Dottore di Ricerca

# Cover Page

**From left to right:**

Tilted cross-section scanning electron microscopy (SEM) displaying a dense and vertically oriented silicon nanowire array fabricated by metal assisted chemical etching.

Cross-section SEM microscopy depicting an hybrid system obtained embedding a carbon nanotube (CNT) dispersion in a Si NW array fabricated by metal assisted chemical etching.

Plan-view SEM image of Si NWs fabricated by metal assisted chemical etching and decorated with Ag nanoparticles deposited by pulsed laser deposition.

SEM plan-view displaying in detail an individual Si NW completely decorated with Ag nanoparticles deposited by pulsed laser deposition.

This research has been performed in collaborations with the Physics department of the University of Catania, the Counsil of National Research Institute for Microelectronics and Microsystems (MATIS IMM-CNR) of Catania and the Insitute for Chemical and Physical Processes (IPCF-CNR) of Messina.

Heisenberg, Schrödinger and Ohm are in a car.
They get pulled over.
Heisenberg is driving and the cop asks him
"Do you know how fast you were going?"
"No, but I know exactly where I am" Heisenberg replies.
The cop says "You were doing 55 in a 35."
Heisenberg throws up his hands and shouts "Great! Now I'm lost!"
The cop thinks this is suspicious and orders him to pop open the trunk.
He checks it out and says "Do you know you have a dead cat back here?"
"We do now!" shouts Schrödinger.
The cop moves to arrest them.
Ohm resists.

# Contents

# The world of silicon nanowires

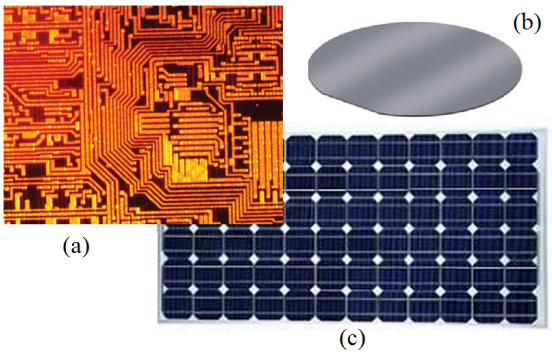


*Figure 1: (a) Silicon-based chip, (b) Si wafer and (c) Si photovoltaic module.*

Silicon is the leading semiconductor in microelectronics due to its availability, easy manufacturing and cheapness. Silicon has a stable and easy to grow oxide ($SiO_2$) that combined to the good electrical and structural properties promoted the industrial employment of this material in transistors, chips, solar cells, bio-compatible sensors and many others commercial products (fig.1). The advent of the first Si solid state transistor in 1954 has radically transformed the technology leading to a great technological development. In the following years, the performances and the number of Si transistors per printable area almost doubled every year according to the trend formulated by Moore in 1965 [1]. The demand for microprocessor-equipped products boosted the microelectronic research towards the realization of more capable chips in smaller and smaller packages down to the actual size of 1 $mm^3$, as shown in fig.2. Indeed, the Intel "Cannonlake" CPU architecture upcoming in 2017 will shift the limit of MOSFET interconnection node towards the 10 nm scale.

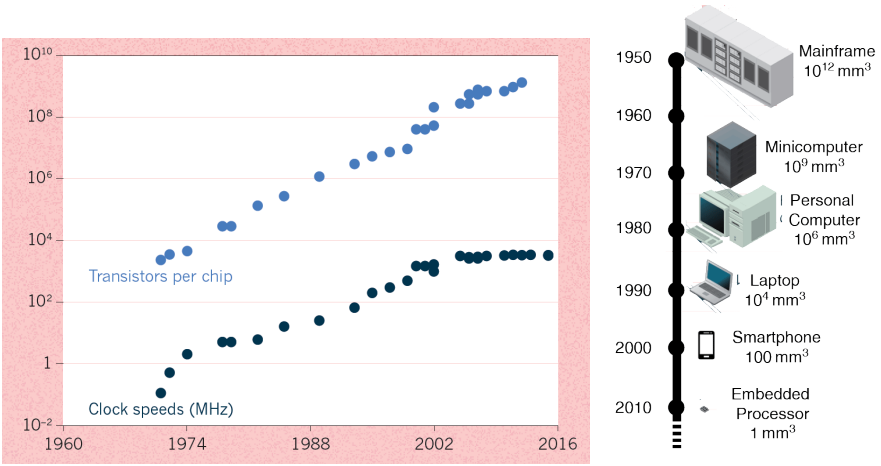


(a) (b)

*Figure 2: (a) Road map of the transistor number per chip and processor clock speed achieved during the last fifty years compared to (b) the device dimension scaling as predicted by Moore [1].*

However, such a drastic scaling of the devices size is really challenging from a technological point of view. Indeed, the complexity of the metal interconnection architectures and the related heating are the main issues limiting a further dimension scaling and the performance improvements of current devices. In order to overcome these limitations different materials have been evaluated as future leading semiconductors. However, they are incompatible with the current industrial processes and it is not that easy to get rid of silicon for the above mentioned reasons. Nanotechnology is currently achieving great advancement for the fabrication of next device generations, enabling the dimension scaling by implementing new physical effects for electronics, sensing and optics at the same time. Moreover, the telecommunication sector demonstrated that light can efficiently substitute the transport of electronic signal making it faster and heat less. Substituting electric signals traveling in Si chips with light is the aim of silicon integrated microphotonics that is the most appealing solution to overcome the interconnection and performances issues. Although there already exist Si-based optical fibers, waveguides, modulator and photodetectors, the key piece of integrated silicon photonics is still lacking: a Si-based light source.

The dimension scaling of Si down to the nanoscale opens the route towards new physical properties that are extremely interesting. For example, using nanotechnology Si can be made a good light emitter. As demonstrated from this thesis, Si nanostructures enable the observation of important properties that are crucial for applications. It is well documented that bulk Si is a poor light emitter at room temperature due to its indirect bandgap (fig. 3). In direct bandgap semiconductors photons are efficiently absorbed exciting electron/hole pairs whose subsequent radiative de-excitation occurs with lifetime of about $\tau_{rad} \sim$ 1-10 ns. In order to preserve the crystalline momentum conservation, the photons absorption/emission in Si is instead a three-particle process mediated by phonons occurring with radiative lifetime of 10 ms at room temperature. Therefore, competitive non-radiative recombination processes such as Shockley-Read-Hall ($\tau_{SRH} \sim 10 - 100\mu s$) and Auger ($\tau_{Auger} \sim 1 - 10\mu s$) relaxation mechanisms are more efficient in Si.

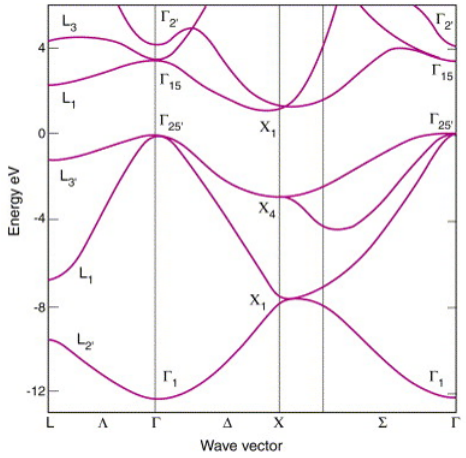


*Figure 3: Silicon dispersion relation showing its indirect bandgap structure: the minimum of the valence band is at the Γ-point ($k = 0$) while the conduction band edge is along the Δ line at 0.85 to the X-point*

The use of quantum confined structure is a striking strategy to improve the radiative efficiency in **silicon nanostructures** (NS) for integrated photonics, opening the route towards the development of multifunctional miniaturized devices [2].

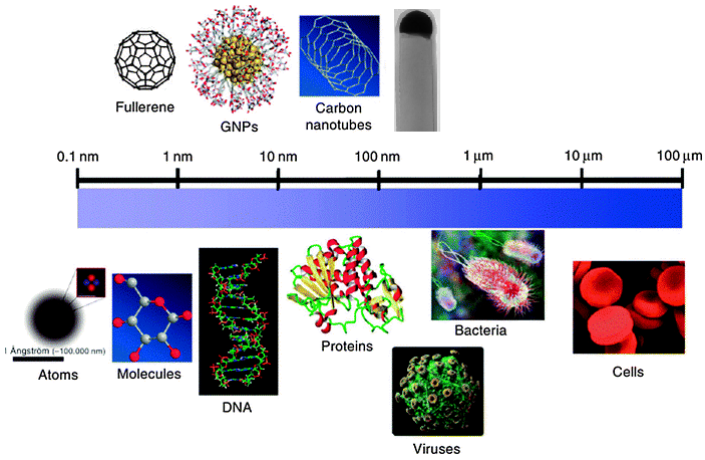


*Figure 4: A comparision between several nanostructure dimension (top line) to the biological blocks scale (bottom line) [3].*

Nanostructures are materials having dimension below 100 nm (fig. 4) and nowadays are widely used in several commercial applications, spacing from cosmetic, biology, paint and textile industry, energy, environmental treatment and especially electronics.

The innovation of nanostructures is related to the new class of physical effects that emerge when the material size is confined to the nanoscale. According to the effective mass approximation (EMA), quantum confinement generally manifests when the semiconductor dimension are below the Bohr radius of the electron-hole exciton (4.3 nm for Si). A drastic modification of electronic, optical and mechanical properties occur when the degrees of freedom of the charge carriers are reduced on such a length scale. As soon as the charge careers are constrained on a smaller region, their wavefunctions overlapping increases causing the crystalline momentum ($k_n$) and energy level distribution ($E_n$) quantization along the confinement directions. A bulk material can be confined into a quasi-2D layer by shrinking one dimension (fig.5 (b)), in 1D nanowire reducing the x and y-dimensions (fig.5 (c)) or in a 0D quantum dot by reducing to the nanoscale all the three spatial axis (fig.5 (d)). The number of electronic states per unit of volume and energy (density of states (DOS)) is drastically affected by the confinement occurring in one or more directions (fig. 5). As far as NWs are concerned, the DOS varies proportionally to $\frac{1}{\sqrt{E-E_n}}$, showing singularities in coincidence of $E_n$.

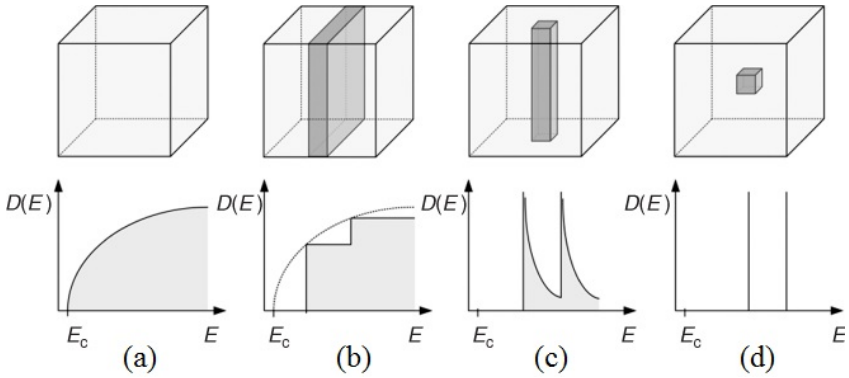


*Figure 5: Schematic representation of low-dimensional structures and associated density of states (DOS) reported as a function of the energy for a bulk material, quantum well, nanowire and quantum dot.*

As a result of the Heisenberg uncertainty principle, the careers spatial confinement introduces a greater uncertainty on the momentum of the particles, causing an energy shift $E_n$ from the bulk bandgap value. Theoretical predictions on the bandgap modulation are shown in fig. 3, showing a pronounced energy shift for Si nanowires whose diameter approaches the sub-10 nm scale [4]. Other theoretical models exploit the quantum behavior of semiconductor nanostructures in presence of different correction factors, such as the electrostatic energy interaction between electron and hole forming the exciton $(1/L)$ and the exchange interaction $(1/L^3)$ among them (being L the confinement dimension). The main advantage of quantum confinement is that the optical transition probability is also increased by reducing the size. Indeed, as the translational symmetry of the system is broken the crystal momentum is no longer a good quantum number allowing for quasi-direct no-phonon interband recombinations to occur more efficiently [5]. The total radiative probability per unit time is expressed as the product of the oscillator strength and the density of states involved in the transition. The oscillator strength describes the energy levels interaction and it exponentially increases by decreasing the volume of the system, arising the total radiative recombination probability [6].

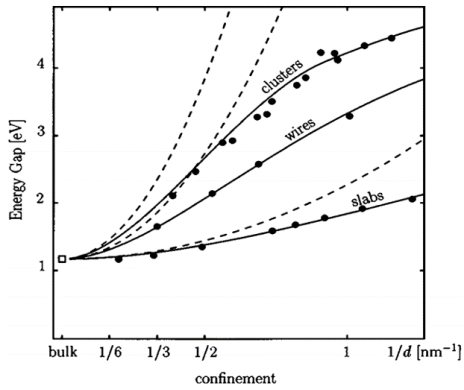


*Figure 6: Experimental optical bandgap modulation obtained for different Si nanostructures as a function of their radii.*

In particular, 1D structures as nanowires are very promising for several innovative sectors due to their unique physical properties, the huge surface-to-volume ratio, the optical and electrical properties. This thesis demonstrates the enormous potential of Si NWs obtained by metal assisted chemical etching. NWs obtained by this approach have nanometer radius (<10 nm) that determines extremely promising physical properties due to quantum confinement. In particular, light emission is observed at room temperature from Si NWs whose emission wavelength shifts by decreasing the size, in agreement with quantum confinement theory. Moreover, the realization of multi-wavelength Si-based light source operating at room temperature is demonstrated from the coupling of Si NWs and carbon nanotubes by using low-cost technologies. By engineering the synthesis process the fabrication of NW arrays having controlled fractal arrangements is demonstrated. NW fractal arrays present unique optical properties, such as multiple scattering that determines a strong light trapping and the observation of remarkable coherent effects for Raman scattering. Finally, the great sensing potential of Si NW has been studied in detail. This thesis demonstrates the huge potential for photonics, photovoltaic and sensing applications of NWs realized by using a low-cost and Si compatible approach.

# Thesis outline

In **chapter 1** an overview on the silicon nanowires synthesis scenario is presented by introducing the most employed bottom-up and top-down strategies, exploiting their main advantages and drawbacks. The impressive structural, optical and electrical properties of these nanostructures promote their implementation in low power consumption nanodevices with improved performances. Some representative examples of Si NW applications in field-effect transistors, broadband photodetectors, low-cost solar cells with improved light absorption and for selective and ultrasensitive biological detectors are reported in this chapter.

**Chapter 2** is focused on the realization of Si NWs by metal assisted chemical etching (MACE) by the use of discontinuous Au layers. The relationship among structural features and growth conditions are here discussed in detail. Indeed, the NW length, diameter, crystalline structure and doping can be precisely defined by using this low cost and industrially compatible process. The second part of this chapter deals with the fabrication of low cost Si-based light emitting sources. Si NWs with quantum confined size are realized by MACE leading to the observation of room temperature light emission from Si. According to quantum confinement theory, the emission wavelength can be red-shifted by tuning the NW diameter opening the routes towards low-cost, Si-based photonics. Moreover, the realization of innovative multiwavelength light sources operating at room temperature is investigated by embedding a carbon nanotube (CNT) dispersion inside Si nanowire arrays using a low cost and Si technology compatible technology. The NW/CNT hybrid system exhibits a tunable emission both in the visible and in the infrared which is strategic for telecommunication applications. The conditions leading to the prevalence of the visible or the IR signal have been identified and are herein discussed.

**Chapter 3** is focused on the design of two-dimensional random fractal arrays of Si nanowires. In fact, the structural arrangement of MACE synthesized Si NWs can be engineering by the deposition of a thin Au layer that superimposes its complimentary fractal arrange-

ment onto the Si NW arrays. Si NW fractal arrays display strong self-similarities over a wide range of length scales and the correlation among the fractal parameters and the optical properties are demonstrated. In fact, the ability to control the scattering, absorption and emission properties is investigated as a function of fractal dimension and lacunarity for different designs. A strong light trapping behavior in the visible range due to the efficient in-plane multiple scattering occurring in the Si NW layer has a promising potential for both photovoltaic and photonic applications.

In **chapter 4** the first experimental observation of a constructive interference effect in the backscattered Raman light from strongly diffusing Si nanowires is reported. Coherent backscattering of light (CBS) is observed when electromagnetic waves undergo multiple scattering within a disordered optical medium. CBS effect arising from the interference of inelastically scattered Raman radiation has been demonstrated in random Si NW arrays. The results are interpreted within the theoretical model of mixed Rayleigh-Raman random walks, exploiting the role of phase coherence in multiple scattering phenomena.

**Chapter 5** presents the decoration of MACE-synthesized Si NWs by Ag nanoparticles produced by pulsed laser deposition (PLD). In this way, the huge aspect ratio of NWs is coupled to plasmonic effects leading to the realization of ultrasensitive surface enhanced Raman spectroscopy (SERS) sensors. PLD conditions have been optimized to guarantee the uniform decoration of NW sidewall along all their length without the need of any post-deposition annealing by using a low-cost and Si implementable technology. The Ag nanoparticles morphology can be precisely tuned as a function of the NW length or the number of laser pulses and the correlation among the structural and optical properties of Si NWs decorated is reported. The great potentialities of PLD metal decoration of Si NWs for SERS applications demonstrates a low limit of detection and a huge enhancement factor compared to regular flat substrates.

# Chapter 1

# Nanowires: state of art

**Abstract**

*Silicon nanowires (NW) are considered among the leading building blocks for future silicon technologies due to their innovative structural and physical properties. This chapter presents an overview on the Si NWs synthesis scenario, introducing the most employed bottom-up and top-down strategies. A detailed description of the most common vapor-liquid-solid (VLS) based techniques is exploited, paying a special attention to their main advantages and drawbacks. Recently, metal assisted chemical etching processes are emerging as new promising fabrication methods due to their low-cost fabrication, fine control over NW structural properties, large-area processability and their compatibility with Si technology. A comprehensive insight on this fabrication class will be also given.*
*The second part of this chapter exploits instead the use of Si NWs in a wide range of applications. Indeed, Si NWs exhibit remarkable optical and electrical features promoting their implementation in photonic and electronic devices that show improved performances and lower power consumption. Si NW arrays have been also recently adopted by many groups for solar cell fabrication due to their strong light trapping and broad band absorption. Furthermore, the huge NW aspect ratio enabled their use as gas and biological high sensitivity sensors.*

## 1.1 Synthesis of silicon nanowires

Silicon nanowires (NWs) are recently emerging as innovative building block for future Si technologies due to their incredible structural and physical properties. In the last years many different strategies have been adopted to synthesize Si nanowires by using either the top-down or the bottom-up approaches.

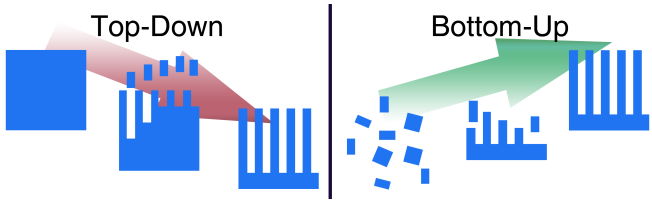


*Figure 1.1: Illustration of top-down and bottom-up fabrication approaches of Si nanowires.*

In the top-down approach, the initial bulk material is destructed into nanostructures by removing small amount by lithography or etching processes (fig. 1.1 (a)). All subtractive synthesis techniques as lithography, reactive ion etching (RIE) [7], wet chemical etching [8] belong to this category. These approaches have been extremely successful in nanoelectronics, where a precise structural control combined with extreme resolution on a nanometer scale are required. However, top-down techniques are very expensive and hardly implementable for industrial production. Therefore new strategies towards the low cost synthesis of nanostructures pushing the dimension scaling are demanded for the next future.
Similarly to what happen in nature, in the bottom-up approaches atomic and molecular blocks self-assemble to create complex structures with engineered properties (fig. 1.1 (b)). As an example, the chemical hierarchical assembly of nanostructures and all vapor-liquid-solid processes refer to this approach. The advantages of bottom-up is related to the ability to control nanostructures at the nanometer resolution, however its major limitation are the poor control of the structural properties and reproducibility. The bottom-up approaches involve the assembly of nanoscale building blocks with controlled and tunable chemical composition and morphology beyond the resolution limit of top-down methods enabling new physical properties.

The synergy between bottom-up and top-down fabrication processes achieved during the last years open the route for the controlled and large scale integration of Si NWs for a new class of multi-functional nanodevices.

### 1.1.1 Bottom-up

The Vapor-Liquid-Solid (VLS) mechanism for Si NWs synthesis was first proposed by Wagner and Ellis [9] in the mid-1960s. This method involve the presence of a metal catalyst (e.g. Au, Ti, Fe, Pt, etc.) and is based on the controlled thermodynamic evolution of the binary silicon/metal alloy. The choice of the metal precursor is critical to define the electrical and structural parameters of the nanowires, especially diameter, crystalline quality and orientation.

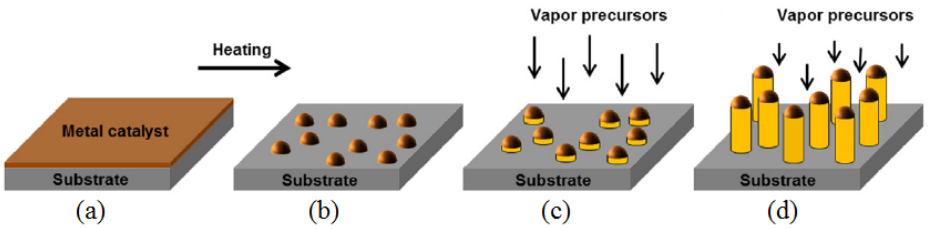


*Figure 1.2: Schematic illustration of the VLS process. (a) A metal catalyst layer is deposited on the substrate. (b) Upon heating, dewetting of the metal layer forms small droplets. (c) Introduction of vapor precursors leads to incorporation of the precursor inside the droplet and its precipitation at the catalyst–substrate interface. (d) Growth of c-Si NWs. [10].*

Figure 1.2 illustrates the steps required during the process. First, a seed metal layer is deposited onto the Si substrate, as an example by electron beam evaporation (EBE). The deposited substrate is then heated up to form small clusters (dewetting) which act as catalysts for the process. Once the metal catalysts are formed, the substrate is inserted in a chemical vapor deposition (CVD) chamber and heated above the melting temperature of the metal/Si mixture (eutectic point) to form metal/Si alloy liquid droplets. Then, Si gaseous precursors ($SiH_4$ or $SiCl_4$) are fluxed in and cracked into reagents when in contact with the heated substrate. Si atoms diffuse towards the metal/Si droplets and they are incorporated into

it. Once the saturation limit is reached the Si atoms solidify outside of the Si/droplet interface and a preferential growth beneath the droplet starts. The growth continues until temperature and Si precursors are supplied, finally forming an array of Si wires having the metal seed catalysts on their tips [11]. The name "VLS" refers to the phase transformation that occurs to Si atoms passing from vapor phase (V) to liquid droplets (L) towards the final solid phase (S). There are two key parameters driving this process: the temperature and the Si atomic percentage. The process temperature is defined by the metal catalyst. Gold is the preferred VLS-catalyst for Si NWs due to the low Au/Si eutectic temperature (363°C), its chemical stability and compatibility with VLSI processing. The Au catalyst seeds can be either deposited as a colloidal Au nanoparticle dispersion or by dewetting of a thin Au layer deposited by evaporation, sputtering, etc. The Au/Si alloy phase diagram is reported in fig. 1.3(a). Si NWs growth occurs when the temperature is above the eutectic and the Si percentage exceeds the threshold of 18.6%. In fact, for Si percentages above the eutectic equilibrium the Au/Si droplet reach the supersaturation condition. Therefore Si atoms precipitate and solidify below the Au/Si droplet interface leading to the growth of the monocrystalline nanowires (fig. 1.3 (b)).

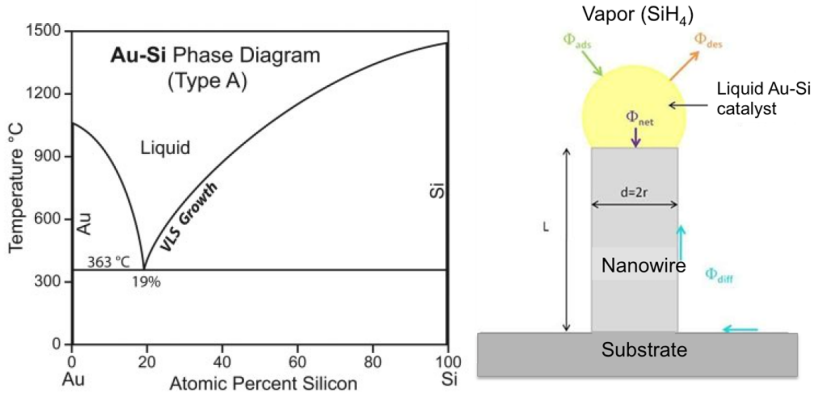


*Figure 1.3: (a) Phase diagram of the Au/Si alloy. (b) Kinetic sketch of VLS growth of Si nanowires [10].*

The growth kinetics of Si NWs by the VLS mechanism consists of four steps: mass transport in the gas phase; chemical reaction at the vapor–liquid interface; diffusion in the liquid phase; and incorporation of atoms in a crystal lattice. The NW growth occurs when the total Si atoms flux ($\phi_{net}$) provided either from the direct absorption of vapor ($\phi_{ads}$) or diffusion ($\phi_{diff}$) to the Au/Si droplet interface exceeds the desorption one ($\phi_{des}$) (fig. 1.3(b)). Hence, the precipitation of Si atoms at the liquid/solid interface occurs causing the growth of monocrystalline nanowires. The realization of dense arrays of VLS-Si NWs is displayed from the SEM reported in fig. 1.4, where it is observed that the nanowire radius r is always smaller that the catalyst droplet radius R [12]. In fact, from the interface equilibrium condition it is derived that $r = R\sqrt{1 - \left(\frac{\sigma_{ls}}{\sigma_l}\right)^2}$, where $\sigma_l$ and $\sigma_{ls}$ are the surface tensions of the liquid catalyst and of the liquid/solid interface, respectively [13].

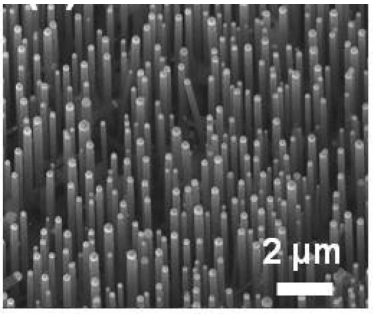


*Figure 1.4: 20° tilted SEM images of Au catalyzed VLS Si NWs grown on a Si(111) substrate in a CVD reactor [12].*

The VLS method works well over a wide range of wire lengths (100 nm - 100 $\mu$m) and diameters ( >5 nm - 100 nm ) and can be used for growing elemental (Si, Ge) as well as compound semiconductor NWs (e.g. GaAs [61], InP [62, 63], etc). A large variety of equipment is available for VLS Si NWs growth and nanowires with different features can be achieved by modifying the environment conditions. Chemical vapor deposition (CVD), SiO evaporation, molecular beam epitaxy (MBE), laser ablation, and solution-based VLS-based processes are respectively sketched in fig. 1.5.

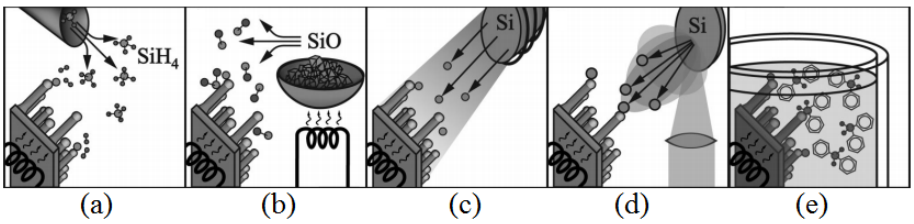


*Figure 1.5: Schematics of experimental setups for silicon nanowire growth. (a) CVD, (b) evaporation of SiO, (c) MBE, (d) laser ablation and (e) solution-based growth [10].*

In CVD processes, a volatile Si precursor ($SiH_4$, $SiCl_4$, etc.) is transported to the heated surface where it reacts and is cracked into its constituents (1.5(a)). CVD Si NWs are epitaxially grown with velocity varying from $10^{-2} - 10^3$ nm/min [9,10] and diameters ranging from 10 nm up to hundreds of micrometers by controlling the process parameters [9, 14]. Since surface diffusion plays a minor role in CVD, the length of the wires can also be tuned accordingly to the growth time. Moreover, by introducing additional doping precursors in-situ it is possible to obtain doped NWs having different doping profiles along the axial direction [15].
A cost-effective method for large scale production of Si NW is through SiO evaporation by oxide assisted growth (OAG). Evaporated SiO passes through a temperature gradient in a double region tube furnace in presence of inert gas, causing the disproportionation reaction of SiO into Si and $SiO_2$ that induces NWs formation (fig.1.5(b)) [16]. NW growth with or without metal catalyst is possible and growth rate of a few mm/h are recorded. NW diameters are determined by the size of the catalyst particle, although the interplay between the wire and the catalyst morphology seems to be more complex than in CVD. Si NWs fabricated with this approach are covered by a $SiO_2$ amorphous shell and generally agglomerate into bundles. OAG synthesized NWs present poor crystalline quality and diameters varying from 5 to 100 nm [17].
In MBE, a Si source is heated until evaporation producing a directional Si atoms stream aimed to the substrate where the atoms adsorb and crystallize (fig.1.5(c)). NWs realized by MBE are epitaxially grown and oriented as the substrate. Moreover, NW can

be engineered in axial heterostructures by switching the evaporation sources. However, the two major limitations of MBE are the low growth rate of a few nm/min and the high value for the minimum NW diameter of about 40 nm [18]. Laser ablation grown NWs differ in many aspects from the MBE whiskers and large quantities of ultrathin nanowires with high aspect ratios can be easily produced. A mixed Si–catalyst target is ablated from a high-power pulsed laser, the target atoms cool down by colliding with inert-gas molecules and condense to liquid nanodroplets onto the substrate (fig.1.5(d)). NWs can be grown independently from the substrate by using laser ablation synthesis and their composition is defined by the target. The growth velocities are typically of the order of micrometers per minute and the NW radii depend on the metal catalysts but also on the gas streamed through the furnace ($H_2$, $He$, or $N_2$) [19]. Although crystalline, laser ablated NWs are characterized by several structural defects and generally covered by $SiO_2$ amorphous shell. Moreover, the huge wire throughput leads to the formation of interconnected bundles of wires. Wire growth can also occur in liquid media for high-yield NW production. One method utilizes highly pressurized supercritical organic fluids enriched with a liquid silicon precursor, such as diphenylsilane, and metal catalyst particles (fig.1.5(e)). Similarly to the VLS mechanism, in this supercritical–fluid–liquid–solid (SFLS) method the alloy droplets precipitate forming Si NWs above the eutectic equilibrium, once the alloy gets supersaturated with silicon [20]. Crystalline nanowires with diameters as low as 5 nm and several micrometers long have been fabricated by this approach. For example, micrometer-long nanowires were synthesized at a temperature of 500°C using Cu catalysts by Korgel group [21].
In summary, VLS mechanism is supported by several synthesis processes producing NWs having different morphologies and structures. However, the high temperature required during the process and some poor structural features (doping, impurities, NW bundles, etc.) prevents the real implementation of VLS NWs in nanodevices. As described earlier, the diameter of VLS grown nanowires is always confined by the catalyst size [9, 22]. However, it can be very complex to decrease the size of the catalyst and in turn the diameter of nanowires in a controlled manner.

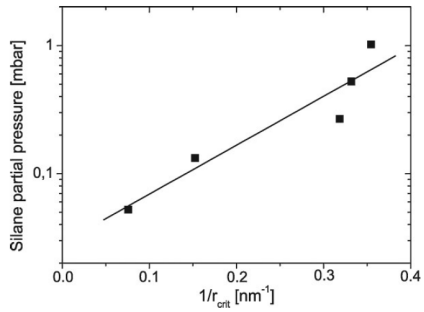


*Figure 1.6: Silane partial pressure versus the corresponding inverse critical radius $r_{crit}$ in Si NWs grown by VLS [10, 23]. The slope of the linear fit is about 8.8 nm.*

From thermodynamics consideration it can be derived the existence of a critical radius $r_{crit}$ for liquid metal droplet below which the growth is not permitted:

$$r_{crit} = \frac{2V_l}{RTln(p/p_0)}\sigma_{lv} \tag{1.1}$$

where $V_l$ is the molar volume of the liquid droplet, $\sigma_{lv}$ is the liquid–vapor surface energy, and $p/p_0$ is the Si precursor partial pressure [10]. According to this equation, using a smaller catalyst requires a higher degree of supersaturation. However, the chemical potential $\mu$ of metal alloy catalyst increases by decreasing the catalyst size in agreement with the Gibbs–Thompson effect:

$$\Delta\mu = \frac{2\gamma}{r_c} \tag{1.2}$$

being $\Delta\mu$ the chemical potential difference of the component species in the liquid droplet, $\gamma$ the surface energy, and $r_c$ is the droplet curvature radius [22].
Therefore, the Si vapor incorporation into the metal/Si liquid alloy becomes harder by decreasing the catalyst size, making it difficult to reach the supersaturation condition necessary to drive the NW growth. The growth of nanowires with diameters below tens of nm is in principle feasible. However, ensuring a smaller diameter (e.g., sub-10 nm) is difficult due to the thermodynamic limitations associated with the use of a nanocatalyst.

An additional difficulty arises when we want to downsize the catalyst, it is introduced from the manipulation of metal nanoparticles or droplets. It is well known that nanoparticles have strong van der Waals attractive forces and thus agglomerate into larger particles. Furthermore, Ostwald ripening occurs between nanoparticles at high temperature. Ostwald ripening is a spontaneous process that occurs because larger particles are more energetically favorable. Accordingly, nanoparticles tend to transform into large particles to attain a lower energy state if the temperature is high enough to induce diffusion of the metal component. Because the van der Waals attractive forces and Ostwald ripening lead to the formation of larger droplets, larger diameter 1D structures are often grown from a nanometal catalyst. Thus, metal nanoparticles have to be carefully separated one another in the course of the preparation, positioning on the substrate, and heating for the growth of 1D structures in order to limit these agglomeration processes. This constrain limits the NW final density.

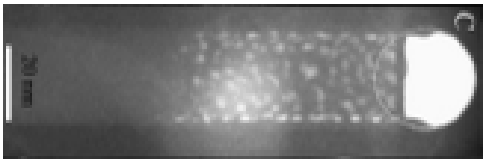

*Figure 1.7: Dark field TEM image showing the Au diffusion along the wire sidewall the during VLS process [24].*

A crucial drawback of VLS-methods is that its high thermal budget promotes the catalyst diffusion and incorporation into the wires, as shown in fig. 1.7. In particular Au, Ag, Zn, Ni and Pt precursors introduce deep electronic states within the Si electronic bandgap. The recombination rate critically depends on the position of the impurity level inside the bandgap of the semiconductor [25]. Indeed, according to the Shockley-Read-Hall (SRH) recombination statistics, the closer the energy level is to the middle of the bandgap, the higher is the recombination rate and the lower is the carrier lifetime.Although Au is the most used catalyst for growing Si NWs via VLS method, Au contamination introduces deep defects in the band gap of Si, therefore posing a major problem for electronic devices. Indeed, Au strongly reduces the minority carrier lifetime and the diffusion length by pro-

moting carrier recombination.
Therefore these precursors should be avoided for electronic and photonic applications. Although Au is chemically inert its complete removal damages the nanowires and is extremely difficult to obtain with traditional Au etchants (e.g. aqua regia, KI-$I_2$ and alkali cyanide solutions). Consequently, researchers are investigating other metal or metallic alloy seeds for Si NWs VLS growth among metals having ionization energies far from Si mid bandgap.

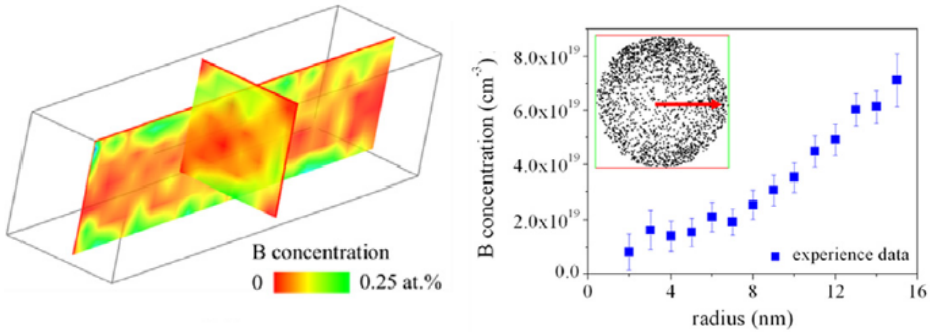


(a) (b)

*Figure 1.8: (a) Cross-section radial and axial B concentration in VLS grown Si NWs by atom probe tomography. (b) Boron concentration profile along the wire radius. The inset shows the cross-section view of B radial distribution. The red arrow represents the path along which the B concentration has been measured [26].*

The doping type and level of Si nanowires are two crucial features for devices realization. The conductivity of VLS NWs can be engineered by in-situ doping, incorporating shallow level impurities, such as B, P, As, Sb, etc., during the synthesis. The dopants concentration tune the position of the Fermi level across the Si bandgap, defining the type and concentration of the majority careers. While top-down NWs have the same doping as the original wafer, a severe drawback of VLS is the uncontrolled dopant segregation along the radial profile of the wire [27]. Indeed, the activated dopant density can be quite different from the nominal introduced concentration and very hard to measure since common techniques do not provide any information on the dopant distribution in the 3D geometry. For example, Perea et al. measured both axial and radial boron distribution from in-

situ doping of VLS-NWs by using atom probe tomography (APT), as shown in fig. 1.8(a) [26].
The B concentration is constant along the wire axis while an enhanced surface dopant concentration is observed along the radial profile. Indeed, the inner B doping concentration is $8.1 \times 10^{18}$ cm$^{-3}$ in the wire center and gradually increases towards the sidewall to $7.1 \times 10^{19}$ cm$^{-3}$ over a range of 16 nm (fig. 1.8(b)).

### 1.1.2 Top-down

VLS based methods for NWs fabrication provide a poor control over their diameter and spacing. Moreover, the electrical and optical properties of VLS grown NWs are detrimentally affected from the catalyst incorporation and a poor doping control.
Top-down approaches are valid alternatives for Si NWs synthesis matching the microelectronic requirements of controlled NW doping, placement and density for the definition of addressable devices. Lithography and reactive ion etching are some of the most accurate top-down approaches for the synthesis of vertical arrays of NWs with defined structural features.

#### Reactive ion Etching

A low-cost and fast solution for the synthesis of ordered Si NWs is provided by deep reactive ion etching (DRIE) performed on highly ordered silica ($SiO_2$) or polymer nanobeads (NB) patterns. Indeed, this method guarantees the precise control of NW diameter and pitch by tuning the beads diameter and the combined etching time of both nanobeads and substrate.

Figure 1.9 illustrates the main steps involved in a DRIE process. First, commercially available or chemically synthesized NB monodispersion is deposited onto the Si substrate in order to form a single or multiple beads layer to be used as a mask. Spin-coating is a fast and cost-effective deposition process but it generally produces small bead domains. A reliable technique to obtain dense and uniform distribution of NB over large areas is provided by the Langmuir–Blodgett (LB) method [28]. By using LB approach the nanobeads self-assemble

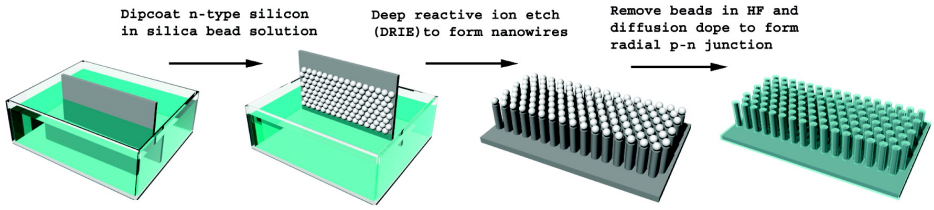


*Figure 1.9: Illustration of DRIE synthesis of a Si NW array. An ordered silica beads monolayed is transferred onto Si wafer, Si NWs are formed by DRIE using the beads layer as a mask and silica beads are removed by HF etching [7].*

into uniform and hexagonal close-packed arrays on a 4" wafer within tens of minutes. The diameter and spacing of the initial NB patter can be precisely tuned by isotropic RIE process. Indeed, the $SiO_2$ NB diameter is selectively reduced between 800 and 50 nm by using an $O_2/CHF_3$ mixture for the RIE etch. Afterwards, in a vacuum chamber a plasma is produced and massive ions anisotropically etch the Si region uncovered by the beads mask. The ions can deeply penetrate into the substrate eroding it and high aspect ratio steep-sided holes are obtained. The synthesis of Si NW by DRIE generally occurs in a $SF_6$, or chlorine ($Cl_2$) environment to etch selectively the masked Si substrate. Si NWs pitch and diameter are influenced by the silica bead diameter, while the length is determined by the DRIE time. Indeed, the final wire diameter is always smaller than the initial NB size and is coupled to the etch time due to the partial etching of the NB mask. Upon the array formation, the remaining $SiO_2$ beads on the NW tips are removed via HF etching. Figure 1.10 displays an example of Si NW ordered array obtained by 8 min DRIE etch in $SF_6$. The array is 5 $\mu m$ long and Si NWs have diameter of 390 nm when beads of 530 nm are used.

Si NW ordered array with diameter from 60 nm up to several hundreds of microns are demonstrated by using NB with diameter from 70 to 800 nm [28]. NWs of varying spacings from 50 to 400 nm were fabricated by etching of $SiO_2$ nanoparticles with diameters of 200 to 500 nm.
Both isotropic (RIE) and anisotropic (DRIE) combined with the shrinking of the $SiO_2$ NB lead to a sharpening of the NW tips. Si nanocones having a radius of curvature of 5 nm have been demon-

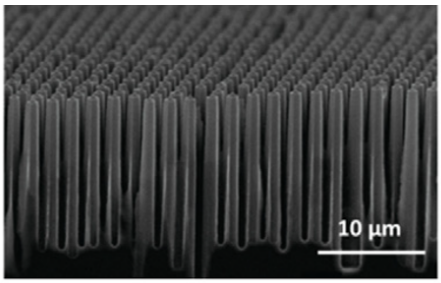


*Figure 1.10: Cross-section SEM image of an ordered silicon nanowire array fabricated by DRIE [7].*

strated, opening up the opportunities for refractive index matching applications.
This technique provides a precise control on the design of ordered high aspect ratio NW arrays over large scales, particularly suitable for solar cell and battery applications. However, DRIE approach produces Si NWs with rough surfaces, presenting scallops along the sidewalls due to the succession of etching and passivation ($C_4F_8$) steps necessary to control the process. In addition, plasma-induced surface damage can extend into the wire reducing the lifetime of minority carriers which is a limitation for all industrial applications. In fact, the presence of recombination losses that detrimentally affect the short-wavelength response of solar cell based on DRIE NWs have been demonstrated. Finally, for a further industrial implementation it is necessary to extend the uniformity of this process to at least 8" wafers.

### Electron Beam Lithography

There are several lithography techniques that provide a good fabrication control, such as deep ultraviolet lithography (DUV), electron beam lithography (EBL) [29], electron beam induced deposition lithography (EBID) [30], X-ray lithography (XRL) [31], nanoimprint lithography (NIL) [32] etc. Among others, the most adopted technique for the synthesis of Si NWs with controlled parameters is probably EBL.

EBL is a versatile technique adopted on different materials that is able to achieve sub-10 nm features at sub-20 nm pitches [33]. By

EBL it is possible to realize pattern or to design nanostructures by scanning a focused electron beam on the resist film spin-coated on the substrate, a procedure called "exposure". As for photolithography, the electron beam changes the resist structure thus its solubility, and the drawn pattern is transferred to the substrate by the selective etching of either the exposed or non-exposed regions ("developing" procedure). EBL processes can be assisted by different oxidation processes to further boost the resolution limit reducing the wire size. Thermal oxidation is the most widely used process for the size reduction of NWs towards the 10 nm scale. However, a substantial thermal oxidation detrimentally affects NW electrical performances, preventing industrial applications. The advantages of electrochemical size reduction are the low temperature operation, better control on the process and surface morphology. A dramatic drawback of this technique is the requirement of an individual electrical contact per each nanowire during the etching. Linnros group perfomed size reduction by electrochemical etching mounting the EBL synthesized wire on a chip equipped with electrode probes to individually contact nanowires at both sides [34]. The etching driving parameter is the Si surface hole/$F^-$ ions concentration ratio. The electrochemical cell can be developed for a chip containing NW arrays to increase the throughput. A comparison among the SEM microscopies of a planar single Si wire with diameter of 100 nm realized by EBL before (top panel) and after (bottom) electrochemical size reduction is reported in fig. 1.11, demonstrating the achievement of resolution of 10 nm for a NW length of 1 $\mu$m.

Nevertheless, this method is too complex, has low throughput rate and produces nanowires having rough profiles that are not implementable on an industrial scale. Furthermore, e-beam lithography is often used to design metal dot pattern for the realization of vertical Si NW arrays by either VLS, deep reactive ion etching or chemical etching processes. Indeed, the realization of etch-resistant metal masks ( as $Al_2O_3$, $Al$, and $SiN_x$) facilitate the formation of high aspect ratio nanowires (30:1) with controlled parameters [35]

As an example, Chu and Duan demonstrated the direct fabrication of c-Si nanotubes and NWs with ultrathin size down to 10 nm by combining EBL and low temperature plasma reactive ion etching $O_2/SF_6$ treatment [36]. The formation of a thin $SiO_xF_y$ shell on the

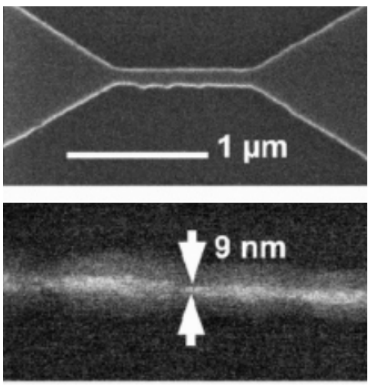


*Figure 1.11: A 100 nm diameter Si channel realized by EBL before (top panel) and after (bottom panel) electrochemical size reduction down to sub-10 nm diameter [34].*

nanostructures surface occurs during the process, providing smoother sidewall profiles compared to other gas mixture and etching. By this approach, the pitch and diameter parameters of Si NWs can be engineered to modify the optical response of the material. Although EBL technique is compatible with CMOS technology, its low throughput, high cost and long exposure time are not implementable for full wafer layouts. Therefore, the use of this form of high resolution lithography is limited to photomasks fabrication, low-volume production of semiconductor devices and for research and development applications. Electron-beam lithography represents a valid alternative to achieve good control over the nanoscale. However, this technique has low throughput and its high cost is a great disadvantage for many industrial and large-scale applications.

**Nanoimprinting lithography** x (NIL) is the next generation lithography solution to easily produce low-cost masks for Si NW array realization over large areas of a few $cm^2$. During a NIL process an imprint mold is pressed onto a polymer layer generally spin-coated on the substrate. When in contact with the mold, the patter is transferred to the polymer by either thermal or cold welding process. The polymer layer can act as an etch mask in order to transfer the pattern into the underlying substrate with high fidelity and precision. Chou et. al demonstrated the fabrication of sub-40 nm diameter, high aspect ratio Si NW arrays over a wide-area by com-

bining nanoimprint lithography (NIL) and deep reactive ion etching (DRIE) [32]. The mold pattern was transferred onto a tri-layer resist made of imprint resist/$SiO_2$/ and antireflection cross-polymer (ARC) (150/20/180 nm) to be used as a DRIE mask for Si nanowires etching. The achievement of nearly vertical nanostructures with wavy sidewalls is possible by alternating etching and passivation treatments (Bosch process). During the etching phase, the ions directly bombard the substrate attacking the passivation layer at the bottom of the trench but not along the sides, thus preventing further etching. DRIE process was optimized with reduced cycle times and gas flows to achieve high aspect ratio (>60:1) NW having vertical sidewalls with roughness below 8 nm. However, NIL is still far too complex for real industrial applications and the sidewalls scallops lead to structural defects and poor electrical quality.

### Metal Assisted Chemical Etching

The application of all the previous mentioned techniques is limited by the long processing time, high operating temperature and the complex equipment employed. The metal assisted chemical etching (MACE) of Si wafers is a top-down approach for the low-cost synthesis of highly oriented Si NW arrays with desired structural features. This method was demonstrated in 1997 by Li and Bohn, who first optimized it for the fast fabrication of porous Si by etching an aluminum (Al) covered Si substrate in an aqueous mixture of $HNO_3 : HF$. In 2002, Peng et al. pioneered this technique fabricating a high density array of Si NW at room temperature by immersing the wafer in a $AgNO_3 : HF$ solution [8, 37].The method is based on the selective oxidation of Si occurring at the metal/Si interface and $SiO_2$ subsequent removal by a proper etching agent. The scheme in fig. 1.12 presents the steps of the process. First, an oxygen-free Si surface is obtained after HF etching (a). Then the bulk material is immersed in a HF aqueous solution containing the metal salt precursor. Usually, $AgNO_3$ is used as process precursor but other oxidizing agents like $H_2O$, $H_2O_2$, $HNO_3$, etc. can be added to the solution to strengthen the effect. The metal salt dissociates in the solution forming Ag nanoparticles, whose density and dimensions are related to its initial concentration (b). The metal NPs deposit onto the clean Si sur-

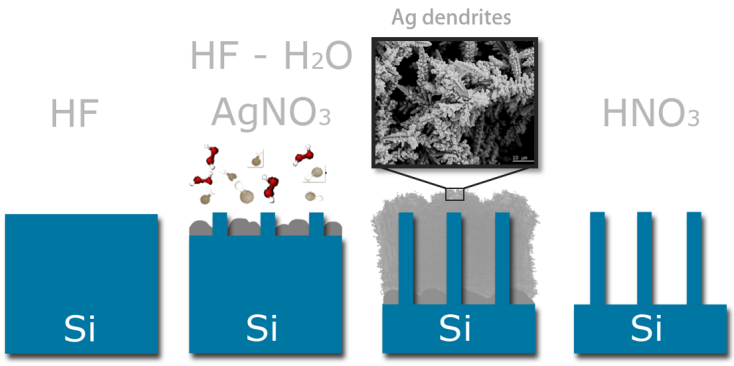


*Figure 1.12: Schematic illustration of metal assisted chemical etching of Si nanowires. An oxygen-free Si bulk is immersed in a $AgNO_3 : HF$ solution where Ag nanoparticles precipitate depositing onto the substrate. The metal covered region are oxidized into $SiO_2$ and etched by HF. Silver dendrites are formed during the process and removed by nitric acid.*

face, locally producing $SiO_2$ underneath the metal covered regions. The Si dioxide is then removed selectively from the fluoridric acid and the metal particles sink into the wafer leaving a pitch behind (c). The metal covered regions sink into the wafer while the complimentary region see the formation of nanowires (d). The process is based on redox reactions that preferentially occur near the noble metal nanoparticles which precipitate in the solution depositing onto the crystalline silicon wafers.
The MACE kinetic can be microscopically described by considering a local anode (Si) and cathode (metal) sites at the etched Si/metal interface that produce a local cell current during etching according to the mechanisms depicted in fig. 1.13(a). During the cathode reactions the oxidation agent $H_2O_2$ is reduced at the metal/solution interface (1):

$$H_2O_2 + 2H^+ \rightarrow 2H_2O + 2h^+ \tag{1.3}$$

As suggested by Li and Bohn [38] and Harada et al. [39], the cathode reaction is assisted by the additional reduction of protons into hydrogen:

$$2H^+ \rightarrow H_2 \uparrow + 2h^+ \tag{1.4}$$

The noble metal acts as a microscopic cathode on which the reduction of the oxidant occurs. The holes generated by the reduction of the

oxidant agent diffuse into the noble metal in contact with Si (2) and are injected into the Si due to the electronegativity difference (3). At the anode, Si is oxidized and dissolved by HF (4). Several models have been proposed to explain the Si dissolution but none of them can be verified easily from experimental in-situ observation. For anode reactions three dissolution models are presented:
Reaction I (RI)

$$Si + 4h^+ + 4HF \rightarrow SiF_4 + 4H^+ \tag{1.5}$$

$$SiF_4 + 2HF \rightarrow H_2SiF_6 \tag{1.6}$$

This reaction determines the direct dissolution of Si in a tetravalent state without forming $SiO_2$.
Reaction II (RII) involves the direct dissolution of Si in divalent state:

$$Si + 4HF_2^- \rightarrow SiF_6^{2-} + 2HF + H_2 \uparrow + 2e^- \tag{1.7}$$

While reaction III (RIII) considers the Si oxide formation followed by its dissolution:

$$Si + 2H_2O \rightarrow SiO_2 + 4H^+ + 4e^- \tag{1.8}$$

$$SiO_2 + 6HF \rightarrow H_2SiF_6 + 2H_2O \tag{1.9}$$

Accordingly, the Si atoms under the noble metal are oxidized due to the holes injection and dissolved by HF (anode reaction). In reaction RI Si dissolves in a tetravalent state leading to gaseous formation. During RII and RIII reactions Si oxidation is followed by the dissolution of the oxidized species. In fact, RII and RIII models differ in whether $H_2$ is generated accompanying the dissolution of Si (in RII), or whether Si oxide is formed at the surface of the Si substrate before the dissolution of Si (in RIII). It seems that model RII happens because hydrogen is generated in a typical etching and is confirmed by the bubbles production during the process. Both models are valid and is more likely probable that a combination of both reaction simultaneously occurs.

In fig. 1.13(b) the difference among the electrochemical potential of the reacting species are compared to Si potential energy at the valence and conduction bands. This potential difference is the driving force leading to the necessary holes injection for the oxidation and

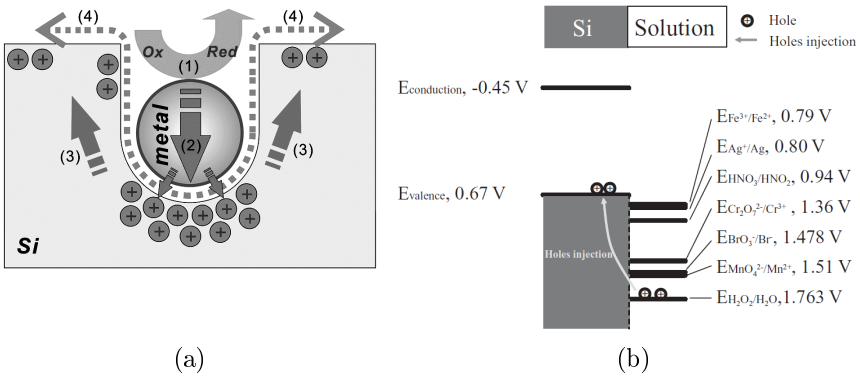


(a) (b)

*Figure 1.13: (a) Kinetic evolution scheme of metal-assisted chemical etching. (b) Scheme of the potential relationship between bands in a Si substrate and standard potentials of various oxidants. [37].*

dissolution of Si. It can be observed that $H_2O_2$ is more positive than the valence band of Si and more positive than oxidants usually used for Si etching ($HNO_3$, $Fe(NO_3)_3$, $KMnO_4$, $KBrO_3$, $K_2Cr_2O_7$, etc.). The holes produced from $H_2O_2$ reduction are then injected into the valence band of Si. The cathode reaction (1) occurs faster on the surface of noble metals than on a bare silicon surface. Upon the oxidant reduction at the noble metal interface, holes are injected into the Si substrate and Si etching occurs. Several noble metals e.g. Au, Pt, Fe, Pd and Ag have been widely used to catalytically reduce $H_2O$ and $O_2$.

The most commonly adopted MACE processes for Si NWs synthesis involve the use of metal salts solution, typically $AgNO_3 : HF$ [40] or $KAuCl_4$ [41]. The synthesis of Si NWs by MACE involve the formation of metal dendrites structures on the top of the wires as byproduct of the etching, as shown in fig. 1.14. These metal dendrites can be easily removed using a specific etching reagent, as for $HNO_3$ in the case of Ag removal. However, this further etching step induces the NW sidewall surface modification that can detrimentally affect the structural, optical and electrical properties of the wires.
The major advantage of MACE synthesis is its fine control over the structural properties of Si NWs. In fact, Si NWs produced via the top-down approach inherit the properties of the starting bulk mate-

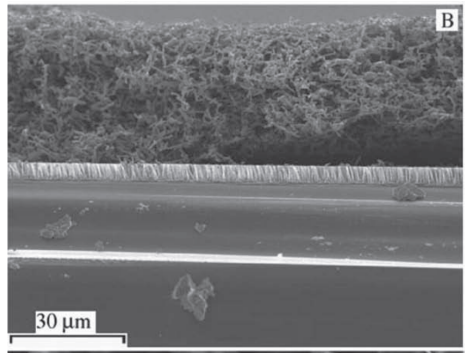


*Figure 1.14: Cross-section SEM view of Si NWs realized by MACE in a HF/AgNO solution showing the formation of silver dendriteson the top of the array [42].*

rial, such as doping profile and crystalline orientation. Furthermore, the NW length can be tuned with great accuracy simply varying the etching time while the radius and density are interrelated parameters defined by the metal precursor concentration. Highly ordered Si NW arrays with controlled structural features can be obtained by performing MACE on metallic mask designed lithographic techniques. In fact, the metal precursor layer can be engineered to promote the local oxidation on the metal covered c-Si substrate for the controlled realization of well-oriented NW arrays of defined size, length and distance. By using MACE, Si NWs with diameter ranging from 30 to 100 nm and length varying from a few tens of nm up to tens of $\mu$m can be obtained, leading to nanostructures with an aspect ratio above 200. This approach is maskless, low-cost and produces Si NWs with controlled features over the wafer scale in short period of tens of minutes. Moreover, it is implementable in CMOS technology due to the low temperature, the fabrication on a large scale and the control of the crystalline quality and doping that for such nanowires are the same of those of the starting Si bulk.
However, as in all top-down approaches, a large portion of the material is wasted. Therefore, MACE has to be extended to microcrystalline Si decreasing the overall material cost for industrial application. Indeed, Chang et al. [43] demonstrated the realization of polycrystalline and amorphous Si nanowires by MACE using a well defined metal pattern on Si substrate.

## 1.2 Silicon nanowire applications

Silicon nanowires have been demonstrated as one of the most promising building blocks for future nanodevices due to their innovative physical properties. Indeed, in the last decade huge progesses have been achieved by employing Si NW in field effect transistors [44, 45], solar cells [7, 46], sensors [47, 48] and lithium battery [49, 50, 51]. The second section of this chapter illustrates the significant advancement achieved in Si NW-based nanodevices.

### 1.2.1 Electronics

As predicted by Moore's law, the scaling of CMOS technology is a key aspect to achieve better performances, reduce power consumption and heat dissipation by decreasing the overall device cost [1].
A very recent demonstration of the advantage of using NWs has been provided by Weber and coworkers, who realized a configurable field effect transistors (FET) based on a single Si nanowire [52].

A schematic illustration of the programmable NW device is reported in fig. 1.15(a) showing an heterostructure of $NiSi_2$/Si/$NiSi_2$ axial junction. Intrinsic (112) oriented Si NWs were prepared by VLS, dispersed on a $SiO_2$ coated n-Si substrate and then covered by 10 nm of $SiO_2$ gate dielectric formed by thermal oxidation. The $SiO_2$ was removed and replaced by Ni at both NW extremities and a 600°C annealing promotes the Ni diffusion into the Si and the reaction in order to form crystalline $NiSi_2$ source and drain contacts regions. Two Schottky barriers are formed at the $NiSi_2/Si$ interfaces, as shown from the SEM reported in fig. 1.15(b), having 0.66 eV electron and 0.46 eV hole injection potentials.
At the barrier regions two individually addressable Ti/Al gates were patterned by EBL in order to tune the MOS operation mode. The SEM reported in fig. 1.16(c) shows the final device after the electrodes deposition. The two Schottky junctions at $NiSi_2/Si$ interfaces enable the reconfiguration of the device as a p- or n-FET by applying an external bias to both regions. The FET design was improved by implementing a Coulomb blockade architecture. In fact, one junction controls the desired charge carriers injection into the active Si channel, while the second is biased to block the complimentary carriers,

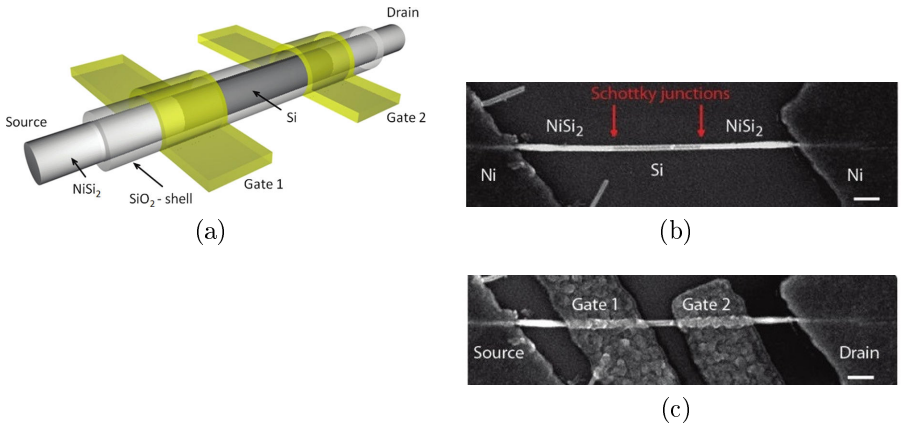


*Figure 1.15: (a) Schematic illustration of a reconfigurable silicon NW FET formed by a $NiSi_2/Si/NiSi_2$ wire with diameter of about 100 nm covered by a 10 nm thick $SiO_2$ gate dielectric. Two individual addressable metal Ti/Al gates are formed over the $NiSi_2/Si$ Schottky junctions. The external $NiSi_2$ regions are used as source and drain contacts. SEM images of NW FET (b) prior and (c) after the gate electrode patterning. The red arrows indicate the location of the Schottky junctions. The scale bar is 200 nm for both images [52].*

tuning the wire conductance [52].
The red curve presented in fig. 1.16(b) shows the typical I-V trend for a p-FET. The n-type behavior can be programmed by inverting the polarity of the program gate and drain biases, as shown from the blue I-V characteristics . In this case the $V_{G2}$ potential blocks the injection of holes from the drain electrode into the active region allowing the electron transport. Both p- and n-FET devices are completely reversible and a negligible hysteresis is observed.
The total modulation for the p-FET (n-FET) configuration is $1 \times 10^9$ ($6 \times 10^7$) within a $V_{G1}$ range of 3 V. Maxima currents of about 94 $\mu A \cdot \mu m^{-1}$ and 5.3 $\mu A \cdot \mu m^{-1}$ and peak transconductance of 6 $mS \cdot \mu m^{-1}$ and 7.5 $nS \cdot \mu m^{-1}$ are measured for NW p-FET and n-FET respectively competitive with planar MOSFET parameters [45, 52]. By using Si NW the realization of reconfigurable transistors is possible.

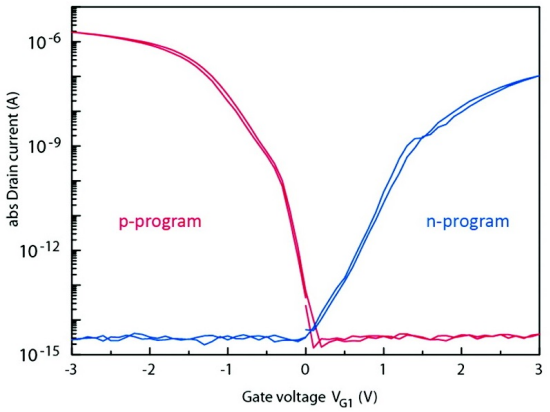


*Figure 1.16: Drain current-voltage characteristic for a p-programmed FET as a function of the applied gate bias [52].*

Another example of Si NWs implementation in Si microelectronics is the realization of a visible-IR detector based on silicon. Indeed, Si CCD, CMOS camera and Si photodetectors are widely used in commercial devices for visible light detection. Nevertheless, due to its 1.1 $\mu m$ bandgap, Si is not suitable for IR detection that is strategic for telecommunication and for imaging.
The main strategies reported in literature in order to obtain light detection over a wire range involve the use of low-bandgap semiconductors (Ge, InGaAs [53, 54], etc.), the realization of hybrid Si-Ge heterostructures or the introduction of deep impurity level by doping [55, 56]. Both strategies generally require an advanced technology, long processing time and their manufacturing processes are very expensive. Moreover these devices have limited sensitivity due to their fabrication constrains.
In this scenario, either single NW or vertically aligned Si NW arrays represent a promising resource for photodetection due to their high surface-to-volume ratio and electronic properties [57]. Lo et al. [58] took advantage of the Si NW arrays huge aspect ratio to fabricate high-sensitivity visible and infrared detectors.

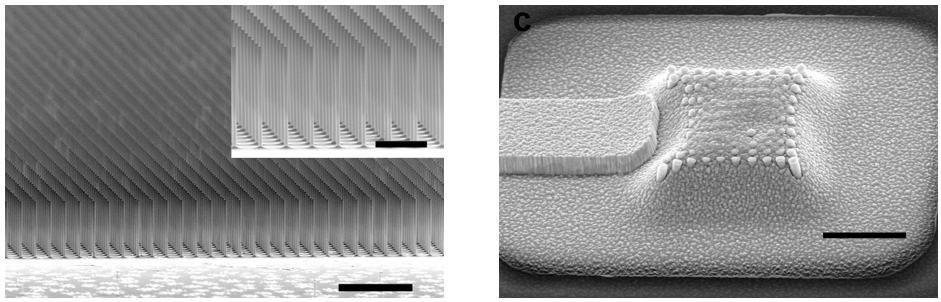


(a) (b)

*Figure 1.17: (a) Large area SEM cross-section and inset of 4 $\mu m$ long Si NW array fabricated using nanoimprint lithography. NW Diameter and pitch are 200 nm and 1 $\mu m$ and the scale bars are 5 and 2 $\mu m$ for inset. (b) Si NW detector obtained by embeddeding nanowires in polyimide covered by ITO contact window. Ti/Au metal contacts were used to polarize the active area (the scale bar is 5 $\mu m$). [59].*

An ordered array of vertically aligned Si NWs was realized by DRIE in $C_4F_8$ and $SF_6$ gases using a Ni dots ordered array deposited on an epitaxial $p^+/p/p^+$ Si substrate corresponding to the source/device/drain regions. NWs were annealed at 650°C to form NiSi alloy at the NWs tips, acting as a contact. In fig. 1.17 (a) is reported an SEM image of a 4 $\mu m$ long Si NWs array having diameter of 200 nm and spacing of 1 $\mu m$. The inset shows the perfect order and vertical orientation achieved by this technique.
Then NWs have been embedded in polymide and a $O_2$ plasma etching was used in order to free the NW tips. Finally a transparent ITO layer was deposited as a photoactive window and Ti/Au contacts were patterned. The final device made of 100 NW is reported in fig. 1.17 (b), displaying on the left the Ti/Au contact used to polarize the central region where NW tips are visible [59, 58]. The NW silicon body acts as the depleted region of the device due to the formation of native surface trap states distributed along the Si bandgap. The charge carriers are trapped at the surface states, causing a depleted region due to the surface band bending. Such process introduces the presence of an effective radial "gate" field that forces the photogenerated electrons to the surface, where they recombine with the trapped holes. The carrier recombination modulates the gate field,

while holes remain confined to the center of the nanowire. The advantages of using Si NW arrays is the fabrication of photodetectors that are sensitive to both visible and infrared region according to interband or intrabands absorption mechanism. The device shows a very high detection sensitivity lower than 0.1 $fW/\mu m^2$ incident power per nanowire when irradiated with visible light. Infrared detection via band-to-band transition is not allowed in bulk Si and intraband absorption from surface states is negligible due to the small surface-to-volume ratio. The major advantage of NWs is related to their huge aspect ratio that enables the IR absorption due to the presence of a high density of surface trap states. Moreover, the ordered geometry introduces high refractive index fluctuations among the semiconducting NW and the surrounding medium. Such fluctuations increase the light scattering, trapping the light inside the device and increasing the overall absorption efficiency. Si NW infrared detection was tested under 1550 nm illumination showing a sensitivity level on the order of 1 pW per wire, several orders of magnitude higher compared to the state of art of Si NWs detection. The IR sensibility is 4 orders of magnitude lower than visible one due either to the decreased absorption cross section at longer wavelengths and to the lower surface states density compared to interband transitions. This result is even more remarkable considering that the absorption coefficient of NW is even smaller than bulk silicon.

### 1.2.2 Photonics

Although silicon is the leading semiconductor for a wide range of applications, its light emission properties are detrimentally affected by its indirect bandgap. The achievement of Si emission and Si-based emitting devices is still scarcely reported. However, light emission from Si NWs has been demonstrated by using different strategies, as fluorescent doping impurities, defect radiative recombination or surface states introduction and molecular complexes on their surface. Indeed, Kalem et al. reported the near-IR emission at room temperature from strained Si/Ge NWs grown by the VLS process [60]. However the emission mechanism is not clear due to the complex structure and moreover the IR-shift achieved by stress-induction processes is hardly controllable.

Moreover, some groups demonstrated the emission of Si NWs doped with Fe or others emitting impurities that generally detrimentally affect the material electrical behavior, preventing the electrical pumping and increasing non-radiative recombination losses.
Again, nanotechnologies proved to be the key strategy to succeed in Si photonics. Indeed, quantum confined Si NWs have recently enabled visible emission from Si at room temperature [61, 62]. Si NWs with radial dimension lower than Si excitonic Bohr radius allow the manifestation of quantum confinement effects allowing light emission at room temperature [63]. A fundamental aspect for photonic devices is the ability to electrically pump the Si NWs emission.

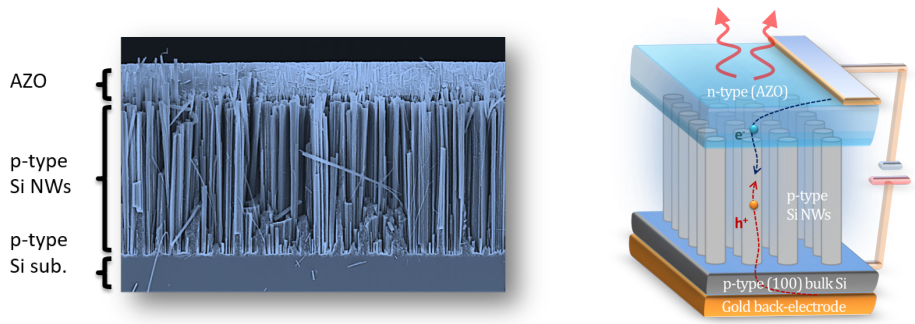


(a) (b)

*Figure 1.18: (a) SEM cross-section image displaying the NW LED. (b) Schematic illustration of Si NW-based LED configuration [62].*

A remarkable demonstration of a room temperature, electrically pumped Si-based light emitting device (LED) by using quantum confined Si NWs is illustrated in fig. 1.18. A few millimeter square LED prototype was demonstrated on a p-Si substrate ($10^{20} at/cm^3$), where Si NWs have been fabricated by MACE using a discontinuous, 2 nm-thick Au precursor layer deposited by electron beam deposition. A dense array ($10^{12} NW/cm^2$) of vertically aligned p-doped, 2.5 $\mu m$ long Si NW array has been synthesized, as visible from fig. 1.18(a). The top electrodes contact was formed by an aluminum-doped zinc-oxide (AZO) layer onto the Si NWs while the Au back-electrode was deposited on the Si substrate rear. A SEM microscopy depicting the Si NW LED structure is presented in fig. 1.18(a), clearly showing

the formation of an axial p-n junction at the Si NW/AZO interface. Figure 1.18(b) illustrates a scheme of the NW LED working principle when an external forward bias is applied [62].

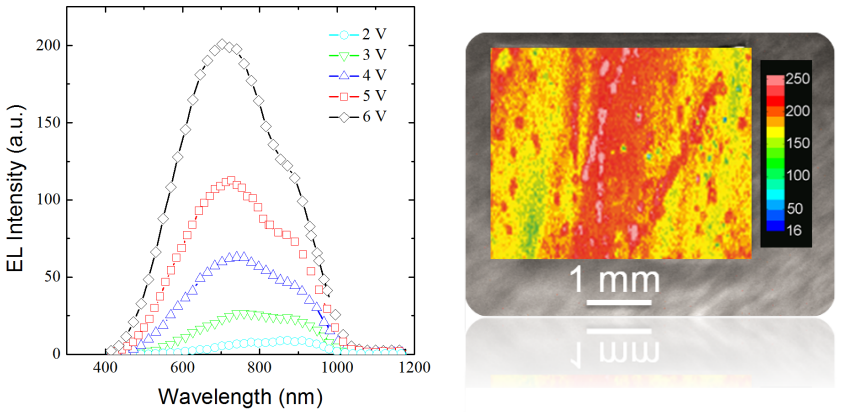


(a) (b)

*Figure 1.19: (a) Electroluminescence spectra of the Si NW LED device for applied forward bias ranging from 2 to 6 V. (b) Emission microscopy of Si NW LED visible emission at 700 nm obtainted over a 10 $mm^2$ at 4 V bias. [62].*

NW LED room temperature electroluminescence (EL) reported in fig. 1.19(a) shows a broad band emission centered at about 700 nm for an applied external bias ranging between 2 and 6 V. EL emission from quantum confined Si NW is demonstrated at an extremely low operating voltage of 2 V. An emission microscopy (EMMI) acquired at a 4 V bias is reported in fig. 1.19(b), clearly displaying the good uniformity of the device emission over a large area of 10 $mm^2$ [61]. This NW LED prototype is extremely promising if compared to other silicon nanostructured light emitting devices, as Si nanocrystals (NCs) embedded in silicon dioxide whose electrical pumping is hard to obtain due to the presence of a dielectric medium. Indeed, the main advantage of Si NWs with respect to Si NCs is the absence of the oxide matrix avoiding the non-radiative recombination occurring at the oxide defect sites. Moreover, NWs can be directly contacted by the electrodes avoiding inefficient tunneling conduction mechanism [64].

The reported results open the route toward the use of Si NWs as future building blocks for low-cost photonics.

### 1.2.3 Photovoltaics

The world energy demand is ever growing and renewable energies combinations are addressed as a possible solution in order to satisfy the request of power supply and reduce the $CO_2$ emission at the same time. In particular, photovoltaics is one of the most adopted renewable sources for its availability and efficiency. Almost 93% of the commercially available solar cells are based on silicon technology due to its cheap manufacturing [65, 66]. Nevertheless, Si absorption in near-infrared region has some limits and Si solar cells must be several millimeters thick to absorb about 90% of the incident infrared radiation between 700 to 1100 nm, corresponding to one-half of the solar energy available above the Si bandgap. Therefore, the optical and electrical features of Si NWs can be exploited in order to improve solar cells performances and reduce their cost. Indeed, the NW surface roughness increases the overall light absorption allowing to reduce the solar cell thickness. In this way a drastic reduction of the solar cell cost can be obtained by diminishing the amount and quality of the Si substrate employed [46]. Finally, the charge collection efficiency can be further improved in Si NW radial junction solar cells by collecting charges on paths smaller than the recombination length, thus avoiding carriers recombination. In 2007 Tian et al. [67] demonstrated the realization of a single Si nanowire solar cell . They implemented a p-i-n coaxial architecture on a single VLS-grown Si wire with a diameter of about 300 nm. A maximum power output of 200 pW and an apparent energy conversion efficiency of up to 3.4% were measured per single NW device, which are outstanding single NW p-n junction performances. Their pioneering work opened the route towards the massive use of Si NWs for the highly efficient third generation of solar cells. Recently, several solar cell architectures based either on single wire, NW array or Si NW/hybrid structures have been developed.Indeed, the use of Si NWs arrays rough surface greatly improves light absorption compared to planar surfaces due to the increase of light paths inside the material.

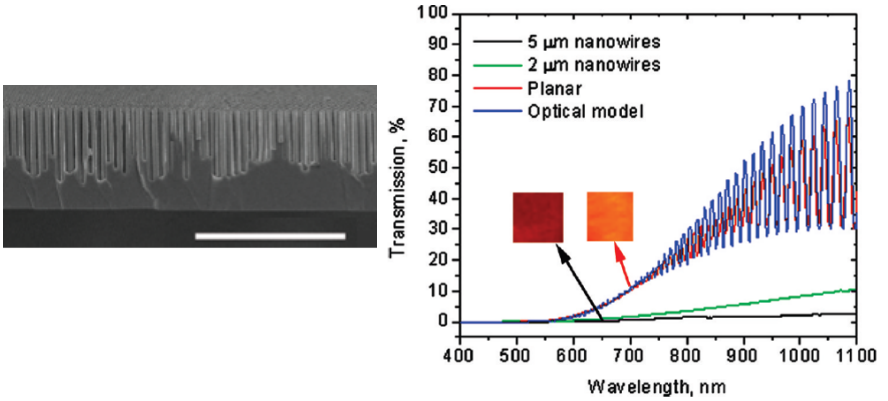


(a) (b)

*Figure 1.20: (a) SEM image of a 5 µm Si NW array fabricated by DRIE. The scale bar is 10 µm. (b) Optical transmission characterization of a plasna Si thin film solar cell (red), 2 µm (green) and 5 µm (black) Si NW array solar cell compared to the optical model spectra for a 7.5 µm thin film (blue) [7].*

A fine strategy to improve standard Si solar cells is provided by Garnett et. al, who implemented a radial p-n junction Si NW array solar cell design [7]. Si NWs were fabricated by DRIE process onto a n-doped Si substrate, as shown from the SEM displayed in fig. 1.20(a) a dense array of vertically oriented NWs was obtained. A radial p-n junction was realized by doping Si NW through boron diffusion. The transmission spectra of thin film Si (red line), 2 $\mu m$ (green line) and 5 $\mu m$ long (black line) Si NW array solar cells are compared in fig. 1.20(b). A strong transmittance suppression is observed for Si NW arrays due to light trapping mechanisms induced by their roughness and reflective index fluctuation. A light trapping path length enhancement factor between 1.7 and 73 with respect to Si was measured over the entire solar spectrum depending on the nanowire geometry. Therefore, vertically-aligned Si NW arrays represents a viable path toward high-efficiency, low-cost thin-film solar cells by providing a way to reduce both the quantity and quality of the required semiconductor.

### 1.2.4 Sensing

In the last decades, the important task of analytic detection has been extensively studied for different application fields, especially for biomolecules and specific markers detection towards the analysis of dangerous volatile organic gases or explosive traces. The high aspect ratio, biocompatibility and the unique features of Si NWs configure this material as a very promising platform for highly sensitivity and tailored selectivity sensors for biomedical and safety applications [68]. The development of fast, label-free and low-cost Si NW sensors is a rapidly expanding field [48] and either DNA and cancer markers detection are particularly appealing. As an example, Zheng et al. developed an innovative NW biosensor for the simultaneous detection of different analytes, consisting of 200 individually addressable p- and n-type Si NW-FETs integrated on the same device [69].

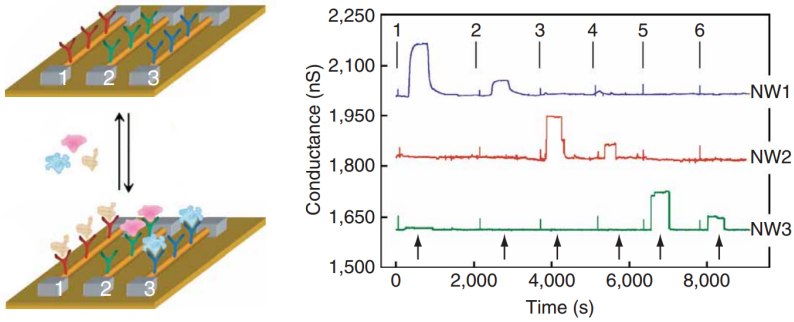


(a) (b)

*Figure 1.21: (a) Illustration of multiplexed protein detection by a three p-Si NWs array, each one functiontionalized with distinct mAb PSA (1, red), CEA (2, green) and mucin-1(3, blue) receptors respectively, to selectively detect three different cancer markers. (b) Conductance versus-time data acquired simultaneously for the detection of PSA, CEA and mucin-1 respectively fro NW from 1 to 3. The solutions were delivered to the nanowire array sequentially as follows: (1) 0.9 ng/ml PSA, (2) 1.4 pg/ml PSA, (3) 0.2 ng/ml CEA, (4) 2 pg/ml CEA, (5) 0.5 ng/ml mucin-1, (6) 5 pg/ml mucin-1 [69].*

Three functionalization steps were performed to covalently link antibody receptors and oligonucleotides to the NW surfaces. The NW surface was first cleaned in oxygen-plasma and functionalized with aldehyde groups and followed by aldehyde propyltrimethoxysilane (APTMS) coverage. The solution of monoclonal antibody (mAb) receptors specific for cancer protein markers were anchored to APTMS onto different regions of the array by using flexible poly dimethylsiloxane polymer fluidic channels sealed to the device chip and the unoccupied aldehyde groups were blocked with ethanolamine. The multiplexed detection of cancer marker proteins is reported in fig. 1.21 for a three p-Si NWs array sensor. Each wire was functionalized with receptor-specific monoclonal antibodies for prostate specific antigen (PSA) in red, cancer embryonic antigen (CEA) in green and carcinoma associated mucin (mucin-1) in blue, respectively. When the protein solutions are injected into the sensor, the electrical conductance of the NW is dramatically changed due to the local carrier concentrations variation occurring along the wire surface. The NW array conductance data demonstrate the simultaneous detection of PSA, CEA and mucin-1 when the protein solutions were sequentially delivered as follows: (1) 0.9 ng/ml PSA, (2) 1.4 pg/ml PSA, (3) 0.2 ng/ml CEA, (4) 2 pg/ml CEA, (5) 0.5 ng/ml mucin-1, (6) 5 pg/ml mucin-1. A high sensitivity is demonstrated over three order of magnitudes for all protein detection, demonstrating the efficiency of the specific functionalization.

Another route to take advantage of nanowires incredible morphological and optical potential is the realization of metal decorated-Si NWs for Surface-Enhanced Raman Spectroscopy (SERS) [70, 71]. A higher metal nanoparticles (NPs) density is obtained on metal decorated-Si NWs due to their huge aspect-ratio, hence the SERS performances on 3D platforms of metal-decorated Si NWs are greatly improved compared to standard flat substrates.

The SERS potential of metal decorated Si NWs allows to rapidly detect very low concentrations of organic molecules thanks to the excitation of localized surface plasmon resonances (LSPR). Indeed, the resonant plasmonic excitation of optically coupled metal NPs enhances the incident electromagnetic field by several orders of magnitude strongly amplifying the Raman fingerprint of the molecule.

Usually, Ag and Au are the most adopted metals for decoration due to good integration with Si systems. Moreover, both metals present a visible plasmonic resonance that is of interest for applications. The metal decoration of Si NWs can be obtained using both chemical (galvanic reduction [72], chemical bath [73]) and physical approaches (pulsed laser deposition, laser annealing, evaporation and sputtering [74, 75]).

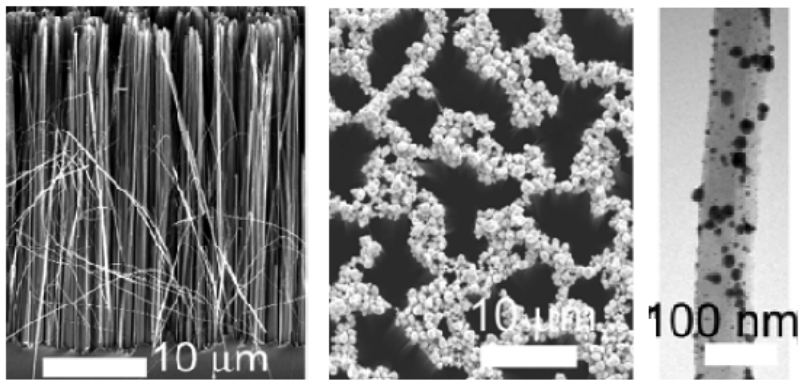


(a) (b) (c)

*Figure 1.22: (a) SEM cross-section image of a 32 µm long Si NW array realized by $AgNO_3$ assisted chemical etching. (b) PLan-view SEM image displaying the NW tips decoration by Ag nanoparticles chemically deposited. (c) TEM microscopy of the bottom section of a single NW. [76].*

Chemical processes are the most adopted decoration approaches due to their low-cost and fast processing time. These decoration mechanisms involve the direct chemical synthesis of metal NPs on the Si surface due to Si reduction in presence of noble metal/HF mixture solutions [73]. During the redox reaction Si oxidizes into $Si_4^+$ and the reduction of $Ag^+$ or $Au_3^+$ ions occurs, producing metal clusters that are directly deposited onto the Si surface. The metal decoration of Si NWs by surface mediate redox reaction has been demonstrated by using either $AgNO_3$ or $NaAuCl_4$ solutions, resulting in a dense distribution of Ag or Au NPs with size and interparticle distance of a few nanometers [77]. Although Si NW surface functionalization can alter the metal NP growth leading to different NPs morphologies, chemical decoration approaches scarcely control the deposition

site and the structural properties of metal NPs. As a consequence, metal NPs are unevenly distributed along the wires and especially concentrated on the NW tips due to the vertical geometry of the array. However, a better control over the NPs parameters is generally offered by physical approaches as exploited in chapter 5.

Indeed, the ultrasensitive SERS detection of pesticides, bacteria and other biomolecules on metal decorated Si NW array has been proved by many groups. Zhang et al. [76] reported the potential of Ag decorated Si NW arrays for high sensitive SERS detection of cancerous dyes and their dangerous derivates employed for plastics and paint production. Si NW arrays prepared by $AgNO_3$ salts MACE (fig. 1.22 (a)) were decorated with silver nanoparticles by immersing the NW in a $HF : AgNO_3$ (0.5 M: $10^{-4}$M) solution under constant and gentle stirring. The silver salts dissolution lead to Ag nanoparticles agglomeration and subsequent deposition onto the Si NW surface. An efficient metal NPs coating is demonstrated by this approach, as reported by the SEM and TEM in fig. 1.22 (b),(c). Ag NPs are bigger and present higher density on Si NW tips with respect to the bottom region of the wires and their diameter is in the range between 4 and 20 nm. TEM analysis also confirmed that no impurities are present at the Si/Ag NPs interface, moreover NPs present a clean surface that is preferred for chemical binding.

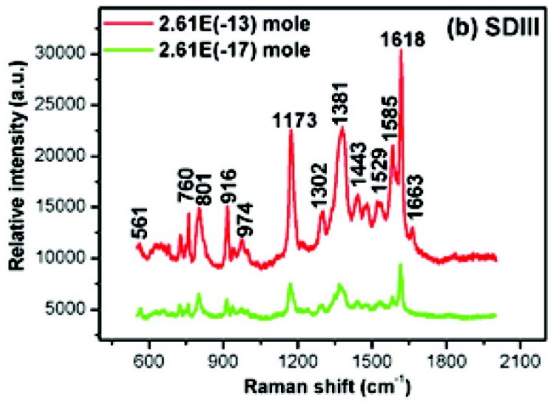


*Figure 1.23: SERS spectra acquired on Ag decorated Si NW arrays demonstrating the detection of* $10^{-13}$ *M (red curve) and* $10^{-17}$ *M (green curve) of SDIII Sudan dye [76].*

The SERS performances of Ag-decorated Si NW arrays were tested for the detection of a series of cancerous Sudan dyes (SDI, SDII, SDN, and SDG) whose use is banned for health safety. One microliter of solution containing different concentration of SDI dye diluted in ethyl acetate was casted on each SERS sensor with dimension of $3\times3$ mm$^2$. The SERS enhancement factors of about $10^8 - 10^{10}$ obtained from the resonant excitation of Ag NP plasmons allowed the detection of very low SDIII molar concentration down to $10^{-17}$ M, as shown in fig. 1.23.
Therefore, Si NWs confirm their great attitude toward the ultrasensitive detection of molecules on both as prepared and metal decorated arrays.

## 1.3 Conclusion

The main top-down and bottom-up strategies for Si NWs synthesis have been presented in this chapter. A special insight on Si NWs growth by the most common VLS technique based on the thermodynamic evolution of metal/Si alloys has been given. Si NWs fabricated by VLS have limited applications in electronics, photovoltaics and photonics due to detrimental effects introduced by the metal precursor used for the process. Indeed, Au and other metal catalysts commonly adopted for VLS diffuse into the wires and introduce deep energy levels responsible for non-radiative recombination. Moreover, NW doping is hardly controlled by in-situ processes and the dopants concentration varies along the radial profile of the wires. These issues affects both optical and electrical properties of these interesting new materials preventing practical applications. In order to overcome these drawbacks new strategies for Si NWs synthesis have been exploited and many groups reported NW fabrication by either using lithography and reactive ion etching processes. EBL is a powerful technique to achieve wires with controlled dimension and position, fully compatible with CMOS processing. However it is very expensive and requires long processing time that prevents its feasibility on a wafer scale.
Among others, the metal assisted etching approach is emerging as a preferred method for Si NWs realization. This top-down approach based on chemical oxidation of silicon through a metal catalyst and a subsequent removal of oxidized silicon through an HF bath is a fast, cheap and scalable process for the growth of NWs with controlled doping and structural features.
The state of the art of Si NWs integration in nanodevices with improved functionality has been also presented. Indeed, the innovative optical and electrical properties combined with NW high aspect ratio promote their employment for reconfigurable field effect transistors, broadband photodetectors and radial solar cells thanks to their strong light trapping properties. Moreover, NWs with diameter of a few nanometers are a promising building block for low-cost Si photonics. Another emerging field of integration for Si NWs is provided by their sensing potential, enabling the multiplexed and selective detection of biological species down to molar concentration well below the stan-

dard. Their clear electrical response and surface sensitivity strongly encourage a deeper integration among physics, chemistry and biology, moreover metal decorated Si NW arrays open the route towards the ultrasentitive SERS detection of low concentration of dangerous biomolecules.

# Chapter 2

# Silicon nanowire based multiwavelength light emitting sources

**Abstract**

*Silicon nanowires represent one of the most promising resources to be employed in modern nanodevices. Nevertheless their fabrication is still quite complex and challenging as demonstrated in the previous chapter. In chapter two the realization of Si NWs by using a low cost, industrially compatible and highly controllable method is reported. By optimizing the metal assisted chemical etching through the use of discontinuous thin metallic layers, it is possible to tune NW length and diameter. By simply varying the thickness of the metallic layers a fine control on NW radius on the scale of a few nanometres is obtained, well below the quantum confinement threshold for Si. Moreover Si NWs maintain the same crystalline structure and doping of the starting substrate, a fundamental feature for device implementation. The fabrication of Si NWs is presented here, describing the relationship among structural features and growth conditions in detail. The realization of low cost Si-based light emitting sources is attracting great interest in the scientific community. Ultra thin NWs with a diameter below tens of nanometres open the routes towards the observation of remarkable quantum confinement effects. The optical properties of Si NWs, such as tunable visible optical emission at room temperature, are investigated.*

*Furthermore the realization of innovative, low cost, Si technology compatible multiwavelength light sources operating at room temperature obtained by embedding a carbon nanotube (CNT) dispersion inside a Si nanowire array is discussed. The NW/CNT hybrid system exhibits a tunable emission both in the visible range due to Si NWs, and in the IR from CNT, a strategic range for telecommunication. The conditions leading to the prevalence of the visible or the IR signal have been identified and are herein discussed.*

## 2.1 Thin metal film assisted chemical etching

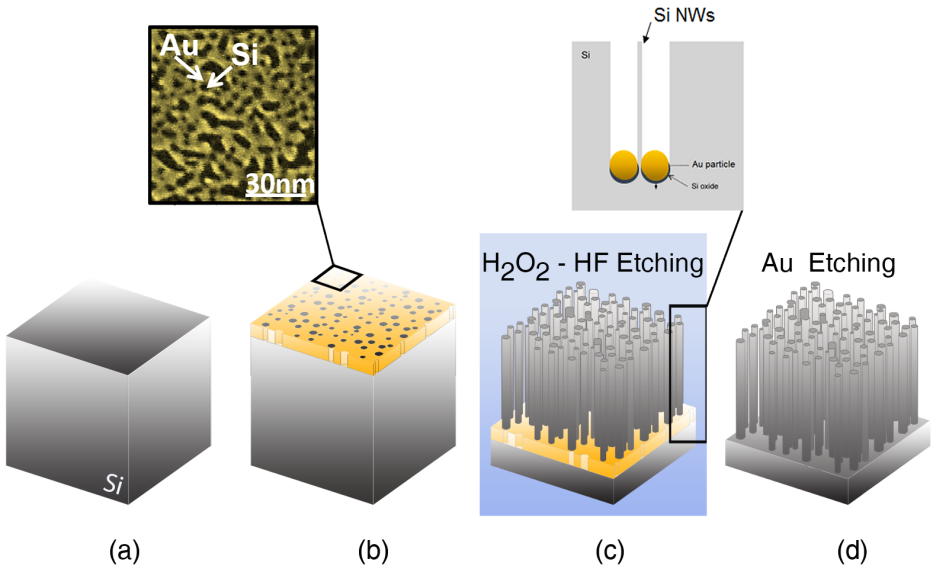


*Figure 2.1: Etching scheme of metal assisted chemical etching of Si NWs by using ultra thin layers of metal as catalysts. The inset shows a plan-view SEM image of the thin gold layer used for the etching.*

The synthesis of silicon nanowires is realized by thin metal film assisted chemical etching (MACE). This approach is based on the wet etching of silicon wafers and it has been revealed as a powerful tool to obtain a fine control on the NWs structural properties by tuning the process parameters.
Si wafers were UV-oxidized for 2 min and then dipped in a 5% aqueous solution of fluoridric acid (HF) for 5 min in order to achieve an oxygen-free surface. A 2 nm-thick Au layer was deposited on Si samples by using EBE evaporation, as depicted in the representative scheme in fig. 2.1. The room temperature evaporation of thin metallic layers results in a percolative film [78] leaving some uncovered Si areas that are responsible for the successive formation of silicon nanowires. The deposited samples were immersed in an aqueous solution made of $H_2O_2$ (0.44 M) and HF (5 M) for Si NWs formation, fig. 2.1. When immersed in this solution a selective oxidation re-

action occurs at the Au/Si interface, induced by the difference of electronegativity among the two materials. Indeed the metal withdraws electrons from Si (or equivalently injects holes) leading to the localized formation of a thin layer of $SiO_2$ only underneath the metal covered regions, that is subsequently etched by HF and dissolved into the liquid phase [62], [61].
As represented in fig. 2.1, the metallic layer sinks into the bulk while the uncovered silicon regions form Si NWs. One of the major advantage of this process is that, being entirely performed at room temperature, the Au precursor is not incorporated into the NW array. In fact it mainly remains confined at the bottom of SiNWs and can be easily removed by a potassium iodide (KI) and iodine ($I_2$) solution. This is an extremely important feature of this process that prevents the presence of Au atoms inside the NWs that could determine the presence of non-radiative phenomena. Moreover most of current techniques for NW synthesis based on VLS or lithographic processes are hardly capable of producing wires of a suitable size to exhibit quantum confinement effects and thus Si light emission [23]. Therefore the absence of Au-contamination inside the wires and the fine control over the NW doping that is the same of the starting bulk are only some of the great advantages obtained by this approach.
The proposed MACE method is a cheap and maskless process for the synthesis of a vertically aligned high density array of Si NWs that guarantees a high control on the structural and optical features [62]. Being a wet etching process it is easily implementable in large scale Si technology and it allows to maintain the same doping quality and crystalline orientation of the silicon bulk. Figure 2.2(a) displays a tilted SEM cross-section of Si NWs having length of 2.5 $\mu m$ showing a high density array of $10^{12} NW/cm^2$ with a surface coverage of about 50%. Si NWs with dimension ranging from few hundreds of nm up to a few tens of $\mu m$ can be synthesized simply varying the etching time from approximately 2 min to 1h. A uniform NW array displaying the same length is achieved within a high grade of accuracy of about 5% as reported in fig. 2.2(b) from the cross-section view of a 3 $\mu m$ long Si NW array realized by MACE from a 2 nm deposition of Au.

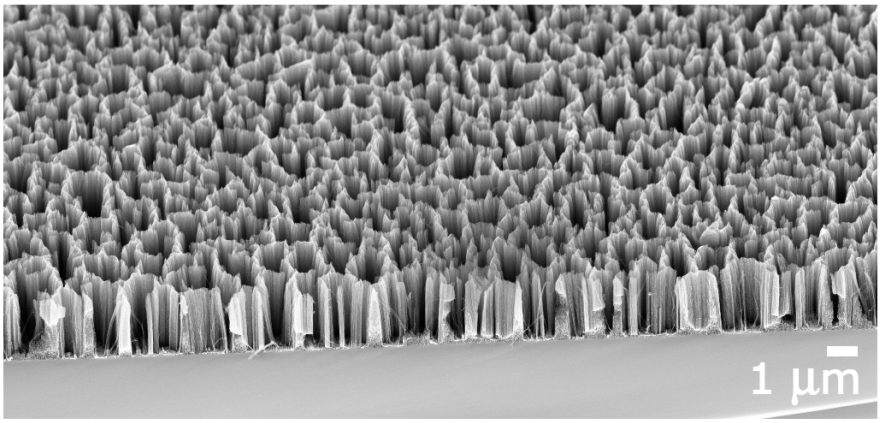


(a)

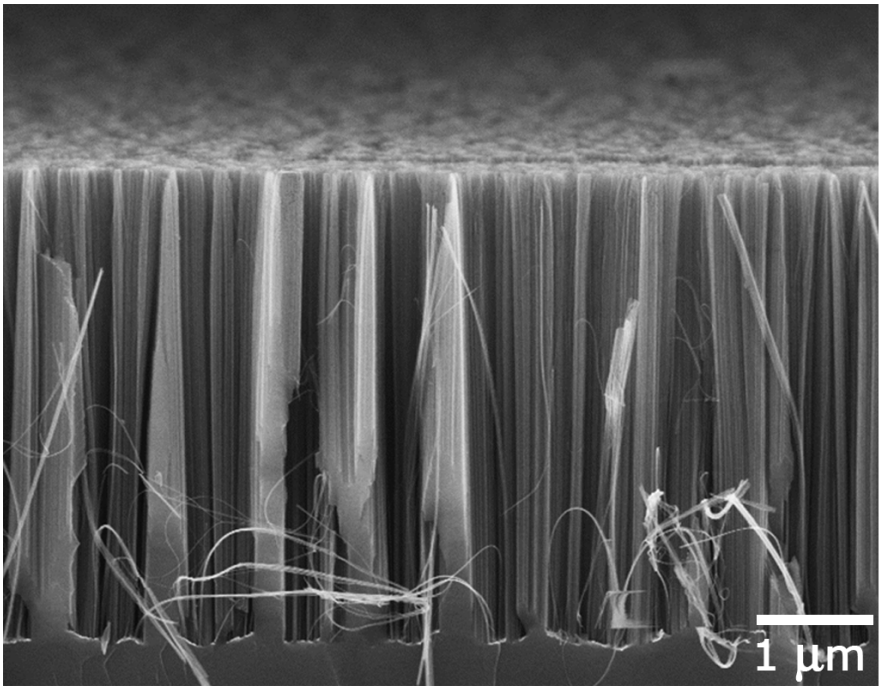


(b)

*Figure 2.2: (a) SEM tilted cross-section displaying 2.5 µm long Si nanowires fabricated by metal assisted chemical etching on (100)-oriented Si substrate deposited with 2 nm of Au. (b) SEM Cross-section of a high density array of vertically aligned Si NWs having 3 µm length.*

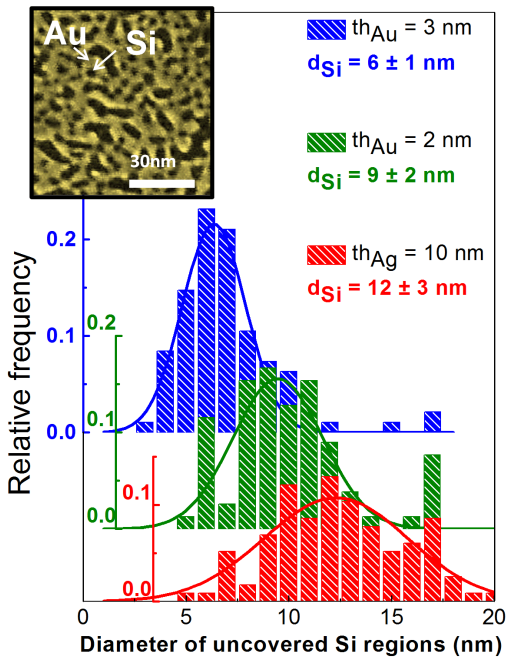


*Figure 2.3: Statistical analysis of the mean diameter of Si uncovered regions for a deposition of percolative layers of 3 nm and 2 nm of Au, and 10 nm of Ag respectively. A representative SEM plan-view of a 2 nm of Au film deposition (yellow areas) on silicon (dark regions) is shown in the inset [62].*

The statistical analysis of the mean diameter of Si uncovered regions as a function of the thicknesses of the metallic layers is reported in fig. 2.3. The top inset shows a SEM plan-view of a room temperature EBE deposition of 2 nm percolative layer of Au on silicon. For clarity gold areas are marked as yellow and Si ones as dark regions. The results are collected from different SEM images performed on the same samples. A mean diameter of $12 \pm 3nm$ is achieved for a deposition of 10 nm of Ag, $9 \pm 2nm$ and $6 \pm 1nm$ for a deposition of Au of 2 and 3 nm respectively. Therefore demonstrating that the diameter of the uncovered Si areas can be varied in a manageable way by changing the thickness of the deposited metal. The thickness difference among Au and Ag layers is related to different wettability of the metals on silicon surface. When deposited on Si, silver atoms aggregate in bigger hemispherical clusters [78] forming a smaller angle of contact at the interface with respect to Au.

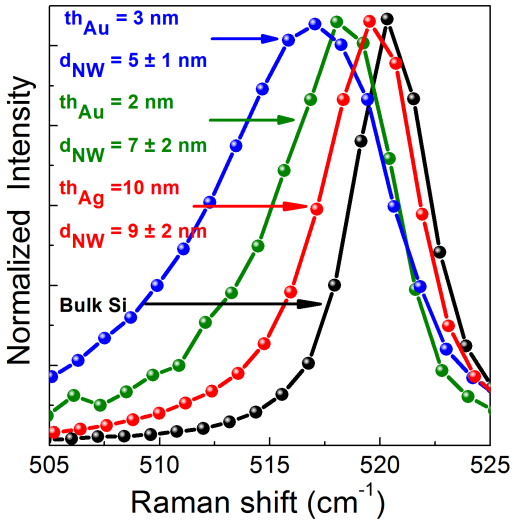


*Figure 2.4: Raman spectra of Si NWs obtained by using Au layers having a thickness of 3 nm (blue) and 2 nm (green) and Ag layer having 10 nm (red) respectively compared to the Raman spectrum of bulk crystalline Si (black) [62].*

Indeed a thicker Ag layer is needed to obtain a percolative layer for the formation of ultra thin NW with diameter below the confinement threshold of ten nanometers. In fig. 2.4 the Raman spectra of Si NWs obtained from different metal deposition thicknesses are reported. NW Raman peaks are asymmetric and visibly shifted if compared to the symmetric Si bulk signal (black). The asymmetry and the Raman peak shift are two typical features of quantum confined Si nanostructures, as also demonstrated from Piscanec work for Si NWs [79]. To estimate the NW diameter the Raman spectra have been fitted using the Ritcher-Campbell-Fauchet model for quantum confined nanowires [80, 81]. A mean diameter of $9\pm2$ nm has been estimated for an Ag deposition of 10 nm, while mean values of $7\pm2$ and $5\pm1$ nm are calculated for a deposition of 2 and 3 nm of Au respectively [62]. A strong control on NW diameter has been demonstrated by finely varying the thickness of the metallic precursor layer.
A crucial role is played by the size of the Si uncovered areas that is strictly connected to the NW diameter. Therefore to select NW diameter a good control on the Si uncovered areas is required.

As a matter of fact, NW diameter values are very close to the mean values of the Si uncovered regions proving that NW diameter can be simply controlled by varying the thickness of the metallic layers. Therefore, this is an innovative approach to select NW diameter as a function of the thickness of the metallic layer and to obtain a suitable size for the occurrence of quantum confined phenomena.

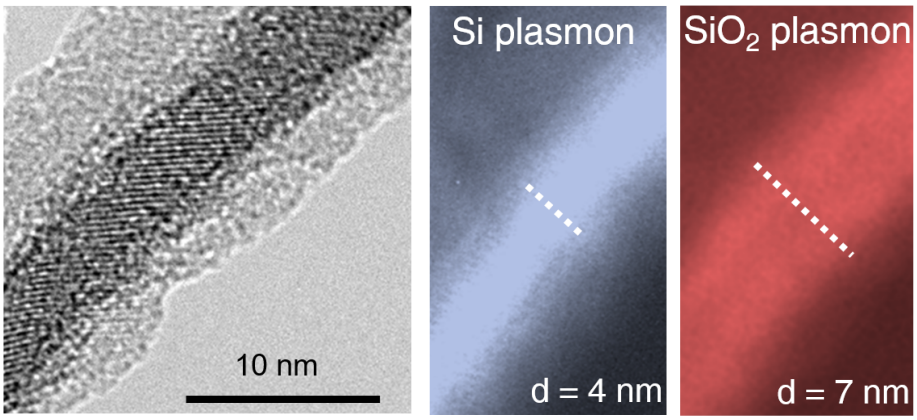


(a) (b) (c)

*Figure 2.5: (a) High resolution bright field TEM image performed on a single NW. EFTEM microscopies of the same NW have been obtained by detecting the Si plasmon energy loss, as reported in panel (b) and $SiO_2$ plasmon loss in (c) [62].*

The Raman analysis on NW diameters were further confirmed by TEM investigations. As observed in fig. 2.5(a) Si NWs realized by this method have diameters below ten nanometers. Moreover it is possible to observe the realization of nanostructure, having the same crystalline orientation of the starting Si bulk.
Additional structural details have been obtained by energy filtered transmission electron microscopy (EFTEM) analysis performed on the same wire as shown in fig. 2.5(b) and fig. 2.5(c). The EFTEM microscopy displayed in fig. 2.5(b) is obtained by selecting the electron signal with energy loss tuned to the Si plasmon (16 eV). Si plasmon peak is spectrally well resolved from $SiO_2$ bulk plasmon (tuned at 24 eV) as reported in panel (c). The $SiO_2$ region (7 nm) is larger than the Si one (4 nm) and the presence of a $Si/SiO_2$ core-shell structure is clearly distinguishable.

Moreover the Si (100)-lattice planes are only appreciable in the 4 nm diameter NW core. This core-shell structure is induced by the formation of a nanometric $SiO_2$ layer due to air exposure of highly reactive Si dangling bonds after the etching. The Si NW core is embedded in an outer $SiO_2$ shell with total mean diameter of 7 nm as shown in fig. 2.5(c) [62].

## 2.2 Optical properties of silicon nanowires

For a long time silicon has been considered unsuitable for optical application for the indirect nature of its electronic band gap. In indirect semiconductors the radiative recombination of an electron-hole pair is a three particles process, involving the presence of a phonon as a third particle to preserve the crystalline momentum conservation. Non-radiative de-excitations are $10^6$ times more probable to occur than radiative ones.
In literature many other groups have reported photoluminescence (PL) emission from Si NWs mainly induced by the presence of emitting dopant agents, for example N-containing complexes [82]. Demichel et al. exploited the light emission of Si NWs induced by phonon-assisted low temperature recombination of photogenerated carriers [83]. A possible solution to achieve room temperature emission from silicon is presented by quantum confinement effects. When the radial dimension of the wire is comparable with the exciton Bohr radius, a relaxation of the dispersion relation is verified with a strong increase of the oscillation strength, thus allowing the occurrence of radiative transitions with comparable probability to non-radiative ones. In the previous works the light emission is clearly not related to the occurrence of quantum confinement phenomena since NW size is too large to induce such an effect. In fact there are only a few studies reporting on room temperature PL from NWs whose size has been reduced by poorly controllable oxidation processes [84, 35, 85]. Moreover electrical pumping is not achievable by this approach.
Si NWs synthesized by metal-assisted etching using thin layers of gold or silver are efficient light emitters at room temperature (RT).
This behaviour is attributed to the presence of quantum confinement phenomena, as demonstrated in the following section.

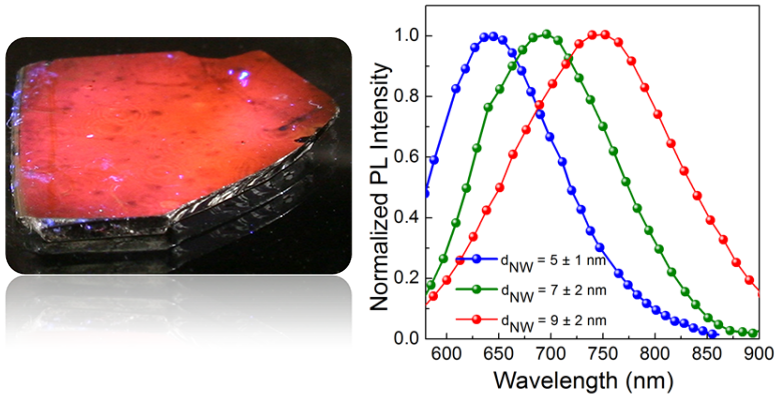


(a) (b)

*Figure 2.6: (a) Photograph of a Si NW sample having an area of about* $1cm^2$ *excited by the 364 nm line of a fully defocused* $Ar^+$ *laser beam showing a bright red PL emission clearly visible to the naked eye. (b) Room temperature PL spectra obtained by exciting Si NW samples of different sizes with the 488 line of an* $Ar^+$ *laser at a pump power of 10 mW [62].*

The major demonstration of the occurrence of quantum confinement in Si NWs is given by a remarkable room temperature photoluminescence. In fig 2.6 (a) a photograph of a 2.5 $\mu m$ emitting Si NW array is obtained by defocusing the 364 nm line of an $Ar^+$ laser on the sample. A very bright red emission from the NWs is observable to the naked eye. Figure 2.6 (b) reports the PL spectra of 2.5 $\mu m$ long NWs of different diameters acquired by exciting with the 488 nm line of an Ar laser at a pump power of 10 mW. The spectra consist of a broad band emission exhibiting a full width at half maximum comprehended between 125-200 nm due to the NW size distribution. In particular the PL peak is centered at about 750 nm for 9 nm diameter NWs, while it is clearly blue shifted towards 690 nm for 7 nm diameter NWs and further shifted to 640 nm for NWs of the size of 5 nm. According to quantum confinement theory the energy gap of the NWs increases as the inverse function of the square radius if considering the model of particles in a finite 2D well potential. Therefore by reducing the wire size a blue shift of PL is expected. From the graph it is evident that the emission wavelength shifts as a function of the NW mean size, an exquisite quantum effect in agreement with confinement theory [61, 86].

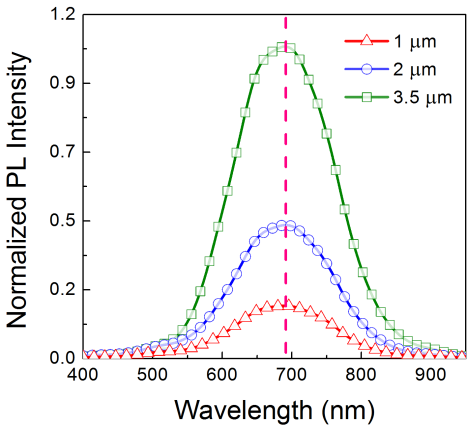


*Figure 2.7: PL spectra of Si NWs array of length 1 um (red line-triangles), 2 um (blue line-circles) and 3.5 um (green line-sqaures), obtained by exciting the system with the 364 nm line of an Ar+ laser at a pump power of 60 uW.*

Another evidence of the presence of quantum confinement effects is given by the lifetime and PL trend as a function of time. Newly formed NWs are not yet oxidized and a $SiO_2$ shell is formed after air exposure, thus increasing the effectiveness of the spatial confinement. This phenomenon of surface passivation acts reducing any superficial non-radiative recombination centers present in the newly prepared samples. Therefore, it has been observed that the lifetime of the system and the PL intensity increase as a function of time until the stability conditionn is reached, as expected from the occurrence of passivation in nanostructures [87]. Fig. 2.7 displays the room temperature PL spectra of Si NWs having a diameter of 7 nm but different lengths ranging from 1 to 3.5 $\mu m$. Each PL spectrum consists of a broad emission band with the same FWHM of 160 nm due to the NW size distribution that is to ascribe to the morphology of the 2 nm thick Au precursor film. From the spectra it is evident that longer NWs exhibit a more intense emission that linearly increase with the length. Indeed a huge ensemble of emitting centers is present in a single wire, therefore the longer the NW is the more electron-hole pairs are present [88, 89].

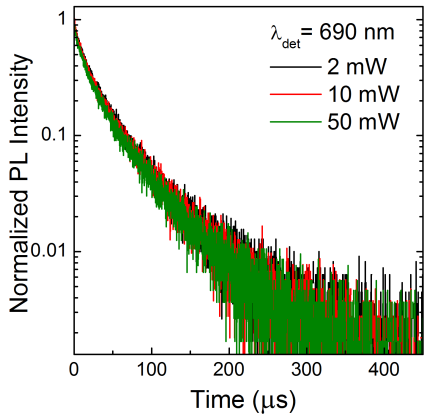


*Figure 2.8: Lifetime of PL decay signal for a Si NW sample emitting at 690 nm measured by exciting the system with the 488 nm line of a Ar+ laser at different pump powers [62].*

A crucial aspect for photonic application is related to the presence of non radiative phenomena. As an example Si nanocrystals are greatly affected by the occurrence of Auger recombination thus limiting their range of utilization. In particular Auger phenomena are strongly affected by the density of carriers and are more marked at higher power. The decay time of the PL signal measured as a function of the pump power from 2 mW to 50 mW is displayed in fig. 2.8. A 2.5 $\mu m$ long NWs system of 7 nm diameter has been pumped with the 488 line of an $Ar^+$ laser and the de-excitation of the PL signal at 690 nm after the laser shut-off has been measured.
As observed from fig. 2.8 the lifetime of Si NWs does not vary by increasing the laser pump power, proving that in this material non-radiative phenomena are not efficient [90]. NWs have very high aspect ratio and so radiative recombination may occur in points of the wire that are very far from each other, thus suppressing the probability of interactions between different electron–hole pairs by non-radiative effects [62]. The PL decay data were then fitted with an exponential function, measuring a typical de-excitation time of about 25 $\mu s$ for these NWs. An external quantum efficiency of the system higher than 0.5% has been measured, a comparable value with efficiencies reported for porous Si [91] and Si nanocrystals [92].

## 2.3 Synthesis and optical properties of carbon nanotube dispersions

A new frontier for photonics is given by the fabrication of multifunctional devices. Particularly interesting is the realization of cheap multiwavelength light sources working at room temperature and compatible with Si technology [93].
The following sections is focused on the realization of Si NW-based multiwavelength light sources operating at room temperature. Such light emitters have been fabricated by embedding a carbon nanotube dispersion inside a Si nanowires array. In this frame carbon nanotubes (CNT) appear as a promising nanomaterial to be employed in a large variety of fields for their outstanding electrical, mechanical and optical properties [94, 95]. In fact the employment of CNT in microelectronics [96], solar cell [97, 98], photonics [99, 100] and sensing devices is today very well reported in literature.
Nanotubes are produced in a large variety of structures, from single-walled tubes (SWCNT) formed by the rolling of a single graphene sheet, double and multi-walled tubes (MWCNT) formed by a series of graphene sheets rolled along the same axis.
For our purpose were used single-walled carbon nanotubes (SWCNT) that are considered the most promising CNT candidates for miniaturized application with respect to others. In fact to obtain MWCNTs having the same structures is much harder than for SWCNTs.
Most of SWCNTs have a diameter below a few nanometers and can be several times longer on the scale of hundreds of micrometers, showing an impressive aspect ratio of about $10^4 - 10^5$ . SWCNTs are almost 1D nanostructures formed by the wrapping of a single graphene sheet on a well defined axis with a specific angle, the chiral angle $\alpha$. The roll-up direction is uniquely identified by the chiral vector $C_h = n\mathbf{a_1} + m\mathbf{a_2} \equiv (n, m)$, where $\mathbf{a_1}$ and $\mathbf{a_2}$ identify the graphene lattice vectors and $n$ and $m$ are two integers [101]. $C_h$ and the tube radius play a key role determining the dispersion relation of the tube and thus all of its physical properties.
Therefore single-walled tubes represent a unique class of CNT since their electronic and optical properties can be varied with their structural parameters [102, 103].

In fact, CNTs electrical conductivity may present a metallic or semiconducting behavior. SWCNTs satisfying the following equation 2.1 are metallic and do not present any appreciable energy gap.

$$n - m = 3q \quad where \quad q = 0, 1, 2, 3, ... \tag{2.1}$$

For all of the other (n,m) combinations a significant band gap is observed and a semiconducting behavior is reported.
Moreover SWCNT band gap can vary from zero to about 2 eV.

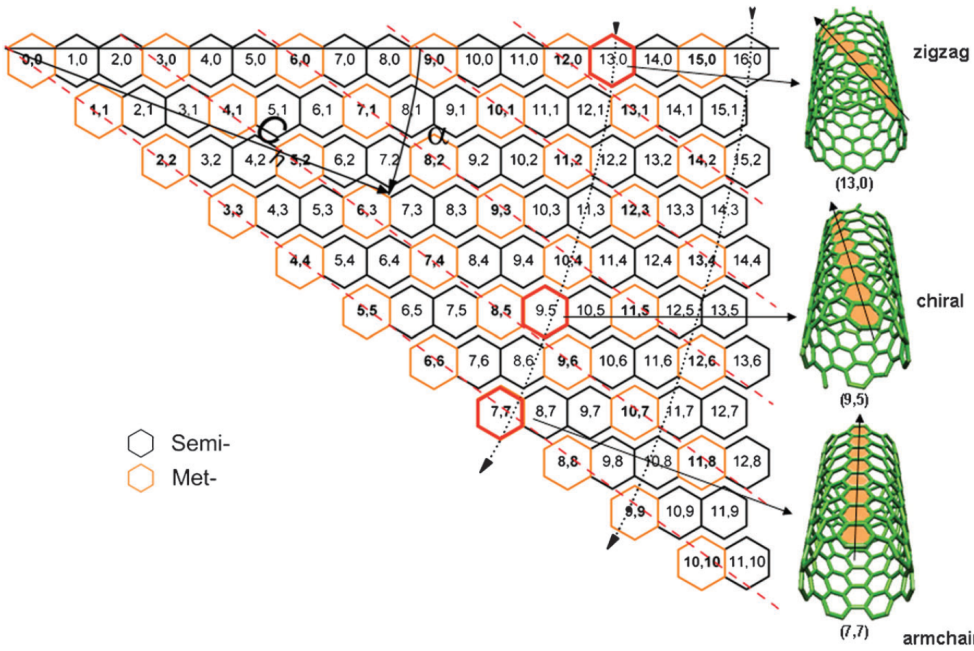


*Figure 2.9: Chirality map of SWCNTs displaying the metallic (orange hexagons) and semiconducting nature (black hexagons). [104] .*

A map of different CNT chirality arrangements labeled according to their chiral indices (n,m) is reported in fig. 2.9. Metallic families are highlighted in orange hexagons, while semiconducting ones are black marked. Metallic tubes are identified by parallel red dashed lines, while the types between these lines are all semiconducting. The main three typical SWCNTs configuration are displayed along the right side of the chirality plot.

Indeed, all (n,n) families are called armchair and are metallic, while all (n,0) are zig-zag types and among these, those having (3n,0) are metallic and those otherwise results semiconducting. The other remaining (n,m) chiral configurations can have either behavior. The two black dotted lines outlines all SWCNTs with diameters ranging between 1.0 and 1.2 nm
CNTs can be easily synthesized through several methods like arch-discharge, laser ablation and CVD. Nonetheless most of these techniques produce CNT networks or arrays where CNT agglomerate in bundles. Bundle formation is caused by the Van der Waals forces acting among adjacent tubes and represents a critical issue for CNT optical and structural properties. These bundles strongly affect CNT light emission limiting their implementation in photonics due to the occurrence of energy transfers among adjacent tubes of the same bundle. Particularly crucial is the presence of metallic and MWCNT in the bundle, for which no optical emission is observed.

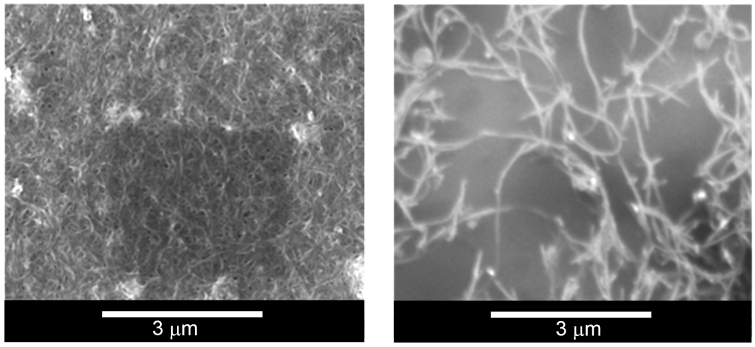


(a) (b)

*Figure 2.10: (a) SEM images of SWCNT bundles shown after 15 min of centrifugation at 6000 rpm and (b) after using a debundling procedure in DEC surfactant after 15 min of horn sonication [105].*

Therefore a good debundling procedure is needed to achieve an efficient optical emission from CNT. Several debundling approaches are well documented in literature by using different dispersing media [106, 107]. Some of the most effective debundling procedures involve covalent functionalization of CNT surface by using surfactants. Surfactants are generally amphiphilic organic compounds, made of a polar hydrophobic tail and of a hydrophilic head.

When immersed in water, surfactants aggregate forming micelles. In these structures the hydrophobic tails align toward the inner part while the hydrophilic heads face the surrounding liquid. Other types of aggregates can also be formed, such as spherical or cylindrical micelles or lipid bilayers. Micelles interact with CNTs wrapping their surface, drastically reducing the Van der Waals interaction and bundle formation. In fig. 2.10 are reported two SEM images of a CNT powder dispersed in water (a) and in 10 mg/l Dichloroethane (DEC) surfactants (b) by using a 15 min horn-sonication and a 6000 rpm centrifugation. It is clearly visible from a first comparison that the enveloped CNT network present in (a) is unravelled by this procedure, leading to the formation of smaller bundles [105]. The debundling procedure adopted to obtain a stable SWCNT dispersion is reported in fig. 2.11.

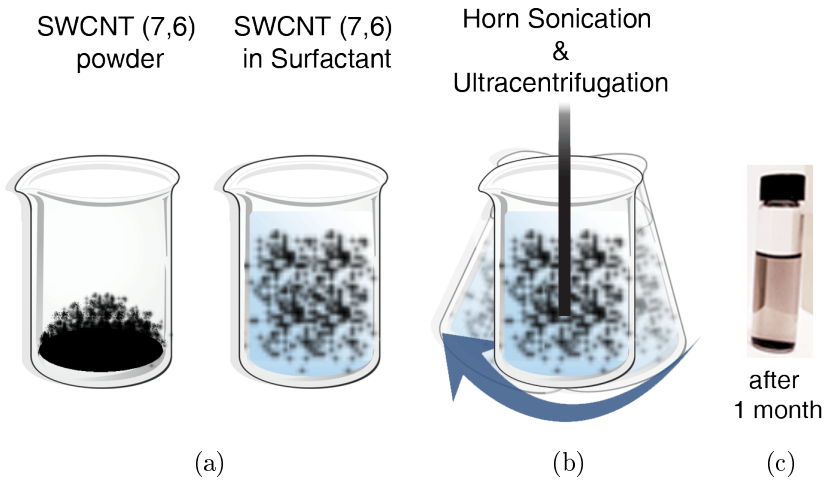


*Figure 2.11: Representative scheme of SWCNTs debundling procedure. (a) The CNTs powder was immersed into a TDC solution. The obtained dispersion was (b) horn-sonified for 30 min, filtered and then ultracentifugated for 45 min to achieve a stable dispersion of debundled CNT in surfactant. (c) Photo attesting the stability of the CNT dispersion after one month. [105]*

A CNT dispersion has been prepared by using commercially available powder of SWCNTs having diameter of 0.9 nm and a mean length of 700 nm [108]. SWCNTs present in the powder are mainly enriched in (7,5) and (7,6) semiconducting chiralities. Nonetheless the presence of other chiralities is detected, in fact as well known in literature single chirality CNTs are very hardly produced. To avoid bundles formation [103, 109, 110], 2 mg of CNTs were added to 10 ml of deionized water containing 0.2 g of taurodeoxycholic acid (TDC) as surfactant (fig. 2.11(a)). When immersed in the solution CNT surface is wrapped by surfactant micelles that act screening the bundling interactions among adjacent tubes. The mixture was then horn-sonicated for 30 min causing the precipitation of bigger bundles and carbonaceous residues. The precipitated products were further filtered and removed by a 45 min ultracentrifugation process, as depicted in fig. 2.11(b).
Well-dispersed CNTs and small bundles present in the surnatant (dispersion upper part) was extracted while larger bundles and insoluble impurities were removed. Figure 2.11(c) displays a photograph reporting the achievement of a clear and stable debundled CNT dispersion after one month. A concentration of about 0.5 mg/l of CNT was estimated from a comparison with similar standard debundling procedures present in literature [100, 111].
The detailed study on the optical properties of the achieved CNT dispersion is reported in the following analysis.

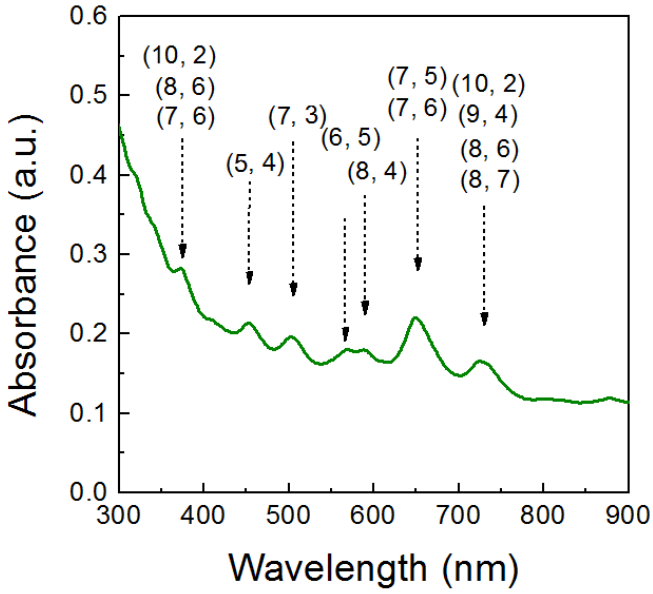


*Figure 2.12: Absorption spectrum of a 0.5 mg/l CNT dispersion presenting several chiralities of nanotubes [111].*

The optical properties of the 0.5 mg/l CNT dispersion has been investigated by using UV-VIS spectroscopy, PL and Photoluminescence excitation (PLE) as reported in fig. 2.12 - 2.14 respectively. The absorption spectrum in fig. 2.12 shows several absorption peaks, characteristic of the different CNT chiralities present in the dispersion. At 454, 504, 566 and 590 nm, the (5,4), (7,3), (5,4), (7,3) resonant absorption peaks are detected respectively. The 650 nm peak is given by the superposition from (7,5) and (7,6) absorption. While the 724 nm peak results from the undistinguishable (8,6) and (8,7) absorption.
It has been observed that TDC absorption is negligible in the analysed range. Thus the background appreciable at shorter wavelength is to be attributed to the excitation of CNT $\pi$ plasmons [102]. The CNT chiral families have been identified by cross-checking the characteristic absorption and emission peaks shown in fig. 2.12-13. All chirality assignments result in good agreement with theoretical predictions and experimental data reported in literature [103, 109, 110].

The presence of a chirality distribution does not represent a weak point for the debundling procedure, attesting instead its effectiveness to individualize CNT regardless of their chiralities. Moreover such a CNT chiral distribution allows for a wide range absorption, ranging from UV to visible wavelengths.

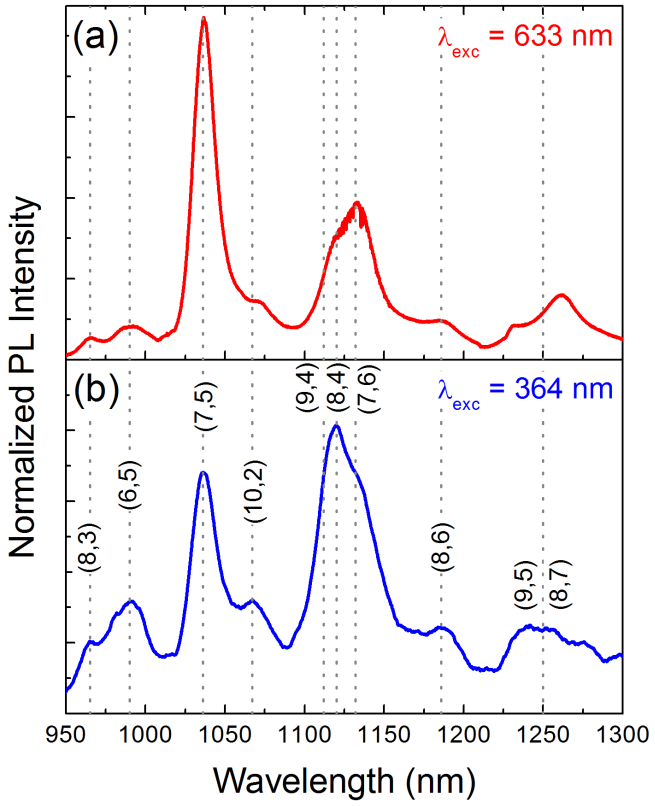


*Figure 2.13: Normalized PL spectra of a 0.5 mg/l CNT dispersion (a)obtained by exciting with the 633 nm line of a He-Ne laser and (b) with the 364 nm line of a $Ar^+$ laser. [111]*

PL spectra of a 0.5 mg/l CNT dispersion have been acquired by exciting it at the 633 nm line of a He-Ne laser and at the 364 nm line of an $Ar^+$ laser, as displayed in fig. 2.13(a) and (b) respectively. Both spectra were normalized for the acquisition conditions. The typical infrared PL emission from a CNT dispersion under both excitation wavelengths is reported in fig. 2.13. The CNT photoluminescence is induced by the the absorption of a UV/visible photon that pro-

motes an exciton formation at the highest unoccupied excitonic state $eh_{22}$ or $eh_{33}$ according to the used excitation wavelength. Several sharp PL peaks can be recognized in both spectra demonstrating that the same chiralities can be detected under the considered excitation modes, although relative intensities are quite different. As shown in fig. 2.12 and 2.13 both absorption and emission peaks are quite sharp. This is an evident feedback of the effectiveness of the adopted procedure to avoid the formation of large tubes bundles. Indeed sharp PL peaks are only observed in isolated nanotubes or in small bundles, in which non-radiative recombinations caused by energy transfers towards metallic species are minimized [100].
The observed emission peaks at 965, 990, 1035 and 1065 nm are associated to the (8, 3), (6, 5), (7, 5) and (10, 2) chiral families respectively. A broad emission between 1100-1150 nm is due to the superposition of (9, 4), (8, 4), and (7, 6) typical peaks. None of these emission peaks can be singularly resolved by the detection system for the adopted excitation wavelength, as later shown in fig. 2.14(a-b). The characteristic (8, 6) emission can be identified at about 1185 nm, while the broad peak at 1250 nm is given by the superstition from (9, 5) and (8, 7) emissions. Some differences among relative PL intensity peaks can be noticed when exciting the same CNT dispersion by using different wavelengths. Comparing the PL spectra in fig. 2.13(a-b) obtained by exciting the same CNT dispersion at different wavelengths some distinguishable differences among the relative PL intensities of the main emission peaks are observed. This effect can be understood considering that the involved transitions are stimulated in a different way by varying the excitation wavelength. A powerful tool to exploit the optical behavior of a material as a function of the excitation wavelength is given by photoluminescence excitation spectroscopy (PLE).
2D PLE maps acquired by using a spectrofluorimeter equipped with a Xenon Lamp are displayed in fig. 2.14(a-b). The PL emission from a 0.5 mg/l CNT dispersion is plotted in a false color scale as a function of the excitation wavelength in the 300–530 nm and in 530–750 nm ranges, as shown in fig. 2.14(a) and (b) respectively. The dash-dotted red lines identify the 364 and 633 nm excitation lines used to probe the PL emission from the CNT dispersion as shown in fig. 2.13. The intensity maxima visible in the maps correspond to the resonant

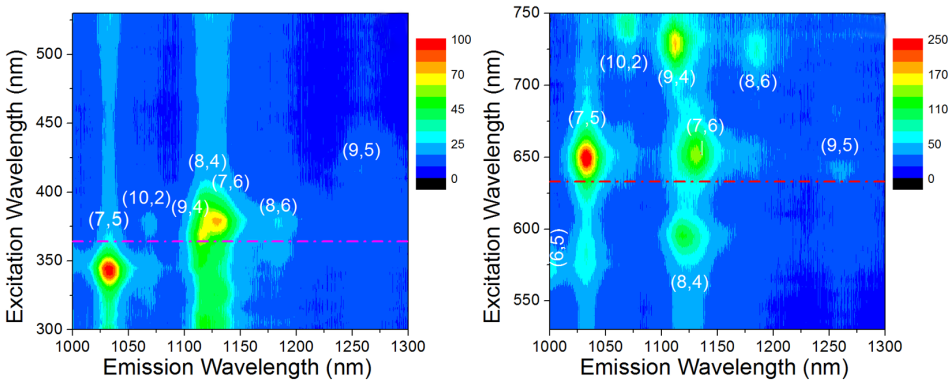


*Figure 2.14: 2D PLE maps plotting in a color scale the PL infrared emission as a function of the excitation wavelength for the 0.5 mg/l CNT dispersion. The 300–530 nm excitation range is shown in panel (a), while the 530–750 nm region is shown in panel (b) [111].*

excitation of the various CNT families. It is evident from the PLE maps that a change of the excitation wavelength deeply influences the shape and the intensity of the CNT dispersion PL spectra.
Indeed at lower excitation wavelengths a higher amount of energy is transferred to the system allowing the direct excitation of higher $eh_{33}$ states. In particular when exciting the system with the 364 nm wavelength the predominant emission is given by the resonant absorption inducing $eh_{33}$ transitions for the (9, 4), (8,4) and (7, 6) families which is above the (7, 5) excitation. Meanwhile, a lower amount of energy is handed over to the system when exciting in the visible range. In the latter case the resonant excitation of low energy states $eh_{22}$ and $eh_{11}$ dominates. The relative intensity among CNTs can be significantly inverted when exciting the system with red radiation at 633 nm. Indeed the resonant $eh_{22}$ emission from (7,5) family is predominant over all the other chiralities when pumping the system with the 633 nm excitation. Therefore fig. 2.14(a-b) evidence that (7,5) and (7,6) emission peaks are predominant over the other CNT emissions in the investigated range. In fig. 2.14 (b) the emission of (9, 4), (8, 4), and (7, 6) CNTs can be spectrally well resolved when the resonant $eh_{22}$ and $eh_{11}$ excitation conditions are matched.

This confirms that a substantial variation of the relative CNT intensity peaks can be produced by simply selecting the excitation wavelength. Furthermore the PL maps clearly attest the presence of a large ensemble of CNT different chiral family, assuring the absorption over a wide range of excitation wavelengths from 300 nm to 750 nm. The relative PL tunability gives an extra value to the CNT dispersion system as later remarked.

## 2.4 Realization of the silicon nanowire/ carbon nanotube hybrid system

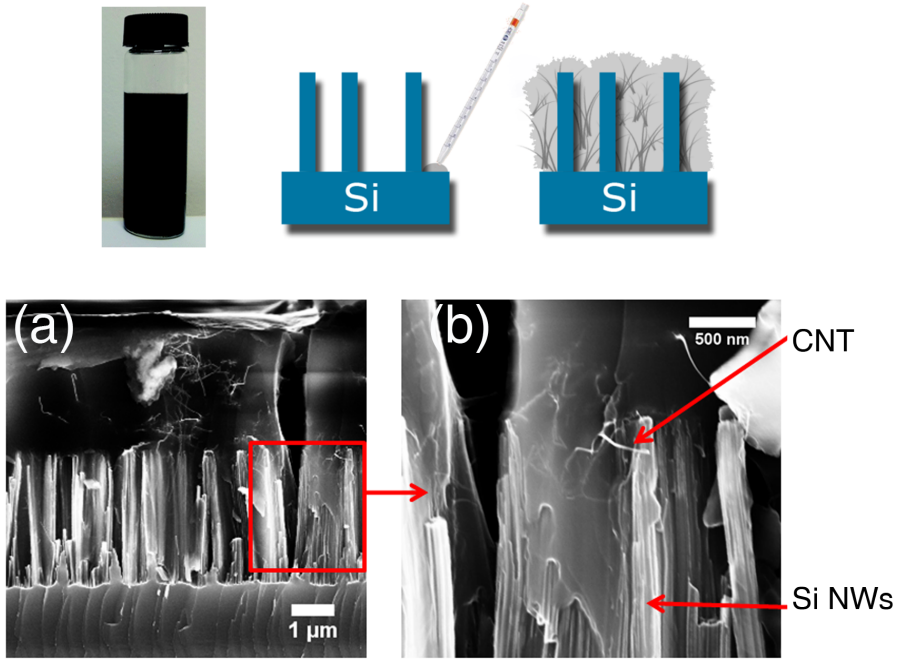


*Figure 2.15: Representative scheme illustrating the NW/CNT sample preparation obtained from a 3 µm long, 7 nm diameter NW array embedded in a 0.5 mg/l CNT dispersion. The SEM cross-section of a typical CNT/NW sample is reported in (a) where CNTs are observable as white filament structures decorating the NWs. A high resolution SEM detail is displayed in (b) [111].*

The following section discusses the realization of the hybrid NW/CNT system. The hybrid system has been prepared with a Si NW array of 7 nm of diameter characterized by high superficial density of $10^{12} NWs \cdot cm^{-2}$ [88, 111]. The adopted infiltration process is depicted in the representative scheme of fig. 2.15 top section. A 5 $\mu l$ volume of 0.5 mg/l CNT dispersion was drop-casted onto 3 $\mu m$ long Si NW array with dimensions of the samples of 0.5 x 1 $cm^2$. The dispersion spontaneously diffuses until a uniform coverage of the array is achieved. CNTs result stably embedded in the NW array after a few hours of air exposure at room temperature. The SEM cross-section of the newly formed solid hybrid system is displayed in fig. 2.15(a-b), where tubular structures wrapping nanowires are discernible. The presence of CNT embedded in the NW forest is clearly distinguishable in the high resolution SEM detail reported in fig. 2.15(b). The CNTs used for the dispersion have diameter smaller than 1 nm and such small nanostructures are not detectable by SEM microscopy. Thus the filaments noticeable in the SEM image demonstrates that the detectable CNT fraction mainly consists of small bundles having size of only few tens of nm. The Raman spectrum of the Si NW/CNT hybrid system acquired by exciting the system with the 633 nm wavelength at pump power of 80 $\mu W$ is reported in fig. 2.16(a-b). By Raman spectroscopy it is possible to observe the effective embedding of the 0.5 mg/l CNT dispersion into the $3\mu m$ long Si NW array. The typical Si and SWCNT vibrational modes are displayed in fig. 2.16(a). The low frequency region is marked with a red rectangle and zoomed in fig. 2.16(b). The three intense peaks centered at 253, 266 and 284 $cm^{-1}$ are assigned to the radial breathing mode (RBM) of the (9,4), (7, 6) and (7, 5) CNT chiral families. The RBM are produced by the out-of-plane coherent oscillation of C-atoms along the radial direction of the tube. These are typical CNT phonon modes whose frequencies are inversely proportional to the nanotube radius and are therefore related to the CNT chiral vector [112]. The presence of Si NWs and CNTs can be identified and discriminated from the Raman spectrum of the hybrid system. Indeed Si optical first-order Raman peak (520 $cm^{-1}$) and second-order transversal optical phonons signals (900-1100 $cm^{-1}$) are observed in fig. 2.16(a), while CNT Raman emissions can be divided in several contributions, mainly D, G and M-band, followed by iTOLA and G'-band.

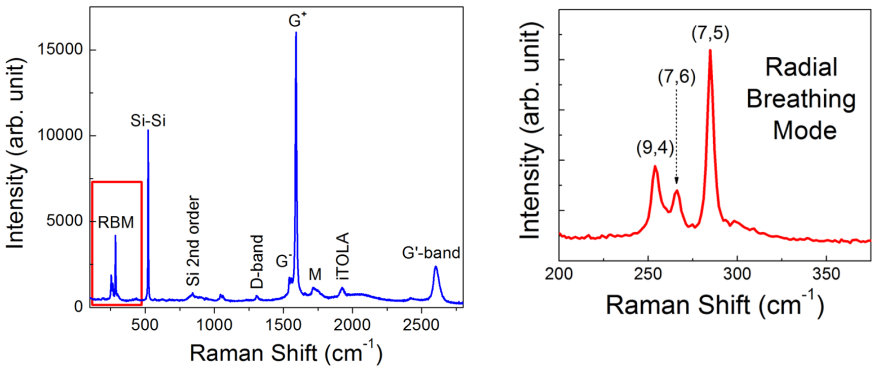


*Figure 2.16: (a) Raman spectrum of a Si NW/CNT sample acquired by exciting the system with 633 nm line of an He-Ne laser at a pump power of 80 $\mu W$. (b) The 200-350 nm range of the Raman spectra is zoomed to show the occurrence of typical RBM oscillations [111].*

The G-band is divided in two features: $G^-$ that is peaked at about 1560 $cm^{-1}$ and a sharp component named $G^+$ peaked at 1590 $cm^{-1}$. The first feature is due to in plane stretching vibrations of C atoms along the circumferential direction. While $G^+$ is produced from in-plane vibrations along the axis of the tube.
Generally the G-band becomes smaller for small tube diameters and it is strong and asymmetric for metallic tubes assuming a Breit-Wigner-Fano shape. Both $G^-$ and $G^+$-bands exhibit Lorentzian shape peaks, attesting that the dispersed CNT are mainly semiconducting. The D-band observed at 1307 $cm^{-1}$ is a second order Raman scattering mode related to the disorder grade of the CNTs. Its overtone is indicated as G'-band and peaked at 2604 $cm^{-1}$. Both D and G'-bands have negligible intensities compared to the G-band. It proves that the presence of tube defects or amorphous C-contaminants present in the hybrid system are almost insignificant. M-band (an overtone mode at 1730 $cm^{-1}$) and iTOLA band (a combination of optical and acoustic modes at 1927 $cm^{-1}$) are also visible. These two features are typical vibrations associated to the presence of semiconducting CNT [99, 112].

## 2.5 Room temperature multiwavelength light sources based on silicon nanowire and carbon nanotube hybrid system

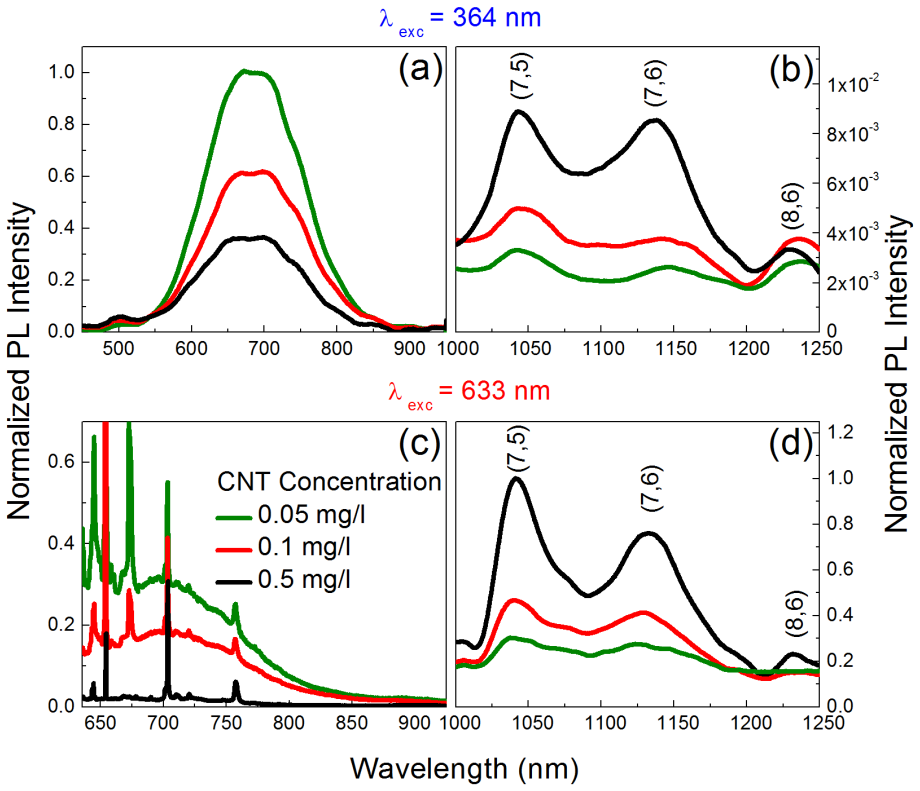


*Figure 2.17: Room temperature PL spectra of Si NW/CNT samples realized with CNT concentrations of 0.5 mg/l (black line), 0.1 mg/l (red line), 0.05 mg/l (green line). Si NWs and CNT emission spectra obtained by exciting the system at the 364 nm wavelength are displayed in (a) and (b) respectively. While (c) and (d) display the emission spectra of Si NWs and CNTs acquired at the 633 nm excitation wavelength [111].*

Several NW/CNT samples containing different amount of tubes were prepared by diluting the CNT dispersion. The main CNT concentrations reported in this study are 0.5 mg/l, 0.1 mg/l, 0.05 mg/l, respectively displayed as black, red and green lines in fig. 2.17. Fig. 2.17 displays the normalized PL spectra of Si NWs infiltrated with CNT dispersion investigated as a function of the CNT concentrations mentioned above. The spectra presented in fig.2.17(a) and (b) have been obtained by exciting the system with the 364 nm line of an $Ar^+$ laser. Figures 2.17(c) and (d) have been acquired using the 633 nm excitation wavelength from a He-Ne laser. All spectra have been normalized as a function of the power and the intensities have been scaled for detection conditions in order to be comparable.
A room temperature multiwavelength emission is exhibited from the NW/CNT hybrid system. Indeed a broad visible emission is produced by quantum confined Si NWs, while the IR emission is coming from the CNTs. Data reported in fig. 2.17(a-d) also demonstrate tunability of PL relative intensity for both ranges by simply varying the CNT concentration or the excitation wavelength. For example, fig. 2.17(a-b) report the PL visible and IR spectra when exciting the system with UV radiation at 364 nm. Si NWs visible emission is centered at about 700 nm and is about two orders of magnitude higher than the infrared one for all CNT concentrations. Figure 2.17(b) reports CNT IR emission as obtained in the same conditions. The IR emission is characterized by the presence of three major peaks at 1042, 1132 and 1237 nm. By comparing fig. 2.12-2.14 and fig. 2.17, the first feature at 1042 nm can be assigned to the convolution of (7, 5) and (10, 2) emission. While the second component is given by the superposition of (9, 4), (8, 4) and (7, 6) chiralities. A weaker broad peak is observed at longer wavelength, mainly assigned to the (8, 6) and (9, 5) families. It is noteworthy that the hybrid system exhibits the same PL peaks with similar relative intensities as previously reported for the CNT dispersion for the same excitation wavelength in fig. 2.13. NW emission is reduced when increasing the CNT concentration. The opposite behavior is observed for IR emission, that increases when incrementing CNT concentration. The visible emission from Si NWs at 633 nm reported in fig. 2.17(c) is way less intense with respect to the emission in fig. 2.17(a). In fact for isolated Si NWs a PL intensity excited at 364 nm is 4 times higher

than what measured by exciting at 633 nm for the same power condition. Si NWs and CNT typical Raman peaks are superimposed to the broad band emission from NWs, as displayed in fig. 2.17(c) when exciting the system at 633 nm. In fact Si overtone scattering from acoustic mode (at 645 nm), first and second order Si phononic transitions (at 654 and 672 nm) are detected. Furthermore CNT Raman G-band and G'-band are appreciable at 703 and 757 nm respectively. As previously discussed, fig. 2.17(c) demonstrates that by increasing the CNT concentration the intensity of the NW visible PL signal strongly decreases. Also in this case, the CNT emission increment as a function of CNT concentration. Si NWs PL emission results almost undetectable and the spectra are mainly dominated by CNT Raman peaks for the highest CNT concentration of 0.5 mg/l (black line) . When exciting at 633 nm, IR emission from CNT results predominant over the visible one. This is due to the direct excitation to $eh_{22}$ or $eh_{11}$ levels when using resonant radiation to pump the system. The relative emission intensity of (7,5) and (7,6) chiralities is slightly different according to what previously explained in section 2.3.
Moreover, no significant variations of the NW and CNT PL peak position and shape are detected when changing either the excitation wavelength or CNT concentration.
Figure 2.18 plots the normalized integrated PL intensities recorded in the visible ($I_{vis}$) and in the IR region ($I_{IR}$) as a function of the CNT concentration for 633 nm (fig. 2.18(a)) and 364 nm (fig. 2.18(b)) excitation wavelengths. All spectra have been normalized as a function of the detection conditions and the intensities have been scaled to be comparable. Fig. 2.18(a-b) shows that the visible PL integrated peaks $I_{vis}$ decrease as a function of CNT concentration for both excitation wavelengths. The opposite behavior is reported for $I_{IR}$ peaks that increase by increasing CNT concentration. The ratio $I_{IR}/I_{vis}$ as a function of the CNT concentration at 633 nm excitation wavelength is reported in the inset of fig. 2.18(b). A clear incremental trend is attested when increasing the CNT concentration.

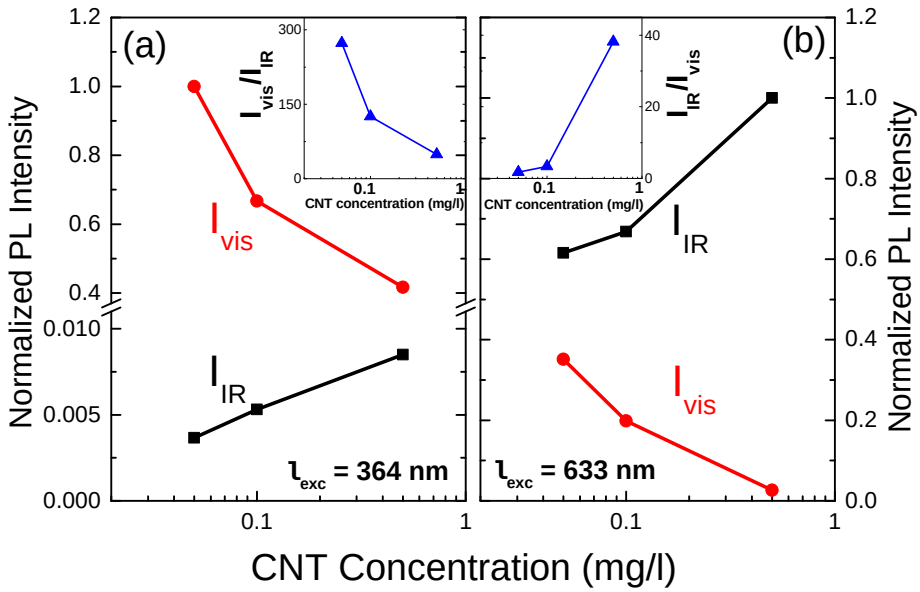


*Figure 2.18: Normalized integrated PL intensities recorded in the visible ($I_{vis}$) and in the IR ($I_{IR}$) regions as a function of the CNT concentration for excitation wavelengths of (a) 364 nm and (b) 633 nm. The two insets report the ratio $I_{vis}/I_{IR}$ for figure 2.18(a) and $I_{IR}/I_{vis}$ for figure 2.18(b) as a function of the CNT concentration for the two excitation wavelengths [111].*

The IR emission can be 40 times higher than the visible emission when using the maximum CNT concentration of 0.5 mg/l. The predominance of the IR signal is partly due to the resonant absorption in the visible range from (7, 5) and (7, 6) families. In fact Si NW absorption in this range is far more inefficient. Nevertheless the occurrence of energy transfer mechanisms from NWs to CNTs further quenching NW PL emission cannot be excluded a priori. On the contrary, when using the 364 nm excitation wavelength the opposite trend is reported for $I_{vis}$ and $I_{IR}$ as a function of CNT concentration. In this case Si NWs emission results predominant over the IR one since silicon absorption in the UV range is highly efficient [113]. Meanwhile the CNT absorption in the UV range involves a non-radiative decay process from $eh_{33}$ to $eh_{22}$ or $eh_{11}$, resulting in a less efficient process.

Therefore as reported in the inset of fig. 2.18(a), the $I_{vis}/I_{IR}$ ratio is increasing as a function of the CNT concentration for the 364 nm excitation wavelength. The $I_{vis}$ emission can be about 280 times higher than the IR emission for the lowest CNT concentration of 0.05 mg/l. Figure 2.18(a-b) are particularly remarkable. Demonstrating that PL visible and IR relative intensities can be tuned over a wide range by varying two simple parameters, such as CNT concentration or the excitation wavelengths.

## 2.6 Conclusion

In this chapter the realization of a high density array of vertically aligned Si NWs has been demonstrated by using a low-cost and controllable metal assisted chemical etching technique. By tuning the deposition of thin metallic layers at the percolation limit it is possible to control the diameter on a compatible scale for the occurrence of quantum confinement phenomena. The advantages of this method have been compared to the most used VLS technique, demonstrating the remarkable control over Si NW structural features as length, doping and crystalline quality.
The optical properties of the Si NWs template have also been studied, reporting a bright and efficient room temperature PL due to quantum confinement effect, with the PL emission shifting as a function of the NW radii and PL intensity depending on the NW length. Furthermore, the structural and optical properties of a semiconducting SWCNT dispersion have been studied from absorption, PL and PLE analysis. Leading to the identification of a low-cost procedure for the effective and stable embedding of several semiconducting SWCNTs families in a Si NW array. The structural and optical properties of the hybrid system have been carefully studied by SEM, Raman and PL analysis. Finally, the room temperature Si NW/CNT emission both in the visible and infrared range have been investigated. Demonstrating that relative emission intensities can be tuned as a function of the CNT concentration or the excitation wavelength. The achieved results are extremely promising for the realization of an efficient multi-wavelength Si-based light source operating at room temperature and fully implementable with current Si technology.
These systems also enable the modulation of the relative emission peaks as a function of the CNT concentration and of the excitation wavelengths. Furthermore, it is also possible to vary the IR emission wavelength by changing the CNT chiral families present in the dispersion, demonstrating their strategic use for telecommunication sector.

# Chapter 3

# Two-dimensional silicon nanowire random fractal arrays


**Abstract**

*Achieving light management in nanostructured materials represents a recent challenge for several research groups. The capability to control the absorption, emission and light transport properties in a medium is an appealing task generally attained by using periodic or random surface patterning at the expense of an advanced technology.*
*This chapter is focused on the design of two-dimensional random fractal arrays of Si nanowires by metal assisted chemical etching. Using thin gold layers at percolation limit having fractal arrangement as precursors for the synthesis process, it is possible to obtain the complementary fractal disposition for Si NWs with a well controlled, maskless and low cost method.*

*A fractal is realized by the recursive repetition of a structure along the space with scale invariance and self-similarities. In particular, silicon nanowires fractal arrays display strong self-similarities over a wide range of length scales, from 20 nm up to a few microns.*
*The design of different fractal architectures and the investigation of the key role structural parameters in terms of fractal dimension and lacunarity are here reported. Moreover, the correlation among the structural properties and the optical response of the array has been demonstrated. A strong light trapping behavior in the visible range due to the efficient in-plane multiple scattering occurring in the Si NW layer has been reported, attesting a promising potential for both photovoltaic and photonic applications.*

## 3.1 Preparation of two-dimensional silicon nanowire random fractal arrays

*Figure 3.1: Photograph depicting a Romanesco broccoli as a typical example of natural fractals in ordinary life.*

A fractal is characterized by the recursive repetition of a pattern along the space with scale invariance and self-similarity [114]. Fractal structures are largely present in nature and in our ordinary life [115], one just needs to look carefully.
As an example, in fig. 3.1 a *Romanesco broccoli* vegetable is reported. Its spatial configuration attests how nature is spontaneously organized in fractal structures. Similar behaviors are reported in the biology realm where many examples of fractal or multifractal structures are present [116]. Fractals have been intensively studied by mathematicians since the 17th century, but their theory was only recently formalized in the latest 20th century [117]. A new emerging physics branch has deeply investigated the fractal arrangement of thin percolative gold layers. Indeed, Au fractal films present a variety of phenomena, such as superconductivity, superdiffusivity and nonlinear optics effects that can be used for a large range of applications.

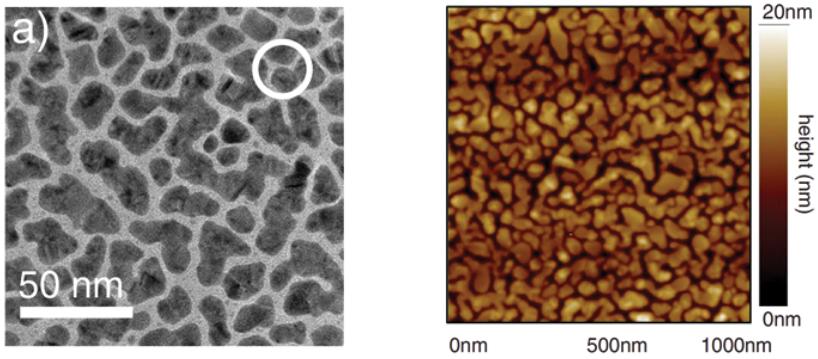


(a) (b)

*Figure 3.2: (a) TEM image of a percolative gold layer deposited on silica glass by EBE and having Au surface coverage of 67% [118].*
*(b) AFM map of a discontinuous gold film deposited by thermal evaporation on quartz substrate, having Au surface coverage of 59% [119].*

Percolation theory has been first introduced by Broadbent and Hammersley in 1957. According to their theory, a thin metallic layer is "*at percolation*" when connected regions of infinite extent appear (or disappear) for which it is always possible to identify a path connecting the edges of the considered area [120, 121]. A metallic film at percolation limit presents a two-dimensional (2D) random fractal arrangement [78]. The percolation threshold corresponds to the concentration of deposited material where a connected network is formed. In the case of Au deposition the percolation threshold is defined as a function of the filling factor and is generally between 50% and 60% according to the deposition and substrate conditions.
Figure 3.2(a) displays the TEM microscopy of a gold percolative film deposited by EBE on glass, having a filling factor of about 67%. Carminati group demonstrated the fractal arrangement of such Au percolative films by observing non-linear optical transitions [118]. Another example is repoerted in fig. 3.2(b) showing an atomic force microscopy of a discontinuous gold film at percolation limit having a filling factor of 59%, deposited by Au thermal evaporation on quartz in ultra high vacuum condition from Laverdant group [119]. Non-linear optics effects generally occur above the percolation threshold, together with a strong electrical conductance and super-diffusion.

These are some typical phenomena usually manifested in fractal systems. For this reason, the percolation threshold is directly linked to a fractal distribution of the system for which unexpected physical effects are observed [114, 122].

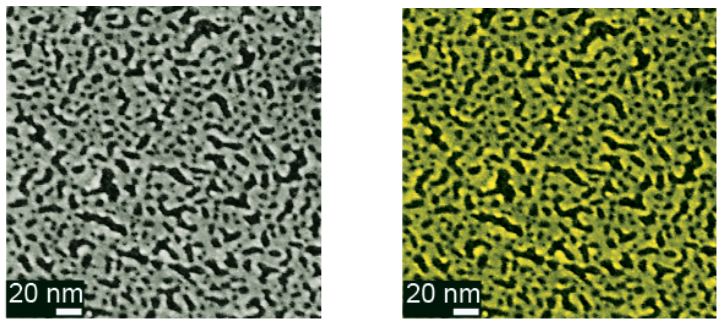


(a) (b)

*Figure 3.3: (a) Plan-view SEM microscopies of a 2 nm percolative Au layer deposited on (111)-oriented Si substrate by EBE. (b) Corresponding false-color SEM image used for Au filling factor measurement.*

In order to fabricate a two-dimensional fractal nanowire array we first prepared a percolative Au film to be used as a precursor.
Figure 3.3(a) displays the plan-view SEM microscopy of a 2 nm percolative Au film deposited on a n-doped ($10^{15} at/cm^3$), (111)-oriented Si substrate by electron beam evaporation. The connected structure typical of percolative films is clearly visible from the image. In order to measure the Au surface coverage the following procedure has been adopted. The contrast of the high resolution SEM image of 2 nm of Au deposited on the Si substrate ( fig. 3.3(a)) has been modified by using Gatan Digital Micrograph Suite. The gold covered regions have been highlighted in yellow, as shown in fig.3.3(b), and the total area of the selected regions has been measured by pixel counting. The filling factor has been estimated as the ratio of the Au covered area for the total area of the analyzed image expressed in the same units. Using this procedure an Au filling factor of about 54% has been measured. The estimated value is above the Au percolation threshold on silicon guaranteeing the realization of a fractal structure. It is worth noticing that the percolation limit is sensitive to different factors and strongly influenced by the growing conditions.

Indeed, a major key role is determined by the substrate that is responsible for the kinetic and thermodinamic arrangements of the metal clusters on the free surface [123]. As far as Au percolative films deposited on Si are concenerd, the percolation threshold generally corresponds to an Au filling factor value above 50% [122, 124].
After the realization of a controlled Au percolative film, fractal Si NWs have been prepared by metal assisted chemical etching using this Au fractal film as precursor for the process. Further details of this technique are reported in section 2.1.

## 3.2 Fractal characterization

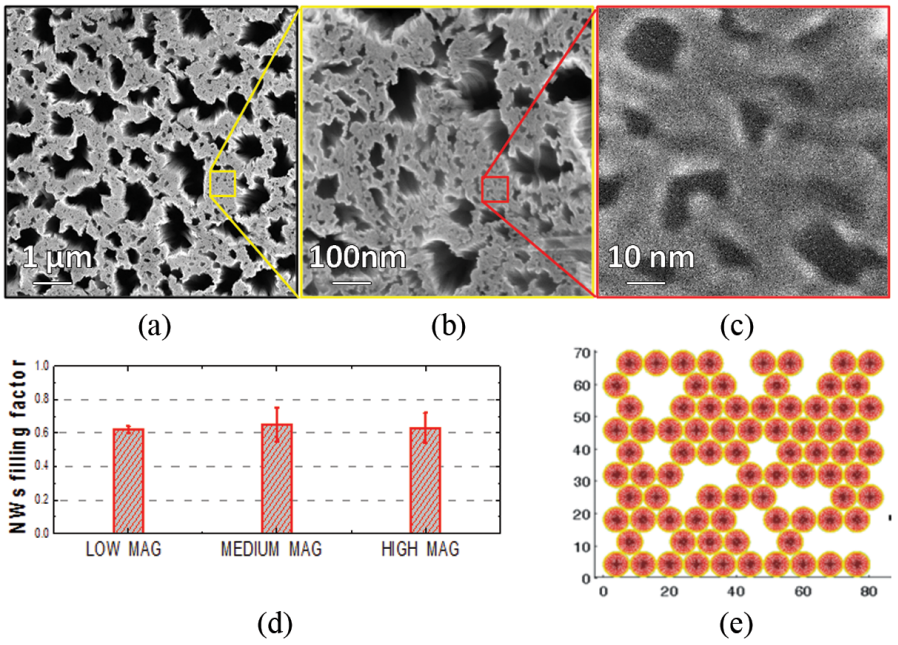


*Figure 3.4: Plan-view SEM images of a Si NW array obtained by metal assisted chemical etching acquired at (a) 25kx, (b) 250kx and (c) 2500kx magnification scale respectively. (d) Si NW surface coverage histogram for all the investigated magnification scales. (e) Representative scheme of the elementary map used for the model building cell (MBC) approximation.*

The structural properties of Si NWs have been studied after their realization by chemical etching assisted by the presence of Au fractal layers. The self-similarity of a (111)-oriented, 2.6 $\mu m$ long Si NW array has been tested at different length scales by SEM analysis, as reported in fig. 3.4(a-c). The SEM microscopies have been acquired at the same point of the sample for different magnification conditions of (a) 25kx, (b) 250kx and (c) 2500kx respectively. A Si NW surface coverage of about 60% is measured for all the analyzed magnifications as displayed by the histogram plot in fig. 3.4(d), confirming the scale invariance of the system. It is very impressive to observe that by varying the magnification of observation, the repetition of the random structure is always the same. These self-similarity and scale invariance features are clear evidence of Si NWs fractal arrangement. Therefore, the realization of Si NWs having fractal geometry has been demonstrated by using Au fractal film as precursor for the etching. Indeed, the Au fractal arrangement is the negative mask used for Si NWs synthesis. Hence, the fractal geometry is transferred to the NWs array during the etching, whose planar arrangement results complimentary to Au ones. The randomness of the array has been described using the model building cell (MBC), a bottom-up approach for fractal characterization [125]. According to the MBC approximation a 2D elementary cell of area 80x70 $nm^2$ has been created from the random disposition of $N = 80$ circular monomers having 4 nm radius. The radius choice is based on the Raman and TEM measurements for Si NW diameters, corresponding to $7 \pm 2$ nm for a 2 nm-thick Au precursor layer. Figure 3.4(e) displays a MBC elementary cell having filling factor of 60% in order to reproduce the high resolution SEM image reported in fig. 3.4(c). The MBC cell has been repeated along the space to map an area of 800x700 and 8000x7000 $nm^2$, corresponding to the SEM images of fig. 3.4(b) and (a) respectively.
The *fractal dimension* ($D_F$) is a non-integer value measuring how the pattern repetition changes as a function of the investigated length scale [114]. As far as 2D fractals are concerned, $D_F$ never reaches the Euclidean value of 2. A $D_F \sim 1.9$ very close to the asymptotic value has been calculated by using the MBC approach, which is a typical characteristic of high density fractals [122].

The fractal dimension has been calculated from the MBC model as a function of the monomer number N according to the following relation:

$$N \sim {r_g}^{D_F} \tag{3.1}$$

where $r_g$ is the gyration radius defined as:

$${r_g}^2 = \frac{1}{2N^2}\sum_{ij}^{N}(r_i - r_j)^2 \tag{3.2}$$

being $r_i$ and $r_j$ the position vector of the $i_{th}$ and $j_{th}$ monomer [125]-[126]. A gyration radius of $r_{g0} = 30.6$ nm has been measured for the MBC cell displayed in fig. 3.4(e) [127].
The fractal dimension has been obtained as the slope of the $logN_k$ vs $log(\frac{r_{gk}}{r_{g0}})$ plot, where $N_k$ is the number of monomers needed to cover the different magnification SEM images, while $r_{gk}$ are the corresponding gyration radii. A fractal dimension of about $D_F \simeq 1.9$ has been measured, resulting in perfect agreement with the value reported for an Au fractal layer.
$D_F$ values very close to the eucledian asymptotic one are characteristic of high density fractals [122].

### 3.2.1 Realization of Si NW fractal arrays with different structural characteristics

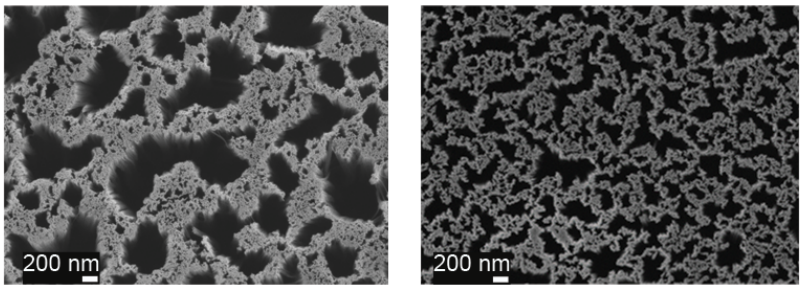


(a) (b)

*Figure 3.5: SEM characterization of two different Si NW fractal arrangements achieved by MACE (a) on (111) and (b) (100)-oriented Si substrates, hereafter referred to as sample 1 and sample 2, respectively.*

A critical aspect for applications is the realization of Si NWs with different structural features.
The SEM plan-view images displayed in fig 3.5(a-b) show the realization of two different fractal arrangements obtained by varying the NW growth conditions. Figure 3.5 (a) presents a Si NW fractal array realized by MACE using 2 nm of Au on (111) Si wafer. By contrast fig. 3.5 (b) shows a more compact and highly packed fractal architecture obtained under the same condition by using a (100)-oriented Si wafer. (111) and (100) Si NW fractal arrays will be hereafter referred to as **sample 1** and **sample 2** respectively.

The design of different fractal arrangements has been optimized by either varying the crystalline orientation of the substrate, or by changing the filling factor of the Au film used for the etching.
When the Si crystalline orientation is changed, the electron density distribution and the superficial density of states are different. In this way the wettability, diffusion and clustering dynamics of gold atoms distributed on Si surface are modified [78, 123].
Finally, the Si NW fractal morphology can be easily tuned controlling the Au deposited film as it corresponds to NW negative print. Moreover, a fine control over the spatial arrangement of MACE synthesized Si NWs is attained by an industrially compatible approach, achieving the structural tuning without the use of any expensive techniques.

The *lacunarity* ($\lambda$) is the most important parameter used to unequivocally describe a fractal structure. In order to measure the lacunarity of the system we referred to the Mandelbrot studies (1983), considered as one the fathers of the fractal analysis. His theory on fractal arrangement was later developed in 1991 by Allain and Cloitre, who clarified the parameters dependency in the **box counting algorithm** (BCA). Their algorithm is today well acknowledged by the scientific community and well documented in several papers on fractals characterization. As displayed by the inset in fig. 3.6(a) and according to the Allain-Cloitre algorithm, a grid has been superimposed on the SEM image by using ImageJ software and Fraclac plugins [128]. For fractal dimension calculation the number of boxes $N$ covering the area has been counted as a function of the box size $\epsilon$ in order to estimate the fractal dimension according to the following equation:

$$N = A\epsilon^{-D_F} \tag{3.3}$$

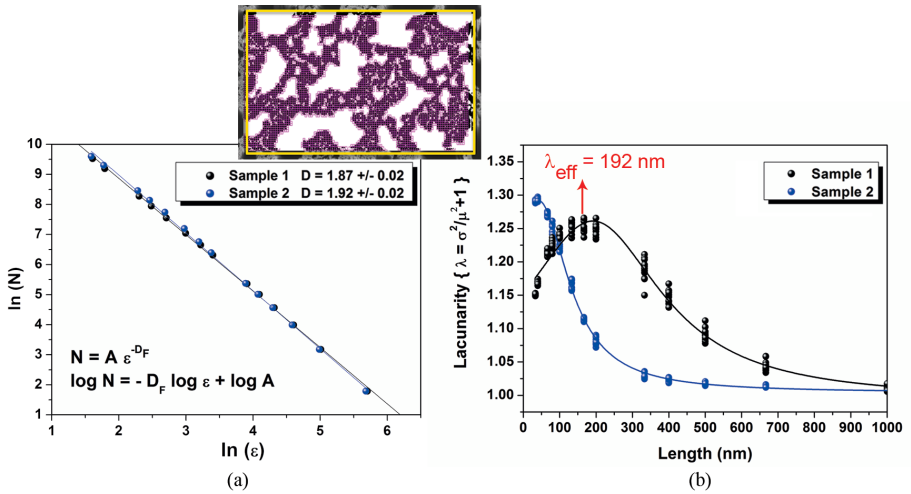


*Figure 3.6: Fractal parameters characterization for the NW samples displayed in fig. 3.5. (a) The fractal dimension is plotted in log-log graph as a function of the box size. The inset illustrates the box-counting algorithm grid adopted for the fractal parameters evaluation.*
*(b) Lacunarity for the two NW samples reported as a function of the investigated length scale.*

The process has been iterated 14 times to obtain convergence and taking into account the resolution of the image.
The box number is plotted as a function of the box size in a log-log graph presented in fig. 3.6(a). The trend has been fitted with a linear function whose slope corresponds to the fractal dimension of the system $D_F$.

$$logN = -D_F log\epsilon + logA \tag{3.4}$$

Fractal dimensions equal to $D_{F1} = 1.87 \pm 0.02$ and $D_{F2} = 1.92 \pm 0.02$ have been measured respectively for sample 1 and sample 2. These results are in perfect agreement with the one obtained by MBC model, further confirming the two-dimensionality of the Si NW fractal structure. The $D_F$ defines the scaling law for the fractal structure and therefore it is connected only to the geometrical properties of the system.
Nevertheless the fractal dimension itself is not enough to unequivocally describe the system. In fact, it is possible to find fractals with the same scaling relation having different spatial arrangements.

In order to fully characterize a fractal, a new parameter must be defined: the *lacunarity* ($\lambda$). Lacunarity is a crucial fractal feature taking into account the scale invariance, filling factor and geometry of the system [129]. It is strongly related to alternation of empty and filled space, namely the heterogeneity spatial distribution. In 1983 Mandelbrot defined the lacunarity as the "distribution of gap sizes as a function of the length scale", therefore an object is considered more lacunar when the gap sizes are distributed over a wide range of lengths. Both $D_F$ and $\lambda$ measure the structural complexity of the system, but the lacunarity is the only quantity unequivocally describing heterogeneity distribution of the system as a function of the length scale. The lacunarity is defined as the ratio between the pixel density variance ($\sigma^2$) over the pixel density square ($\mu^2$) as a function of the boxes size and position [128, 129].

$$\lambda = \sigma^2/\mu^2 + 1 \tag{3.5}$$

The pixel density distribution and pixel variance have been calculated with the same box-counting approach, sectioning the image in boxes of decreasing size and position. Figure 3.6(b) reports the lacunarity trend as a function of the length scale for 2.5 $\mu m$ long NWs realized on (111) and (100) Si substrate, respectively sample 1 and 2, whose planar distributions are reported in fig. 3.5(a-b).
Both samples have lacunarity values higher than one over a wide length range, attesting the presence of heterogeneity overall the investigated scales. Particularly interesting is the behavior of sample 1 whose lacunarity shows an heterogeneity peak at about 192 nm. A maximum of the refractive index fluctuation is expected at this length, increasing NW scattering efficiency. As it usually occurs, the fractal geometry strongly affects the optical response of the system. Meanwhile, lacunarity for sample 2 increases towards smaller length scale without showing any appreciable peak. Nevertheless, the presence of a blue-shifted peak cannot be excluded a priori, since the box counting analysis has been halted at 33 nm according to the resolution of the SEM image. Finally, the realization of 2-dimensional Si NW fractal arrays has been demonstrated by using a low-cost, industrially compatible method without the use of lithography or masks. Furthermore, it is possible to vary the fractal geometry of the array by optimizing the chemical etching.

## 3.3 Optical properties

In order to improve the optical properties of a system there are many surface patterning strategies that can be adopted [130]. Indeed the angle of incidence of light is scrambled by simply using surface texturing, increasing the light path inside the medium [131, 132]. This strategy leads to an overall absorption and light-matter interactions improvement [133].
The fabrication of either random or periodic texture often requires the use of advanced and expensive technologies. Furthermore, a good reproducibility over the structural arrangement can hardly be obtained for random patterning. The realization of a fractal is not only interesting for mathematical studies. In fact, such a structure can improve the optical properties of the system if compared to random and periodic surface patterns. In an infinite fractal the presence of cavities of dimension ranging over all the possible length scales are present. Such cavities can efficiently match the incoming wavelengths with comparable dimensions, inducing important resonant optical phenomena [134]. For this reason, fractal-like structures are nowadays implemented in many smartphone antennas in order to capture several signals, whose wavelengths span on a wide range of orders of magnitude [135].
As far as a finite fractal is concerned, its cavity dimensions range over a broad region of finite length scales. We demonstrate that the fractal geometry of Si NW arrays guarantees improved optical properties which is extremely promising for applications.

### 3.3.1 Light trapping properties

Si NW arrays are arranged in random and complex 2D fractal structures leading to significant refractive index fluctuations along the NW plane. These fluctuations induce a strong in-plane multiple scattering, resulting in a remarkable suppression of NW reflectance. Light scattering properties of Si NW fractal arrays have been tested by measuring the total reflectance from the ultra-violet-visible to the near-infrared spectral range.

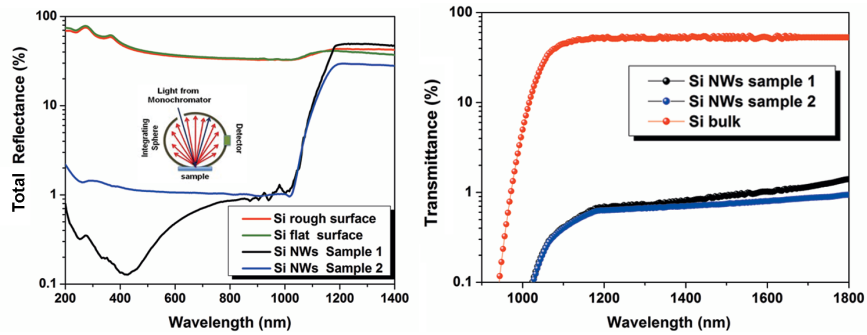


(a) (b)

*Figure 3.7: Light scattering properties of Si NW random fractal arrays. (a) Total reflectance of Si NW sample 1 (black lines) and sample 2 (blue line) compared to a polished Si surface (green line) and a diffusive rough back-layer (in red). (b) Si NW direct transmittance for samples 1 (black dots) and sample 2 (blue dots) are compared to a double polished c-Si bulk (red dots) taken as a reference.*

A comparison among the total reflectance of rough Si (red line), flat Si (green line), Si NW sample 1 (black line) and sample 2 (blue line) is reported in fig. 3.7(a). The total reflectance has been measured using a double-beam spectrophotometer equipped with an integrating sphere. In this configuration both specular and diffuse reflected light components are acquired.
Few microns rough Si surface presents a single-scattering behavior due to the average angle-dependent Fresnel coefficients at the Si-air interface. The same trend is also observed for a polished flat Si surface. Meanwhile Si NW arrays reflectance present a sharp drop-off below the Si bandgap corresponding to 1.1 $\mu m$. A total reflectance lower than 1% has been measured for both NW samples across the entire visible-NIR range. The extremely low reflectance values are a clear evidence of light trapping inside the Si NW layer, arising from multiple scattering occurring within the NW layer. Indeed, it is worth noticing that isolated quantum confined NWs having 7 nm diameter could hardly lead to such an efficient multiple scattering [62]. It is the alternation of tightly spaced NW regions separated by air cavities (as shown in fig. 3.6) that introduces strong heterogeneities producing light pathways ranging on length scales between 10 nm and 1000 nm.

Therefore, it is the heterogeneity distribution that is responsible for the efficient in-plane multiple scattering. The total reflectance of sample 1 presents a broad minimum peak centered at about 428 nm and approaching 0.1% value.
The effective refractive index $n_{eff} = 2.23$ has been calculated by the Bruggeman mixing rule, assuming a composition of 40% air voids, 40% silicon and 20% silicon native oxide [136, 137]. It is very impressive to observe that sample 1 reflectance minimum at about 428 nm corresponds to an effective wavelength traveling in the Si NW layer of $\lambda_{eff} = \frac{\lambda}{n_{eff}} = 192$ nm.

Fractal Si NWs optical properties are strongly related to their structural arrangement as clearly demonstrated from the lacunarity measurements for both samples. In fact, sample 1 presents a lacunarity maximum at about 192 nm. We observed that at the wavelength of 192 nm the reflectance is lower than 0.1% attesting a light over-trapping feature. This correspondence between the length scale at which the lacunarity has its maximum and the wavelength for which the sample shows the minimum of reflectance is a very strong demonstration that the optical properties depend on the lacunarity. By contrast lacunarity for sample 2 increases towards smaller length scales. Indeed, the reflectance does not show any light over-trapping in this range in agreement with the lacunarity trend. This correspondence highlights the strong influence of the morphological properties, such as lacunarity, on the optical scattering response of these materials. Therefore, by varying the fractal lacunarity it is possible to control and tune the optical properties of Si NW arrays. That is a very appealing result for photovoltaic applications.

Si NWs obtained by MACE have an almost perfect vertical alignment, leading to a constant average refractive index along the vertical direction. A material that arose a strong interest among the photovoltaic research is the black silicon [138]. Black silicon is a new emerging material well known for its low reflectivity due to anti-reflection effect induced by a z-graded refractive index profile. Our fractal NWs are a particular black-Si substrate do not possess anti-reflection phenomena but are instead characterized by a very strong light trapping. In fact, for vertically aligned Si NWs the presence of an anti-reflection behavior observed for black silicon materials can be excluded because of the lack of a z-graded index profile.

This thesis is also supported by the total reflectance trend observed in the Si transparency region. As shown in fig. 3.7(a) NW reflectivity is pretty high for wavelength above the Si bandgap and sharply drops-off below 1.1 $\mu m$ in correspondence to the Si absorbing visible range. This trend is incompatible with an antireflection effect due to a z-graded index profile that would lead to a smooth and very low reflectivity across the Si bandgap. Indeed, since the lacunarity is higher than one for length scale up to 1100 nm, a strong light trapping is observed until this value. This is an unexpected result for Si that is generally not absorbing in this NIR wavelength region. Further demonstrating how lacunarity determines the optical response of the material, can be varied by the structural properties.
In order to confirm the presence of multiple scattering occurring along the Si NW plane and for further exclusion of an anti-reflection effect Si NWs direct transmittance are reported in fig. 3.7 (b). The measurements have been performed on a spectrophotometer in the direct transmission configuration, excluding the diffused light components. Transmittance measurements are only shown in the near-infrared since its values drop to zero in the visible range due to Si absorption and reflection. To avoid any interference and IR signal coming from the rough Si surface the measurements have been performed on NWs realized on a double polished Si wafer and compared with the same substrate. Figure 3.7(b) displays an impressive transmittance suppression below 1% for both Si NW samples with respect to Si reference. Meanwhile for anti-reflection materials a transmittance increment above the Si bandgap is observed since both reflection and absorption are nearly zero in the IR range. The Si NWs transmittance below 1% in the Si non-absorbing region is another clear demonstration of the very strong light trapping.
Therefore, it can be concluded that light is neither reflected nor scattered out from the NW arrays but it remains mostly trapped in the NW layer by multiple scattering processes, as attested by fig. 3.7(b). The great potential of 2D Si NWs random fractal array for photovoltaics has been also confirmed by angular reflectance measurements. The specular reflectance for sample 1 is reported as a function of the incidence angle in fig. 3.8. Si NWs have been excited with non-polarized light by using 428 nm (blue dots), 532 nm (green dots) and 633 nm (red dots) excitation wavelengths, respectively.

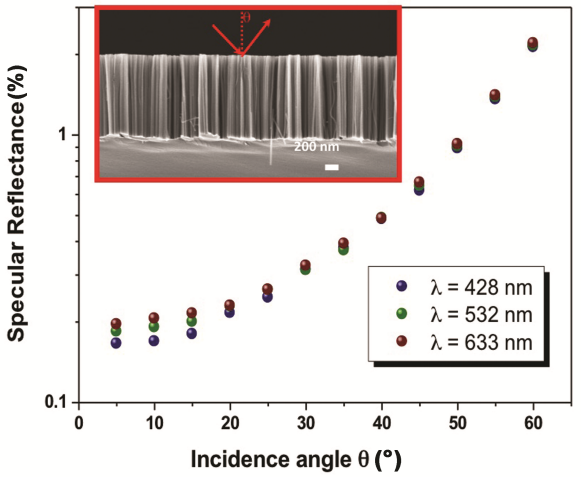


*Figure 3.8: Specular reflectance as a function of the incident angle of light reported for fractal Si NW sample 1. Measurements have been acquired at the excitation wavelength of 428 nm (blue dots), 532 nm (green dots) and 633 nm (red dots). The inset displays a SEM cross-section of Si NWs and the red arrows illustrate the incident and scattered light forming a $\theta$ angle with the normal axis.*

The measurements have been acquired in the spectral range between 300 nm an 800 nm by using a home-made micro-reflectometer coupled to a Fourier-transform spectrometer (Bruker IFS 66s). The inset displays a schematic representative of the experimental illumination conditions, where $\theta$ is the angle formed by the incident and scattered light (red arrows) with respect to the normal axis to the sample surface. The specular reflectance shows a minimum when the incident radiation is along the wire vertical axis, remaining inferior to 1% below 60° incident angles for all three excitation wavelengths. Therefore, the angle-resolved measurement ensures that visible light trapping is not affected by the radiation incidence angle.
These results configure the 2D Si NWs random fractal materials as a promising architecture for low-cost, scalable Si-based photovoltaic cells, guaranteeing a high light trapping efficiency during the all day.

### 3.3.2 Coherent backscattering and localization of light

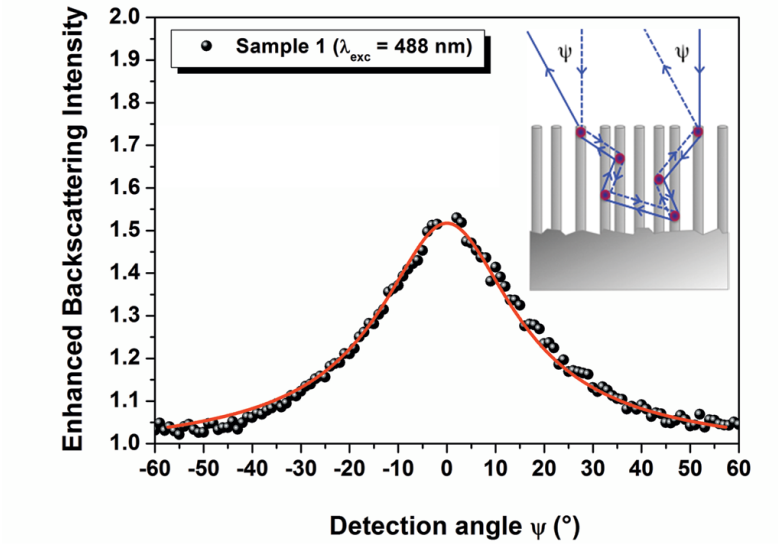


*Figure 3.9: Coherent backscattering cone (black dots) of sample 1 obtained at the excitation wavelength of 488 nm fitted by the semi-infinite slab model (red line). The inset represents a schematic of the coherent backscattering mechanism.*

Another clear evidence confirming the occurrence of strong in-plane multiple scattering in Si NWs is demonstrated by coherent backscattering measurements. The scattering strength of Si NW sample 1 has been tested through the coherent backscattering of light. Coherent backscattering (CBS) is a light transport phenomenon occurring in disordered media [139, 140].
Momentum-reversed scattered waves interfere constructively in the exact backscattering direction, as illustrated schematically in the inset of fig. 3.9. A rapid dephasing develops between the counter-propagating waves departing from the backscattering direction. The dephasing mechanism arises due to the averaging of light path lengths traveled in the medium, resulting in a typical cone shape for the angular-dependent scattered intensity [141].

The backscattering intensity for sample 1 has been acquired with an homemade angular scatterometer exciting the system with the 488 nm line of an $Ar^+$ laser. The measured intensity has been normalized for the diffusive background to obtain the enhanced backscattered intensity. In fig. 3.9, the enhanced backscattered intensity (black dots) is reported as a function of the detection angle ($\phi$), obtaining the typical CBS cone.
The CBS trend has been fitted by a semi-infinite slab model (red line) in fig. 3.9, considering an xy-plan of Si NWs having thickness ($L$) in the limit of $L \to \infty$. A detailed study on the scattering strength of both ordered and disorder Si, InP and especially GaP NWs has been performed by Muskens group. In particular, the transport mean free path $l_t$ has been investigated for GaP NWs as a function of the diameter, obtaining a minimum value of about $160nm$ for 110 nm diameter GaP NWs [142]. As far as Si NWs fractal arrays are concerned, a transport mean free path $l_t \sim 160$ nm has been measured from the CBS cone full width at half maximum (FWHM) when using the 488 nm $Ar^+$ laser line as excitation wavelength. This value is far below the case of $TiO_2$ powder, confirming the impressive scattering strength of fractal Si NW arrays in comparison to well known high refractive index materials. Furthermore, a strategic advantage of fractal geometry is related to the well known presence of electromagnetic field localization. In fact, fractal dilation symmetry and lack of translation invariance properties lead to the spatially localization of propagating waves that are not eigenfunctions of the dilation symmetry operator [134]. An infinite random fractal present heterogeneities correlated on all length scales, allowing to resonantly match the structure with a broad range of incident wavelengths. In some cases, this behavior can lead to inhomogeneous localizations of the electromagnetic field where both spatially localized and delocalized modes coexist [118, 143]. This typical property of a fractal structure results in the formation of hot-spot regions, where the intensity of the electromagnetic field is enhanced [144, 145].

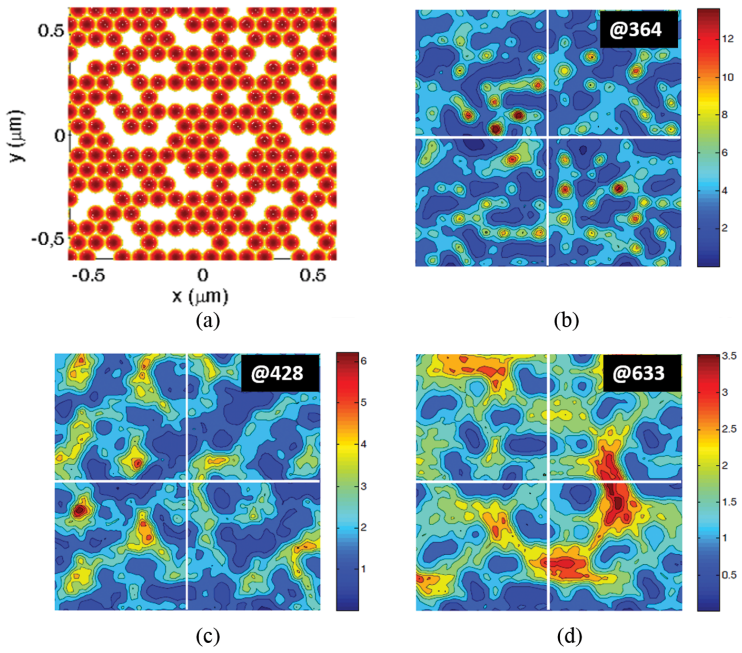


*Figure 3.10: (a) Model random structure simulating Si NW array. Near field intensity maps simulated by transition matrix approach for (b) 364 nm, (c) 428 nm and (d) 633 nm excitation wavelength, respectively.*

Our Si NW arrays are a finite fractal showing a wavelength matching overall the visible and near-IR range, up to 1100 nm. For such a wavelength range it can be assumed to have our cavity distribution. In order to prove this hypothesis the 2D Si NW random fractal array has been simulated by using the transition matrix approach in order to test hot spot formations [146, 147]. A Si NWs array is a highly complex 3D structure to be represented and simulated. Therefore, the system has been approximated by a random distribution of 300 nanospherical particles with 40 nm of radius. The particle have been arranged by using the MBC approach to fully cover an area of 600x600 $nm^2$, as shown in fig. 3.10 (a), to reproduce the structure and the lacunarity of the array in the best possible manner. The particle dimensions and arrangement have been chosen in order to reproduce the heterogeneity size for which lacunarity is maximum for sample 1. The particle refractive index has been measured by the Bruggeman mixing rule assuming a composition of 70% Si and 30% $SiO_2$.

The amplitude of the radiation scattered from the structure ($E_{sca}$) has been simulated and compared to the incident electric field one ($E_{inc}$). The near field normalized intensity $|E_{sca}/E_{inc}|^2$ distribution is presented in a false color map in fig. 3.10, for (b) 364 nm, (c) 428 nm and (d) 633 nm excitation wavelengths. The wavelength choice is justified since Si NW arrays are finite fractals having a strong visible wavelength matching. In particular, a quite good matching with the sample lacunarity is observed at the 364 nm excitation wavelength. The formation of hot spot regions having dimensions smaller than $\lambda_{inc}$ has been calculated for all the investigated excitations. The hot spot distribution is more localized and intense at shorter wavelength (fig. 3.10(b)), as expected from sample lacunarity trend (sample 1). When the wavelength increases (c-d) the hot spot regions appear more enlarged and delocalized along the structure. In fact the scattered field intensity is reduced by half for 428 nm (c) and by a factor of 3 for 633 nm (d). These simulations prove the occurrence of field localization in random systems. The achieved result for a random geometry appears even more remarkable for dilation symmetric systems, as fractals.
Thus the simulation results obtained for a random structure can be extended to a fractal model having heterogeneity correlated on all length scales included between the size of the nanospherical particles to that corresponding to the dimensions of the fractal. Indeed, for 2D Si NW fractal arrays it is always possible to match the inhomogeneities length scale for whatever visible incident wavelength. Therefore, the refractive index fluctuations due to the structure generate a strong scattering, possibly leading to interesting localization effects. Although the presented simulations are very promising the experimental demonstration of the occurrence of field localization is still quite complex.

### 3.3.3 Raman and emission properties

The fractal geometry strongly influences the Si NW optical properties, particularly affecting their emission. The influence of such a peculiar structure to determine the NW emission characteristics has been investigated by studying Raman and PL emission as a function of the incident wavelength. Si NW array has been excited with the 488 nm line of a $Ar^+$ laser at a power of 20 mW. The laser beam was focused on a 100 $\mu m$ diameter spot by mean of a high numerical aperture (NA = 0.9) 100x air objective. NW emission spectrum have been acquired by using a micro-Raman spectrometer, equipped with a cooled CCD for visible wavelength detection. For this measurement a long-pass edge filter at 488 nm has been used to suppress Rayleigh scattering by 6 order of magnitude. All measurements have been performed at room temperature.

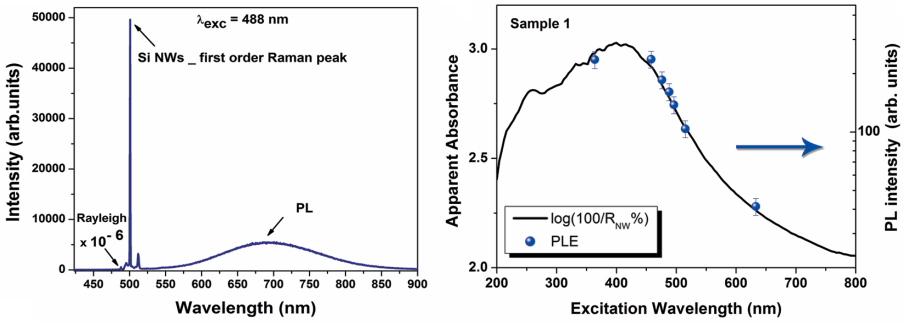


(a) (b)

*Figure 3.11: (a) Si NWs sample 1 Raman and PL emissions obtained by exciting with at the 488 nm line of an $Ar^+$ laser (power 20 mW on a 100$\mu m$ diameter laser spot). (b) Sample 1 PL intensities detected at 690 nm are plotted as a function of the incident wavelength (blue dots) with respect to the apparent absorbance of the sample (black lines). The blue arrow indicates the y-axis corresponding to the plotted PLE data.*

Both Raman scattering and PL emission from a 2.5 $\mu m$ long, (111)-oriented Si NW array (sample 1) are presented in fig. 3.11(a). Two impressive and sharp peaks are visible at about 500 nm and 513 nm, respectively corresponding to Si NW first and second-order Raman signals, followed by a broad PL emission centered at 690 nm due to the size distribution of quantum confined Si NWs [62, 61].

In particular, a remarkably high Si NWs Raman signal is observed in comparison to PL emission. In order to correlate the NW optical response to the fractal parameters, the photoluminescence excitations (PLE) and the Raman enhancement are reported for different excitation wavelengths for sample 1 (fig. 3.11 (b), 3.12 (a)) and sample 2 ( fig. 3.12 (b)) respectively. NW PL emission has been acquired for seven different excitation wavelengths ranging in the visible region. Sample 1 PL intensity detected at 690 nm has been plotted as a function of the incident wavelength to obtain the photoluminescence excitation spectrum (PLE) reported in blue dots in fig. 3.11(b). The blue arrow indicates the y-axis corresponding to the PLE data and the error bars take into account the intensity fluctuation occurring in different points of the sample.
The PLE is compared with respect to the apparent absorbance of sample 1 plotted in a continuous black line. The apparent absorbance is defined as the logarithm of the inverse of NW total reflectance, $log\frac{100}{R_{NW\%}}$, where the NW reflectance has been normalized to the Si bulk reference to take into account the influence of the Si NW layer only. This quantity represents the extinction of the system measuring both scattering and absorption and it is therefore related to the lacunarity of the structure. Indeed, sample 1 apparent absorbance shows a maximum at about 428 nm arising when the effective wavelength $\lambda_{eff}$ traveling in the NW layer matches the maximum of the refractive index fluctuations corresponding to the lacunarity peak. When this occurrence is fulfilled the in-plane multiple scattering processes in the fractal NW array become more relevant.

It is very impressive to observe that the PLE behavior perfectly reproduces the apparent absorbance trend corresponding to the same sample. Further confirming that the PL emission is driven by the morphology of the fractal array.

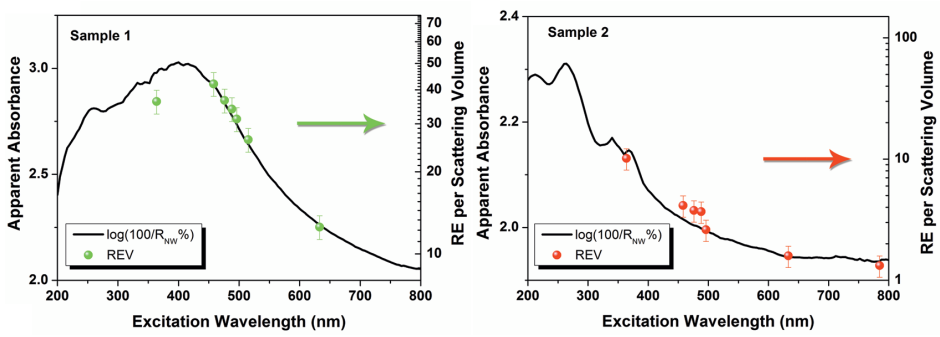


(a) (b)

*Figure 3.12: Si NW Raman enhancement per scattering volume (REV) measured for (a) sample 1 (green dots) and (b) sample 2 (red dots) with respect to the Si bulk reference. Both trends are plotted as a function of the incident wavelength and compared to the apparent absorbance of the corresponding sample (black lines). The arrows indicate the y-axis corresponding to the REV data having the same color.*

Furthermore, Raman measurements have been acquired by means of a micro-Raman spectrometer, focusing the excitation on the sample by a 100x air objective (NA = 0.9). The same power on the sample plane has been adopted for all the different wavelengths used. The Raman enhancement is measured for each exciting wavelength as the ratio of the first-order NW Raman peak integrated intensities normalized with respect to the first-order Si bulk peak acquired under the same experimental conditions.
Finally, the Raman enhancement per scattering volume (REV) has been calculated by normalizing the Raman enhancement to the portion of effectively probed Si NW volume (40%). This value is estimated from structural analysis considering a system composition made of 40% air voids, 20% $SiO_2$ and 40% Si, in agreement with the composition used to calculate the effective refractive index according to the Bruggeman mixing rule. REV trends as a function of the excitation wavelength are presented in fig. 3.12(a) for sample 1 (green dots) and (b) sample 2 (red dots) respectively referring to the right y-axis and compared to the apparent absorbance (black line) of the corresponding sample reported on the left y-axis.

The Raman enhancement trends, as well as PLE behavior, follow quite well the apparent absorbance shape for both NW samples, once again attesting a perfect match between the scattering and the structural properties of the 2D Si NW fractal array. It can be concluded that the scattering induced from the fractal structure promotes the increment of the dwell time of the excitation pump inside the material, leading to an increment of Si NWs optical emission.

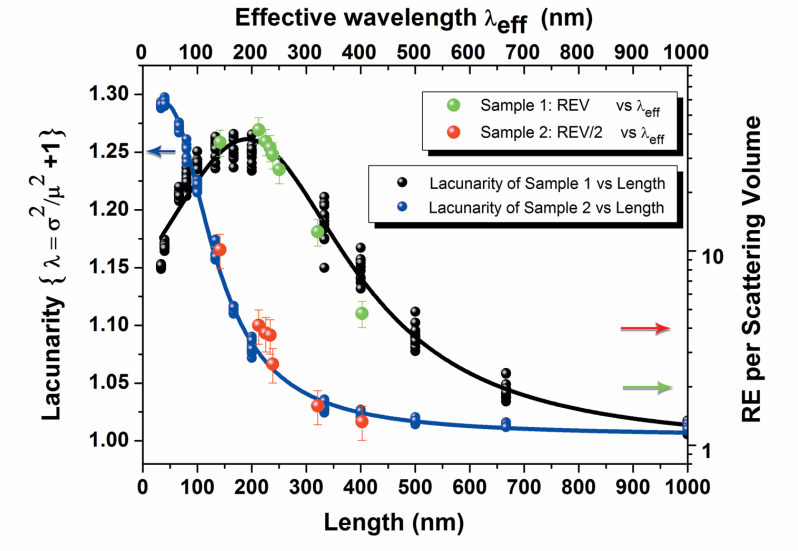


*Figure 3.13: Raman enhancement per scattering volume plotted as a function of the effective wavelength for sample 1 (green dots) and sample 2 (red dots). REV trends are shown in comparison to the lacunarity curves marked as black and blue dots for samples 1 and sample 2 respectively.*

An impressive confirmation of the key-role played by lacunarity to determine the emission properties of a Si NW array is here reported. Indeed, figure 3.13 reports the lacunarity behavior as a function of the length scale respectively for samples 1 (black dots) and 2 (blue dots). The lines represent a guide for the eye. The lacunarity for both samples is compared to the REV trends plotted as a function of $\lambda_{eff}$ on the right axis for sample 1 (green dots) and sample 2 (red dots). Lacunarity directly determines the in-plane multiple scattering occurring inside the material. Therefore, the Raman scattering is strongly linked to the lacunarity of the system. In fact, the perfect matching between lacunarity and REV reported for both NW

samples in fig. 3.13, unequivocally attests that the structural heterogeneity distribution, typically observed in fractals, is the main responsible for the scattering phenomena and therefore for the NW Raman emission.
Furthermore, fig. 3.13 highlights how the REV is correlated on the overall investigated length scales, that is a typical characteristic of a finite fractal structure [148]. The capability to control Si NW emission properties by tuning the fractal lacunarity attests the great potential of these systems for photonic applications.

## 3.4 Conclusion

In this chapter the synthesis of two-dimensional random fractal array of vertically aligned Si NWs has been demonstrated by metal assisted chemical etching, a well controlled, low-cost and Si-techno-logy compatible technique. Indeed, by using gold fractal films as negative masks for NW synthesis, the fractal structure is transferred to the NW array, whose planar arrangement results complimentary to Au ones.
The design of different fractal NW arrays has been realized by varying the filling factor of the Au precursor or the crystalline Si substrate orientation. The self-similarity and the scale invariance of the NW fractal array has been tested by SEM structural investigation demonstrating a NW filling factor of about 60% for different magnification scales. Moreover, a detailed structural characterization on Si NW samples led to the identification of two fractal key role parameters: the fractal dimension and lacunarity.A fractal dimension close to the typical value of two has been estimated attesting the two-dimensionality of the structures whereas the lacunarity trend confirms the presence of heterogeneities for a broad range of length scale between 20 nm and about 1 $\mu m$. The strong relation among the optical properties and the structural features of the fractals have been demonstrated. In particular an efficient light trapping in the visible range characterized by reflectivity lower than 1% associated to the fractal arrangement of the structure is clearly shown. An over-trapping feature has also been observed (reflectance below 0.1%) when effective wavelength traveling in the medium matches the maximum of lacunarity, improving the scattering efficiency for the structure and further confirming that the lacunarity is the main factor determining the scarttering properties of the sample.
Strong in-plane multiple scattering has been also demonstrated from transmittance and CBS analysis, measuring a transport mean free path of 160 nm typical of strongly scattering materials. Hot-spots occurrence in a fractal system are very well reported in literature. Hot-spots formation has been simulated for different visible wavelengths by using the transition matrix approach. When miming the fractal with a random structure having similar structural parameters the hot spot formation has been predicted to be more intense and

localized for shorted wavelengths, as expected from the lacunarity trend of the samples.

Finally, the correlation among the fractal parameters and the optical response of the system has been demonstrated, reporting a remarkably high Raman peak and efficient room temperature PL emission. The Raman enhancement and photoluminescence excitation have been compared to the apparent absorbance of the system, attesting the strong correlation between the heterogeneity distribution (lacunarity), the scattering and absorption properties of the structure. The impressive light trapping obtained by the disordered fractal structure configures this material as very promising for Si-based photovoltaic. Moreover, such tunable heterogeneity distribution over a wide range of length scales makes this material also suitable for optics, especially for the new emerging area of fractal antennas.

# Chapter 4

# Coherent backscattering of light in silicon nanowire arrays

**Abstract**

Disordered media usually manifest very exotic optical properties. Indeed, the high structural disorder can limit the light transport (weak localization) to such an extent that the diffusion is completely halted (Anderson localization). In particular, multiple scattering phenomena play a crucial role for the optical properties of Si NWs leading to the observation of fascinating physical effects. This chapter exploits the light transport in Si NW arrays by means of coherent backscattering (CBS). Coherent backscattering is observed in strongly scattering media as an enhancement of the intensity of light scattered in the backward direction due to the constructive interference between the direct and reversed light paths. This chapter provides the experimental observation of an unexpected constructive interference for inelastically backscattered Raman light from strongly diffusing Si NW arrays. This surprising phenomenon originates from the coherent nature of the Raman scattering process occurring within a length scale of the phonon coherence length of a few tens of nanometers. The observation of the coherent backscattering of Raman light (RCBS) has been interpreted using a mixed hybrid Rayleigh-Raman random walk approximation, clarifying the role of phase coherence in multiple scattering phenomena. The remarkable optical properties demonstrated for Si NW arrays can be employed for many modern applications where the radiation-matter interaction has to be increased.

## 4.1 Optical transport in disordered materials

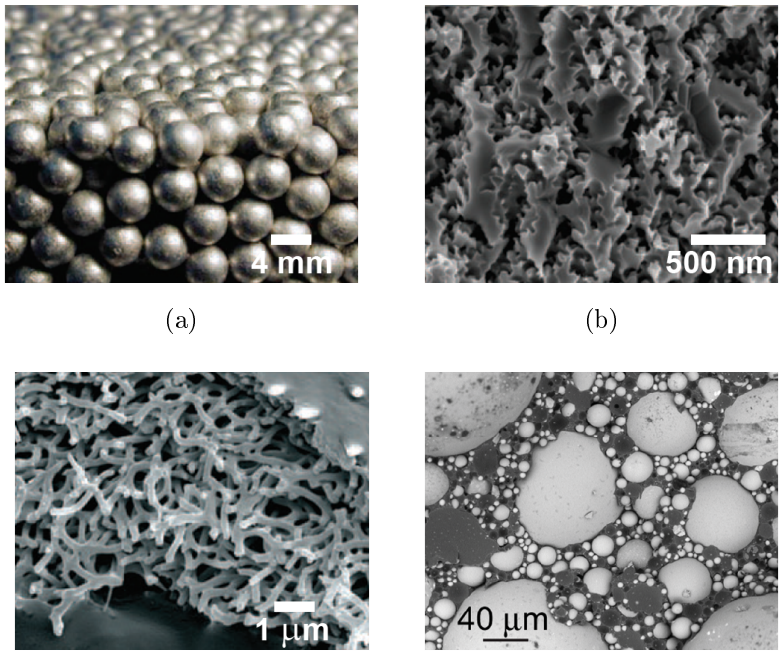


*Figure 4.1: Some examples of disordered materials: (a) brazed aluminium beads network with diameter of 4 mm, (b) porous gallium phosphide wall obtained by sulphuric acid etching, (c) disordered nanofibrils naturally arranged into white beatles scales, (d) disordered titanium dioxide particles ramdomly arranged in a Lèvy glass [148, 149, 150].*

The design of new materials with engineered properties allows the realization of novel mechanical, electrical, magnetic, chemical, biological [151], and optical devices [140, 152]. Many recent papers investigated the influence of disorder on the physical properties of materials leading to observation of new fascinating phenomena [153]. It has been demonstrated that the physical properties of disordered structures can surpass ordered ones and the investigation on the order-disorder phase transition is of interest to tune the material properties [154]. The definition of disorder lies on the lack of some

long range symmetry (i.e. translation, rotational.) correlation and is generally related to the dimensionality of the system. Some example of disordered materials are presented in fig. 4.1, such as a (a) network of brazed aluminium beads, (b) porous gallium phosphide etched in sulphuric acid, (c) the nanofibrils of white beatles scales or (d) the random $TiO_2$ particles arrangement in a Lèvy glass. [148, 149, 150]. Disordered materials present some critical aspects, indeed it is extremely complex to quantify their structural disorder and to identify some characteristic physical parameters. In fact, heterogeneous media cannot be described by the same quantity as for homogeneous structures since their density and structural parameters can be very different [155, 151]. A change in the structural properties is reflected on the deformation resistance to mechanical stress, thermal distribution, electrical conductivity and especially optical diffusion. Therefore new effective quantities must be defined such as an effective elastic module, effective diffusivity and so on, in order to correlate the physical properties to the structural degree of disorder. As an example in percolative films the electric conductivity and their optical behavior can be defined as a function of the percolation factor, while the optical behavior of porous structures can be described using the effective dielectric constant either defining an effective optical thickness that can be very different from the one associated to the homogeneous structure composed of the same material.

Transport processes in disordered materials constitute an important class of problems. Some examples of a transport process in disordered materials includes hopping transport in amorphous semiconductors, frequency-dependent conduction in superionic conductors, diffusion in microporous materials and biological tissues, stress deformation, optical processes in heterogeneous materials, and many more [156, 157].
In particular, optical scattering in a random medium may induce a phase transition in the photon transport behavior leading to the regime of light localization, the optical analog phenomenon of Anderson localization for electrons in a solid [149]. Light transport in disordered media is described by a diffusion process in the weak scattering regime [158]. Strong localization is expected once the (elastic) scattering mean free path $l_s$ decreases below the light wavelength (Ioffe-Regel criterion $kl_s \ll 1$) [141]. However, contrary to electron

localization, this criterion is extremely difficult to satisfy for electromagnetic waves since the scattering cross-section is a function of the fourth power of the wavelength ($\sigma_s \sim \lambda^{-4}$). Nonetheless, recurrent light scattering events can arise by increasing the scattering probability as manifested in disordered materials [148]. The interference between the counterpropagating waves in a disordered structure gives rise to the enhanced backscattering, also called weak localization [159, 160]. Light localization can lead to amplification in random media, where a photon may induce the stimulated emission of a second photon (i.e. random lasing in disordered media) [161]. Disorder-induced optical scattering provides coherent feedback for lasing and also leads to spatial confinement of light in micrometer-sized volume. Indeed, the fabrication of randomly assembled ZnO nanocrystallites microlasers has been reported [162] and some indirect evidences of Anderson localization of light in a ZnO nanoparticles random medium have been demonstrated [163]. Here we demonstrate the weak localization of light in Si NW disordered arrays by coherent backscattering measurements in both elastic (Rayleigh) and inelastic (Raman) cases.

## 4.2 Brief theory of coherent backscattering of light

Coherent Backscattering (CBS), or in a more old-fashioned way "the coherent albedo", is a phenomenon observed for light scattered from disordered media where photons traveling in the exact backscattered direction interfere constructively with their reciprocal path leading to a 2-fold enhancement for the scattered intensity. The coherent backscattering can be explained on the basis on the reciprocity theorem applied to optics. It states that "the scattering amplitude for a **B** polarized scattered wave in the direction $\overrightarrow{k}_{out}$ arising from an **A** polarized incident wave in the direction $\overrightarrow{k}_{in}$ is equal to the amplitude for an **A** polarized scattered wave in the direction $-\overrightarrow{k}_{in}$ from a **B** polarized incident wave in the direction $-\overrightarrow{k}_{out}$" [164]. Light that is multiply scattered does not lose its wave character and can interfere both during and after the scattering process. Indeed, optical information is not lost during elastic scattering processes and multiple scattering is in principle fully reversible owing to reciprocity. The power of the reciprocity principle lies largely in the fact that it is applicable even in the presence of absorption when time-reversal symmetry is lacking, as discussed in detail by Carminati et al. [165]. In order to describe the CBS phenomenon it is important to describe how light can propagate within a disordered system. The scattering mean free path $l_s$ is the average distance traveled by the light between two consecutive scattering events and defines the light scattering inside a medium:

$$l_s = \frac{1}{\rho_N \sigma_s} \tag{4.1}$$

where $\rho_N$ is the density of the scattering centers and $\sigma_s$ is the total scattering cross section. In weakly scattering systems, the intensity $I(z)$ of the scattered plane wave is attenuated exponentially along the propagation distance **z** due to scattering processes according to the Beer-Lambert law:

$$I(z) = I(0) \cdot e^{-\frac{z}{l_s}} \tag{4.2}$$

The single scattering regime is achieved when the condition $z \ll l_s$ is satisfied, so that the scattered intensity is quickly damped.

For $z \geq l_s$ the multiple scattering regime is obtained and a distinction between isotropic and anisotropic scattering must be made. The Rayleigh scattering regime describes the isotropic scattering of light observed when the scatterer diameter is much smaller compared to the incoming wavelength ($d \ll \lambda$). Whereas, for $d \geq \lambda$ light is scattered in the forward direction perpendicular to the surface, such as in the anisotropic Mie scattering regime for spherical particles.
Light propagation in disordered material occurring in the multiple scattering regime can be described by considering the random walk approach, also known as "drunken problem" [158]. The characteristic parameter that is always non null in the random walk description is the mean square displacement for diffused light, defined in 3D space as: $\langle|\overrightarrow{r}^2|\rangle = \langle x^2\rangle + \langle y^2\rangle + \langle z^2\rangle$. Under the isotropic assumption, the random walk problem can be further simplified considering the light transport occurring along one direction only ($\overrightarrow{x}$) and the mean square displacement can be reformulated as:

$$\left\langle x^2 \right\rangle = n \left\langle \Delta x^2 \right\rangle \frac{2nl_s^2}{d} = \frac{2Ll_s}{d} \tag{4.3}$$

where $n$ is the number of scattering events, $\Delta x^2$ is the mean square of the projection of the step length on the x-axis, d is the dimension of the system and $L = nl_s$ is the total length, i.e. the average distance traveled by light during the scattering process. The 2-factor in eq. 4.3 arises from the exponential distribution of the scattering step length $P(\Delta r) = exp^{-\frac{(\Delta r/l)}{l}}$ assumed from the Lambert-Beer law (eq. 4.2) that holds still for multiple scattering media. For anisotropic scattering conditions, the mean square displacement along one direction is reduced by the following amount:

$$\left\langle x^2 \right\rangle = \frac{2L}{d} \frac{l_s}{1 - \langle cos\theta \rangle} = \frac{2L}{d} l_t \tag{4.4}$$

being $\theta$ the scattering angle with respect to the incident beam and $(1 - \langle cos\theta \rangle)$ is the structure factor of the medium. Eq. 4.4 implies that more scattering events are required to randomize the light propagation direction for anisotropic scatters compared to the isotropic case. A new characteristic length is introduced in eq. 4.4 as follows:

$$l_t = \frac{l_s}{1 - \langle cos\theta \rangle} \tag{4.5}$$

The transport mean free path $l_t$ is the typical distance traveled by the light before its propagation direction becomes random [166]. The total length can be now expressed as a function of $l_t$ as $L = nl_s = n_t l_t$, by introducing the effective number of scattering events $n_t = n(1 - \langle cos\theta \rangle)$. Consequently, a random walk of $n$ correlated scattering events of average length $l_s$ can be replaced by a random walk of $n_t$ non-correlated events of average length $l_t$. The multiple scattering regime manifests for $n_t \gg 1$.
When the number of scattering events is high, as for multiple scattering, the propagation of light can be described by the diffusion approximation considering the diffuse transport of energy. In particular, the random walk approach is equivalent to the diffusion approximation for $n_t \geq 10$ [167]. The physics of multiple scattering can best be understood by adopting a diffusion picture for the multiply scattered light. Qualitatively, it can be explained by the fact that a random walk is recurrent in two dimensions, and the total sojourn time becomes infinite as for Anderson localization of electrons. Consequently, the effective cross section of a single scatterer tends to infinity, drastically reducing the effective mean free path [168].
The diffusion approximation provides a qualitative explanation of the coherent backscattering effect in terms of the intensity of scattered light according to the diffusion equation:

$$\frac{\partial I(\mathbf{r},t)}{\partial t} = D \times \nabla^2 I(\mathbf{r},t) - \frac{1}{\tau_{abs}} I(\mathbf{r},t) \tag{4.6}$$

where $I(\mathbf{r},t)$ is the light intensity, $D = \frac{vl_t}{d}$ is the diffusion coefficient depending on the transport velocity $v$, and $\frac{1}{\tau_{abs}}$ is the light absorption rate typical of the sample.

Figure 4.2 displays the incoming plane waves $I_{in}$ illuminating the sample at an angle $\theta$ with respect to the surface normal direction. The scattered intensity is collected at a detection angle $\psi$ with respect to the normal axis, while $\theta_b$ refers to the backscattering direction.
According to the Lambert law, the angular dependence of the scattered intensity $I_{out}(\psi)$ is very low departing away from the backscattered direction. Indeed, the probability for a photon of being scattered at a distance $\mathbf{z}$ from the sample surface and then to exit from it decreases exponentially with $\psi$ $\left(P_{out} \propto e^{-\frac{z}{l_t cos\psi}}\right)$.

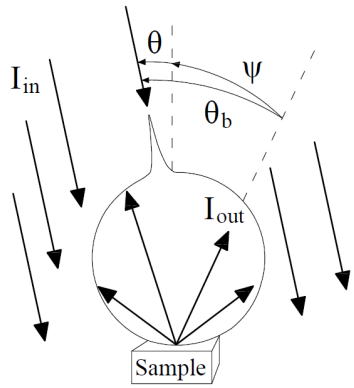


*Figure 4.2: Illustration of a typical scattering pattern observed from the multiple scattering of light within a disordered sample [169].*

Whereas, a clear enhancement is observed for the scattered intensity in the backscattering direction for $\theta + \psi = \theta_b$ due to the constructive interference between an optical path and its reversal, whose existence is guaranteed by the reciprocity theorem. Afar from the backscattered direction the coherent interference is rapidly mixed with the incoherent background. Considering $P_\uparrow$ and $P_\downarrow$ as the matrices associated respectively to the forward and reverse optical path of the scattered light, the reciprocity theorem states that the $P_\uparrow = P_\downarrow^T$ where the $T$-apex stands for transposed matrix. This concept also involves the polarization states of light in both paths. At a first approximation the backscattering problem can be treated neglecting the polarization issue.
Figure 4.3 shows a typical example of an optical ray that enters into the sample, undergoes towards multiple scattering and then exit from the surface (solid line). Each optical path is followed by its reverse counterpart plotted as a dashed line in the same figure. The two rays interfere constructively for $\theta_b = 0$ since they travel exactly the same distance, giving a 2-fold enhancement of the emitted intensity with respect the incoherent lambertian background. By moving away from the exact backscattering direction, the phase difference between the two paths is no longer 0, but is equivalent to $\Delta\phi = (\overrightarrow{k}_{out} + \overrightarrow{k}_{in}) \cdot \overrightarrow{r} = \overrightarrow{q_b} \cdot \overrightarrow{r}$, where $\overrightarrow{q_b}$ is the backscattering vector and $\overrightarrow{r}$ the net path difference.

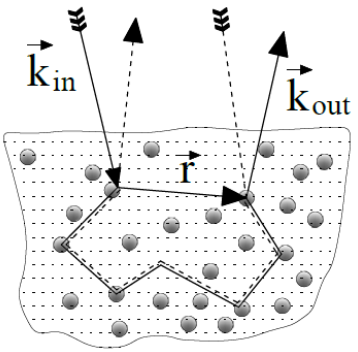


*Figure 4.3: Schematic illustration of the coherent backscattering phenomenon [169].*

The CBS enhancement (CBE) is obtained from the coherent superposition of the reciprocal paths ($|A_\uparrow + A_\downarrow|^2$) weighted to their incoherent contribution ($|A_\uparrow|^2 + |A_\downarrow|^2$):

$$CBE(\overrightarrow{q_b}, \overrightarrow{r}) = \frac{|A_\uparrow + A_\downarrow|^2}{|A_\uparrow|^2 + |A_\downarrow|^2} = 1 + cos(\overrightarrow{q_b} \cdot \overrightarrow{r}) \qquad (4.7)$$

being $A_\uparrow$ and $A_\downarrow$ the field amplitude of the direct and reverse path respectively. By increasing the distance **r** between entrance and exits points, the cosine in eq. 4.7 oscillates faster. Thus the coherent contributions are washed out while moving away from the backscattering direction. The 2 maximum enhancement factor is then obtained for $q_b \cdot r \sim 0$.

In order to obtain some important qualitative features of the CBS cone, we assume that $\overrightarrow{r}$ is parallel to the xy-plane corresponding to the sample surface ($\overrightarrow{r} \sim r_{xy}$) and $\theta_b \ll 1$ as well as $q_b \ll 1$. For simplicity the incidence is considered normal ($I_{in} \perp xy$), meaning that $\theta = 0$ and $\theta_b = \psi$ as considered during the experimental measurements. The optical path difference $\Delta L$ introduces a phase shift of $\Delta\phi = k_0 \Delta L \sim k_0 r_{xy} \psi$ when evaluated in air ($k_0 = \frac{2\pi}{\lambda_0}$). The phase difference $\Delta\phi$ increases linearly by increasing the backscattering angle $\psi$. Until now, only the multiple scattering has been considered in the evaluation of the CBS cone. However a significant fraction of the incoming light can be backscattered due to single scattering, which is significant for isotropic scatterers. This incoherent contribution has to be taken into account since it reduces the enhancement factor.

The CBE relation reported in eq. 4.7 can be then expressed as a function of the incoherent contribution of both multiple and single scattering processes (INC) defined as follow:

$$CBE(\mathbf{q_b}) = 1 + \frac{1}{INC}\int_{r_{xy}\sim\lambda_0}^{+\infty} I(\mathbf{r}_{xy})cos(\mathbf{q_b}\cdot\mathbf{r}_{xy})d\mathbf{r}_{xy} \tag{4.8}$$

$$INC = \int_{r_{xy}=\sim\lambda_0}^{+\infty} I(\mathbf{r}_{xy})d\mathbf{r}_{xy} + \int_{r_{xy}=0}^{\sim\lambda_0} I(\mathbf{r}_{xy})d\mathbf{r}_{xy} \tag{4.9}$$

Thus the coherent backscattering profile is given by the Fourier transform of the radial intensity profile $I(\mathbf{r}_{xy})$ around the point-like illumination center, as expected from the cosine trend described in eq. 4.7. The fundamental coherent backscattering enhancement expression is obtained by substituting the explicit form of $I(r_{xy})$ obtained from the diffusion approximation (eq. 4.6) in eq. 4.9:

$$CBE(\overrightarrow{q_b}) = 1 + C\int_{L>0}^{+\infty} p(\mathbf{L})e^{-\frac{1}{3}l_t q_b^2 L}dL \tag{4.10}$$

where $p(L)$ is the distribution of the optical path lengths $L$ inside the material while the $C$ parameter ($C \in [0,1]$) strictly depends on the type of scatterer, light absorption and polarization.
As expressed in eq. 4.10, the profile of the coherent backscattering cone that is given by the sum of several Gaussians whose width decreases by increasing $L$ and is weighted by the optical path lengths distribution $p(\mathbf{L})$. Indeed, longer paths introduce lower weights giving rise to the typical triangular shape of the cone tip. The cone angular $FWHM_\psi$ is proportional to $\propto \frac{\lambda_e}{l_t}$, being $\lambda_e$ the wavelength corresponding to the surrounding environment.
The absorption and polarization influences have been neglected up to now. However, the material absorption is characterized by the typical absorption length $l_i$ and plays the only role of reducing the total number of outcoming photons, without altering the interference between direct and reverse paths. In fact by introducing the absorption term $\sim e^{-\frac{L}{l_i}}$ in eq. 4.10 results in the definition of an effective absorption length $L_a = \sqrt{\frac{l_t l_i}{3}}$ for the material. $L_a$ defines the superior integration limit for CBE expression and the contributions of the optical paths $L$ longer than $L_a$ is excluded.

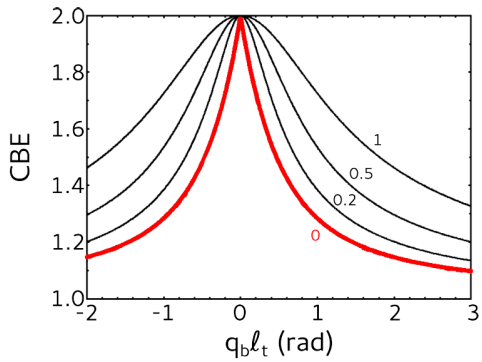


*Figure 4.4: Simulation showing the absorption influence on the CBE profile computed for $\frac{l_t}{l_i} = 0$ (red line), 0.2, 0.5, 1 (single scattering contribution has been neglected).*

As an effect of the material absorption the cone tip is rounded off as sketched in fig. 4.4. Moreover, the CBS enhancement is generally reduced due to the absorption in the presence of single scattering, affecting the definition of the $C$ parameter (eq. 4.10) [167]. In practical situations the effect of absorption cannot be totally excluded and can be further generalized to the case of sample of finite dimension whose reduced thickness generally wash out the long-path contributions. Finally, the effects of light polarization can be taken into account.

According to the reciprocity theorem, the complex amplitude associated to the direct wave path that passes through the polarizer P, undergoes to multiple scattering path $P_\uparrow$ and then crosses the analyser A is equal to the complex amplitude of the reverse path A-$P_\downarrow$-P. Thus the previous analysis is strictly valid only when the incident and detected polarizations are the same, in the so called *polarization* (linear or circular) *conserving channel*. Different contributions to the CBS intensity can be suppressed (or not) depending on the considered polarization channel. Indeed, it is always possible to obtain the maximum CBE regardless of scatterer type for the circular conserving channel only, for which the reciprocity theorem prediction is unaffected by the presence of single scattering events. The other channels are otherwise affected by the presence of single scattering events and CBS enhancement factors typically lower than the maximum value are achieved.

In order to complete the description of the weak localization theory, the time-independent Helmholtz equation for the electric field components $E(\mathbf{r})$ inside or outside the scatterers can be considered:

$$\nabla^2 E(\mathbf{r}) + \left(\frac{\omega}{c_o}\right)^2 \epsilon(\mathbf{r}) E(\mathbf{r}) = 0 \tag{4.11}$$

where $\epsilon(\mathbf{r})$ is the random dielectric constant of the system, $\omega$ the frequency of the incoming radiation and $c_0$ the light velocity in vacuum. The wave equation can then be written as:

$$\nabla^2 E(\mathbf{r}) + \left(\frac{\omega}{c_o}\right)^2 E(\mathbf{r}) = V(\mathbf{r}) E(\mathbf{r}) \tag{4.12}$$

considering as the scattering potential $V(\mathbf{r})$:

$$V(\mathbf{r}) = -\left(\frac{\omega}{c_o}\right)^2 (\epsilon(\mathbf{r}) - 1) \tag{4.13}$$

The scattering potential for point-like scatterers immersed in air environment, having polarizability $\alpha_0$ and position $r_i$ can be defined as follows:

$$V(\mathbf{r}) = -\alpha_0 \left(\frac{\omega}{c_o}\right)^2 \sum_i \delta\left(\mathbf{r} - \mathbf{r}_i\right) \tag{4.14}$$

A non trivial solution of the problem can be obtained by using the Green function and the transition-matrix formalism to the equations 4.12 and 4.14, under the assumption of self-avoided multiple scattering (SAMS) approximations in order to neglect recursive multiple scattering.
A relationship among the averaged scattering intensity $\langle I(\mathbf{r})\rangle$ and the bistatic scattering coefficient $\gamma$ is achieved from these considerations (mathematical details can be found in ref. [169]).

$$\gamma = \frac{4\pi r^2}{A} \frac{\langle I(\mathbf{r})\rangle}{I_0} \tag{4.15}$$

The total bistatic coefficient $\gamma$ is defined as the measured scattered flux per solid angle $\Omega = 4\pi r^2$ and per unit of area $A$, normalized to the incident flux $I_0$. The bistatic scattering coefficient is described by the sum of three components due to the single scattering events $\gamma_s$, the diffused incoherent multiple scattering Lambert background $\gamma_l$ and finally the interference term $\gamma_c$.
It is possible to express the coherent backscattering enhancement CBE as a function of the bistatic scattering coefficients:

$$CBE(\psi) = \frac{\gamma_s + \gamma_l + \gamma_c}{\gamma_s + \gamma_l} \tag{4.16}$$

Eq. 4.16 remarks the fundamental role played by single scattering, as already mentioned before and it has been used to fit the experimental CBE profile for Rayleigh scattering. Assuming $\gamma_s = 0$ lead to the maximum enhancement factor E=2 for $\psi = 0$ since $\gamma_l = \gamma_c$ in the exact backscattering direction under such condition. The $\gamma_s = 0$ condition is verified for the scattering from spherical symmetric scatterers measured in the helicity conserving polarization channel.
In the limit of a finite slab having thickness L, the coherent interference term $\gamma_c$ coefficient assumes the following form:

$$\begin{aligned}
&\gamma_c(\psi) = \frac{3e^{-uL}}{-2\alpha l_t^3 sinh[\alpha(L+2z_0)]} \frac{1}{(u^2+\eta^2-\alpha^2)^2 + (2\alpha\eta)^2} \times \\
&[2(-u^2-\eta^2-\alpha^2)cosh(2\alpha z_0)cos(L\eta) + 4\alpha\eta sinh(2\alpha z_0)sin(L\eta) \\
&+ 2(u^2+\eta^2-\alpha^2)cos(L\eta) - 2\frac{\alpha}{u}(\alpha^2-u^2+\eta^2)sinh[\alpha(L+2z_0)]sinh(uL) \\
&+ 2(\alpha^2-u^2-\eta^2)cosh[2\alpha(L+2z_0)]cos(uL) - 4\alpha u sinh(\alpha L)sinh(uL) \\
&+ 2(\alpha^2+u^2+\eta^2)cosh(\alpha L)cosh(uL)]
\end{aligned} \tag{4.17}$$

where $\psi$ is the scattering angle and the $\eta, \mu, \alpha$ parameters are defined as:

$$\eta = k(1-\mu_s) = \frac{\omega}{c_0}(1 - cos\psi) \tag{4.18}$$

$$u = \frac{1}{2}\kappa_{ext}(1 + \frac{1}{\mu_s}) \tag{4.19}$$

$$\alpha = \sqrt{\left(\frac{1}{L_a^2} + \frac{\omega^2}{c_0^2} sin^2\psi\right)} \tag{4.20}$$

being $k = \frac{2\pi}{\lambda} = \frac{\omega}{c_0}$ the light wave vector and $\mu_s = cos\psi$ the backscattering angle parameter. Meanwhile, $z_0 = al_t$ is the extrapolation length accounting for internal reflections at the boundaries ( $z = 0, L$ ). Whereas, L is the sample thickness, $\kappa_{ext} = \frac{1}{l_s} + \frac{1}{l_i}$ is an effective extinction coefficient accounting for the attenuation of scattered intensity and $\alpha$ is the diffusive extinction coefficient. For $L \to \infty$ the coherent coefficient is reduced to the following expression, valid for semi-infinite slabs (Akkermans model).

$$\gamma_c(\psi) = \frac{3}{2l^3\alpha u} \frac{\alpha + u(1 - e^{-2\alpha z_0})}{(u+\alpha)^2 + \eta^2} \tag{4.21}$$

Eq. 4.17 provides the interference coefficient calculated in the diffusion approximations. Along with the coherent bistatic coefficient $\gamma_c$, also the diffusive background coefficient $\gamma_l$ depends on the sample thickness L and from $z_0$,$u$ and $\alpha$ values. It also depends on a new parameter $\nu = \frac{1}{2}\kappa_{ext_D}\left(1 - \frac{1}{\mu_s}\right)$ expressed as a function of the diffusive extinction coefficient $\kappa_{ext_D} = \frac{1}{l_t} + \frac{1}{l_i}$. A similar function can be obtained for $\gamma_l$ whose mathematical form is not reported for simplicity.
Therefore, CBS is observed for light that is weakly localized within disordered media. The cone shape provides information either on the scattering strength and path distribution of light inside the material. Furthermore, CBS measurements can be exploited for many non-invasive biomedical techniques, as for optical coherence tomography. Indeed such techniques are based on light interaction with the scatters inside the biological tissue allowing to reconstruct specific information. The understanding of the CBS principles is fundamental to gain control of light transport within a medium in that can be eventually focused or guided for specific applications in optical microscopy and photonics.

## 4.3 Coherent backscattering in silicon nanowires

Light transport has been studied for two different Si nanowires arrays realized by metal assisted chemical etching using either thin percolative Au layers (2 nm) [62, 61] and silver salts ($AgNO_3$ 0.05 M) precursor [170, 171]. Both plan and cross-view SEM characterization of NWs are displayed in fig. 4.5 (a-d) for Au and $AgNO_3$-synthesized nanowires, respectively. A comparison between the two samples shows that NW planar arrangement and structural morphology are quite different. Si NWs realized by using percolative Au layers are fractals and made of a dense distribution of thin nanowires having mean diameter of 7 nm and length of 2.6 $\mu m$ (fig. 4.5 (a-b)). Whereas NWs fabricated by MACE using silver salts precursor (fig. 4.5 (c-d)) are still randomly distributed but do not possess a fractal geometry. The latter NWs have bigger diameter ranging from 50 up to 80 nm, length of 8 $\mu m$ and a lower NW density compared to the previous sample. The high resolution inset demonstrates that the NWs tips agglomeration is induced in $AgNO_3$-NWs by superficial effects that are dominant for longer and bigger wires. In either cases, the SEM characterizations show the fabrication of randomly distributed NWs possessing a different kind of disorder. The multiple scattering behavior of Si NWs has been recently reported in literature by many groups and the following sections exploit our investigation of the CBS measurements performed on strongly diffusing Si NWs [172].

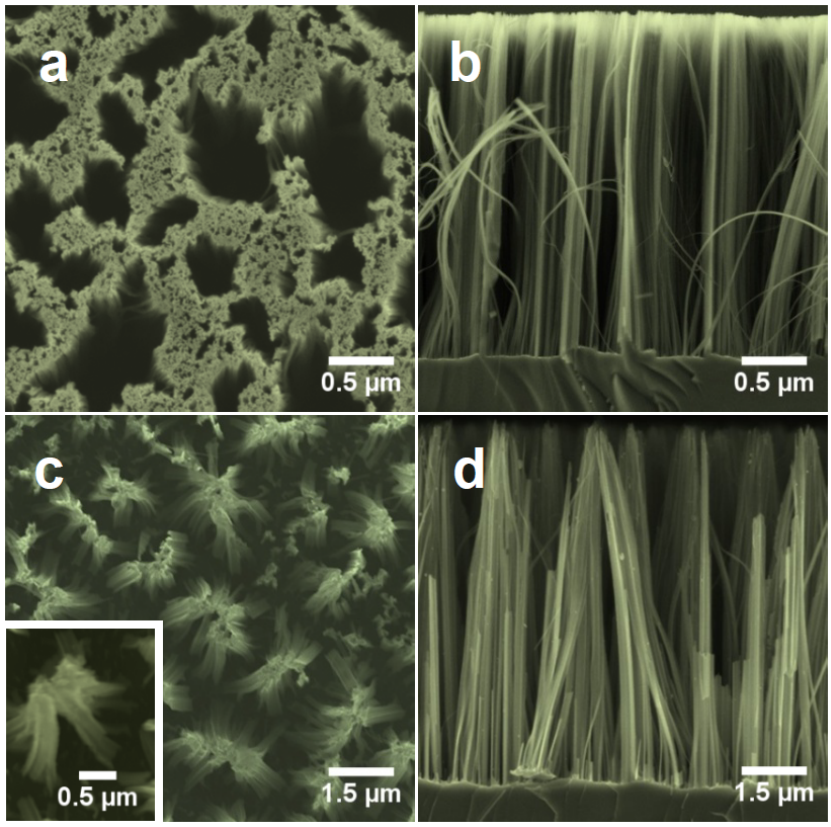


*Figure 4.5: SEM plan-view and cross-section reported for (a,b) Au- and (c,d) $AgNO_3$-fabricated Si NW arrays, respectively. The inset reports a high resolution detail of the $AgNO_3$-synthesized plan view (c) [172].*

### 4.3.1 Rayleigh backscattering measurements

The scattering strength of either fractal and non-fractal Si NWs have been studied by measuring the Rayleigh scattered intensity as a function of the collection angles ($\psi$) by using the scatterometer depicted in fig. 4.6. The samples have been positioned in the center of a three-axis rotation stage and excited with a focused laser beam in the desired polarization channel and both linear and circular polarization can be analyzed. The scattered light is then collected through an achromatic doublet lens mounted in the collection arm ( highlighted in yellow) and then focused on the core of a multi-mode optical fiber ($d = 550\ \mu m$).

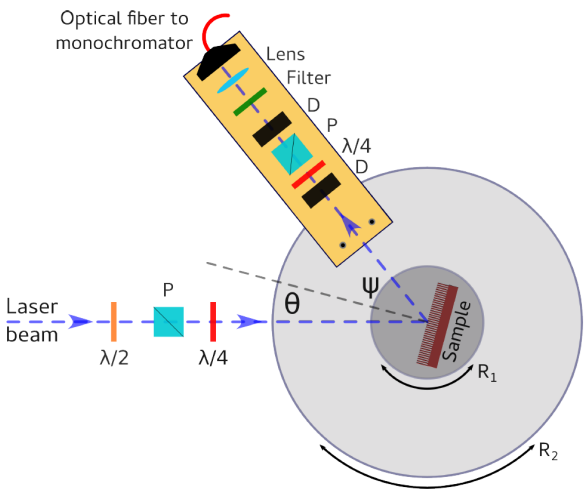


*Figure 4.6: Sketch of the scatterometer used for the CBS measurements having rotation angles $\theta$ and $\psi$. A polarizer P, $\lambda/4$ and $\lambda/2$ quarter and half waveplate have been used as polarization selector, while the angle resolution is defined by the diaphragm D. The collection arm (R2) and the sample holder (R1) are mounted on two independent rotation stages.*

The output signal is analyzed through a monochromator and coupled to a $N_2$-cooled CCD. The angular resolution can be selected by varying the aperture of one or more diaphragms (D) mounted before the lens and low resolution limits as good as 0.1° can be achieved without significant intensity losses. The collection arm is also equipped with a polarization selection system in order to discriminate the desired polarization channel. All the presented measurements were acquired at a normal incidence condition for $\theta = 0°$.

Figure 4.7 shows the scattering intensity measured by exciting the system with 532 nm line of an solid state laser. The circular polarization (helicity) conserving channel (blue dots) is compared with the diffusive background obtained from the linear non conserving channel (red dots) averaged between s and p polarizations respectively perpendicular and parallel to the plane of incidence. The diffuse background has been recorded according to the approach introduced by Muskens and Lagendijk by considering the linear non conserving polarization channel instead of considering standard lightly scattering media possessing very long transport mean free path (i.e. teflon) [163].

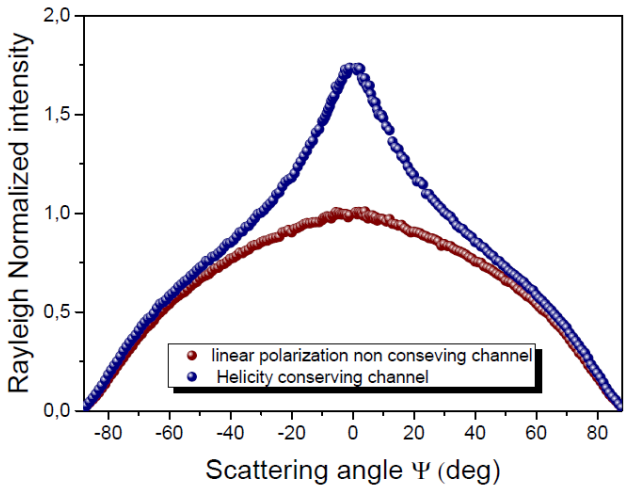


*Figure 4.7: Rayleigh scattering intensity angular profile reported for circular polarization conserving channel (blue dots) and linear non conserving channel averaged between s and p polarization (red dots) for Au-synthesized NW array of 2.6 μm length. The measurements have been performed by exciting at the 532 nm excitation line of a solid state laser.*

In fact their approach consents to exclude any influence due to the interface effects (air-sample) that could alter the diffusive response which is sensitive to both refractive index contrast and surface quality. Thus, by measuring the non conserving signal a better estimation of the diffuse background is obtained as demonstrated by the superposition of the two curves for high detection angles ($|\psi| > 60°$). On the other hand, the scattered intensity in proximity of the backscattering direction ($|\psi| \sim 0°$) is dramatically different. Indeed the diffusive contribution presents a cosine trend while the backscattered intensity is enhanced and a cone arises for the helicity conserving channel. In order to better highlight the enhancement profile of the backscattering cone the helicity conserving channel signal has been normalized to the diffusive background as plotted in fig 4.8.

The CBE measurements were acquired at an angle step of 1° by pumping the system at 532 nm and are displayed for Au-synthesized and Ag-synthesize NWs in fig. 4.8 (a) and (b), respectively. Both samples show the typical CBE profile due to the multiple scattering of light in disordered media.

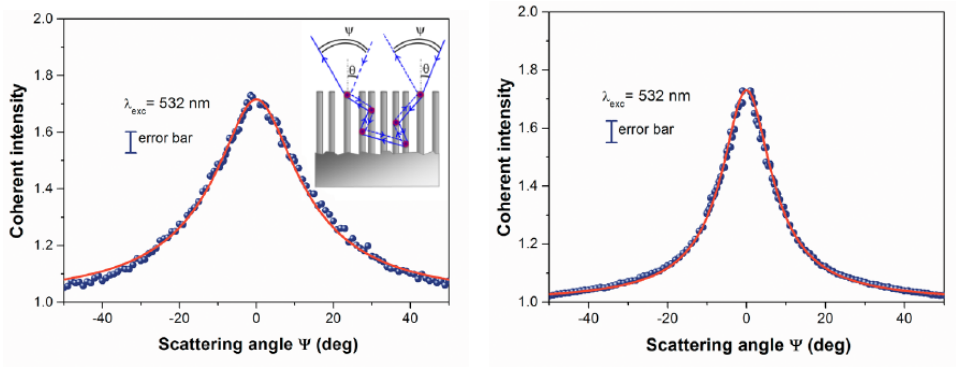


(a) (b)

*Figure 4.8: Rayleigh Coherent backscattering cones after the normalization to the diffusive background signals are plotted in blue dots for (a) Au- and (b) $AgNO_3$-synthesized Si NWs, respectively. The red continuous lines correspond to the respective fits obtained by the finite slab model (eq. 4.16). The inset in (a) schematically illustrates the coherent backscattering phenomenon [172].*

On the other hand, the cone profile is dramatically modified for the Ag-synthesized NWs (fig. 4.8 (b) ) showing a smaller cone angular width as well as a less pronounced cone tip rounding effect in comparison with the fractal NWs sample. Such differences can be ascribed to the different sample morphologies. Indeed the more dense and disordered the system the higher is its scattering strength that is defined as $S \sim \frac{1}{kl_t}$. In particular, lower surface coverage generally lead to lower scattering strength and higher mean free path, resulting in a more squeezed cone as for Ag-synthesized NWs.
Light transport in these NW arrays is highly anisotropic. Indeed, the transport mean free path $l_z$ in the vertical direction is thus much larger than transport path along the xy plane ($l_z \gg l_x, l_y$) due to NWs vertical orientation. The CBS angular profile and shape provide information on both the scattering strength and the path length distribution of light within the sample. The angular width of the CBS cone ($FWHM_\psi \sim 1/l_t$ ) is related to the transport mean free paths $l_t = l_x = l_y$. Whereas, the scattering along the z-direction can be studied as a function of the optical thickness of the sample $\frac{L}{l_z}$. However, the precise value of $l_z$ is generally hard to estimate espe-

cially in Si NWs where the sample roughness induces the coupling of the z-scattering to the one occurring along the xy plane [172]. In order to quantify the effective sample thickness and the transport path, the CBE data in fig. 4.8 have been fitted according to the finite-slab model for the CBS intensity. The transport mean free path has been considered the same along the xy plane ($l_t \equiv l_x = l_y$) and an effective optical thickness has been defined as $L_{eff}/l_t = L/l_z$, being $L_{eff}$ the effective thickness considered as a free fitting parameter. This way, $L_{eff}$ accounts for the contribution of the optical mean free path along the z-direction. The $L_{eff}$ and $l_t$ fit parameters strongly influence the shape of the backscattering cone. A characteristic inelastic (absorption) mean free path $l_i$ has also been included in the fit function as a fixed parameter, which was independently evaluated for the two samples from the effective Si fraction in the NW layer determined from structural analysis. Sample thickness of $L_{Au} = 2.6\mu m$ and $L_{Ag} = 8\mu m$ have been assumed as fixed fit parameters, as measured by the cross-section SEM microscopies. Also the air/sample interface effects have been considered by introducing an extrapolation length $z_0 = a \cdot l_t$ with values of $z_0^{Au} = 1.5 l_t\ \mu m$ and $z_0^{Ag} = 2.3 l_t\ \mu m$ for the two samples, respectively ( eq. 4.17). The CBE fitted by using the finite slab model (eq. 4.16) are plotted with red solid lines in fig. 4.8, leading to estimation of very small transport mean free paths $l_t = 170$ nm and $l_t = 483$ nm and an effective optical thickness $\frac{L_eff}{l_t} = 17$ and $\frac{L_eff}{l_t} = 5$ for Au and $AgNO_3$-fabricated NWs, respectively. These relatively large values of the effective optical thickness point towards a strong effective scattering in the $\overrightarrow{z}$ direction, despite the strong anisotropy of the NWs material. Both CBE profiles show the rounding of the cone tip, partially related to the angular resolution limit which is geometrically limited for $\psi \sim 0$ and to the medium absorption that is not negligible in the visible range. Indeed, the absorption as well as the sample finite size play a fundamental role by limiting the optical paths integration to those paths satisfying the condition $L < l_i$.

## 4.4 Raman coherent backscattering in silicon nanowires

The remarkable results obtained from the Rayleigh CBS in Si NWs demonstrate their promising scattering potential. However, the fascinating Raman effects observed for such NW arrays stimulated our curiosity and the presence of weak localization by coherent backscattering of Raman photons has also been tested. As well known, Rayleigh scattering is a coherent process. Therefore the scattered radiation has a definite phase relation with respect to the incoming wave.
Spontaneous Raman scattering is a linear effect ($I_{Raman} \propto I_{in}$) produced from the inelastic scattered light that has been perturbed by the interaction with the nuclear or electronic modes of the material having arbitrary phases. The experimental observation of Raman effect is generally incoherent since the phonon coherence is quickly lost over short coherence time and length [173]. However the pump wave, the Stokes/Anti-Stokes waves and the lattice vibrations are "phase locked" with each other [174]. This way, the frequency and phase of the phonons populating the vibration mode are equal to the beating frequency and phase of the overlapping laser and Raman local fields. Therefore, the phase coherence in multiple scattering media is still preserved on the scale of the phonon coherence length of about a few tens of nanometers and the Raman coherence is quickly lost with relaxation time of a few picoseconds in Si.
The observation of coherent backscattering of Raman light (RCBS) in Si NWs allows to macroscopically probe the coherent nature of spontaneous Raman scattering in disordered materials.

In the following section a brief explanation on Raman scattering is given in order to better understand the discussion on coherent Raman backscattering measurements.

### 4.4.1 A brief introduction to the Raman effect

An accurate description of the Raman effect can be obtained by treating both the system and the electromagnetic fields classically. The inelastic scattering of light is generated by the interaction with the oscillating electric dipoles of the material molecule induced by the electric field of the incoming radiation. The induced electric dipole

moment $\boldsymbol{\mu}$ of a molecule immersed in an electromagnetic field $\mathbf{E}$ is expressed as follows:

$$\boldsymbol{\mu} = \alpha\mathbf{E} + \frac{1}{2}\beta\mathbf{EE} + \frac{1}{6}\gamma\mathbf{EEE} + ... \tag{4.22}$$

where $\alpha$ is the polarizability, $\beta$ the hyperpolarizability and $\gamma$ the second hyperpolarizability of the molecule and so on. Higher-order terms lead to the observation of both coherent hyper- and 2nd hyper-Rayleigh and Raman scatterings, describing all the four-wave-mixing processes. The nonlinear terms are generally negligible for most materials and the discussion can be limited to the first term linear with $\mathbf{E}$, responsible for the Rayleigh and Raman scattering:

$$\boldsymbol{\mu} = \alpha\mathbf{E} \tag{4.23}$$

The polarizability tensor $\alpha$ is a function of the nuclei positions and accounts for the molecule vibrational state. The polarizability can be regarded as a measure of the flexibility of deformation the molecule electron cloud producing an induced electric dipole under the influence of the applied external field.
The $\alpha$ dependency on the nuclei coordinates is obtained for small oscillation by expanding the tensor components $\alpha_{ij}$ in Taylor series with respect to the equilibrium conditions $(\alpha_{ij})_0$:

$$\alpha_{ij} = (\alpha_{ij})_0 + \sum_k \left(\frac{\partial\alpha_{ij}}{\partial q_k}\right)_0 q_k + \frac{1}{2}\sum_{k,l}\left(\frac{\partial^2\alpha_{ij}}{\partial q_k \partial q_l}\right)_0 q_k q_l + ... \tag{4.24}$$

where the sum is performed all over the possible $k$th vibration modes having normal coordinate components $\mathrm{q}_k$. To further simplify the treatment, the dependence of polarizability on each vibrational coordinate is assumed linear for small amplitude oscillation from the equilibrium:

$$\alpha_k = \alpha_0 + \left(\frac{\partial\alpha}{\partial q_k}\right)_0 q_k \tag{4.25}$$

The normal vibrations can be treated as harmonic oscillations $q_k = q_{k0}cos(\omega_k t)$, being $q_{k0}$ and $\omega_k$ the amplitude and the frequency associated to the $k$th vibration, respectively. By substituting $q_k$ and the

monochromatic incident electromagnetic field $\mathbf{E} = \mathbf{E}_0 cos(\omega_0 t)$ into eq. 4.23, the following relation is obtained for the $k$th vibration:

$$\boldsymbol{\mu} = \alpha_0 \mathbf{E}_0 cos(\omega_0 t) + \frac{1}{2}\left(\frac{\partial \alpha}{\partial q_k}\right)_0 q_{k0} \mathbf{E}_0 cos(\omega_0 t) cos(\omega_k t) \tag{4.26}$$

leading to the appearance of three scattering terms by using trigonometric transformations:

$$\begin{aligned} \boldsymbol{\mu} = \underbrace{\alpha_0 \mathbf{E}_0 cos(\omega_0 t)}_{Rayleigh} + \underbrace{\frac{1}{2}\left(\frac{\partial \alpha}{\partial q_k}\right)_0 q_{k0} \mathbf{E}_0 cos[(\omega_0 - \omega_k)t]}_{Stokes} \\ + \underbrace{\frac{1}{2}\left(\frac{\partial \alpha}{\partial q_k}\right)_0 q_{k0} \mathbf{E}_0 cos[(\omega_0 + \omega_k)t]}_{Anti-Stokes} \end{aligned} \tag{4.27}$$

The first term in equation 4.27 refers to the Rayleigh scattered light occurring at the same frequency $\omega_0$ of the incident radiation. Raman scattering introduces new shifted lines in the spectrum of the scattered light, positioned symmetrically with respect to the Rayleigh line at $\omega_0 - \omega_k$ (Stokes lines) and $\omega_0 + \omega_k$ (Anti-Stokes lines), being $\omega_k$ the frequency associated to the rotational or vibrational transition [175]..

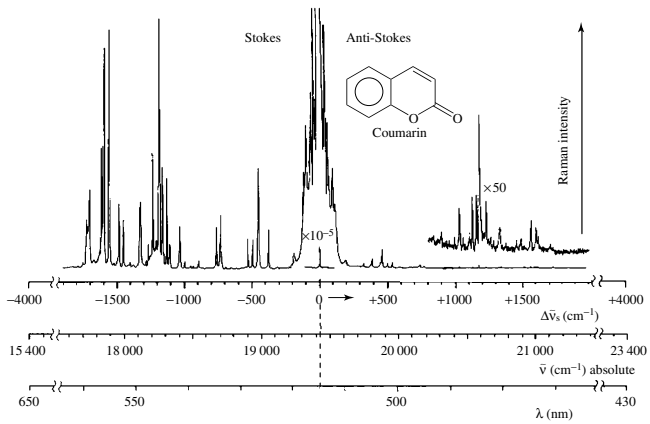


*Figure 4.9: Typical coumarin powder Raman spectrum showing the Rayleigh line and the symmetric Stokes and Anti-Stokes Raman lines respectively [175].*

A typical spectrum of the coumarin organic molecule is shown in fig. 4.9. As evident, the intensities of Anti-Stokes lines are considerably weaker than the correposnding Stokes ones [175]. Moreover, the intensities of Raman signals are about $10^{-5}-10^{-3}$ Rayleigh intensity, which is about $10^{-4}-10^{-3}$ the intensity of the incident exciting radiation [175].
The classical description correctly accounts for the appearance of discrete vibration peaks at different wavelengths with respect to the incoming radiation. It also demonstrates the occurrence of the Raman scattering independently from the frequency of the incident radiation and the Raman intensity dependence on the polarization of the incoming field.
However, the classical approach does not explain the intensity difference between the Stokes and Anti-Stokes lines without clarifying the transitions involved in the processes. In order to fully exploit the light-matter scattering interaction a quasi-quantum mechanical model is needed. The molecule is treated from a quantum point of view, while the incoming radiation is still considered as a classical electromagnetic wave perturbing the system.
According to quantum mechanics, the energy associated with electronic, vibrational and rotational degrees of freedom of a molecule can only assume a discrete set of values corresponding to the stationary states of the molecule $|i\rangle$. As shown in fig. 4.10, the electronic ($S_i$ bands) and discrete vibration energy levels (thin lines $v_i$) are distinguished. The minimum of the electronic band $S_0$ corresponds to the atom equilibrium position. The quantum description of Raman effect is obtained considering the electric dipole transition from an initial state $|i\rangle$ to the final state $|f\rangle$ of the molecule induced by the incoming electric field: $P_{if} = \langle i|\hat{P}|f\rangle$. The first-order perturbation term $P^1_{fi}$ obtained from time-dependent perturbation theory accounts for linear Rayleigh and Raman scattering, respectively:

$$P^1_{fi} = \langle \phi^0_f|\hat{P}|\phi^1_i\rangle + \langle \phi^1_f|\hat{P}|\phi^0_i\rangle \tag{4.28}$$

obtained from the calculation of the perturbed ($\phi^1$) and unperturbed ($\phi^0$) wavefunctions of the system. Both Rayleigh and Raman scatterings can be described by virtual states transitions.

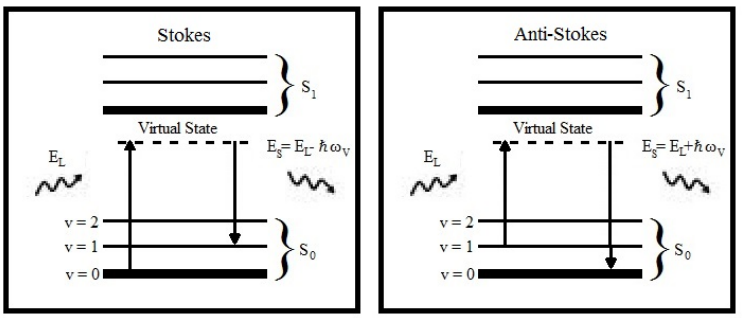


*Figure 4.10: Jablonski diagrams depicting the Stokes and Anti-Stokes frequency shifts associated with Raman scattering [176].*

Virtual states are not eigenstates for the molecule and are of practical convenience to describe the energy exchange between the radiation field and the molecule. As shown in fig. 4.10, the Stokes scattering involves a transition from a lower vibrational state $v = 0$ to a virtual state having higher energy. The system then relaxes to an higher energy vibrational state $v = 1$ of the molecule with respect to $v = 0$ and a scattered photon with smaller energy than the exciting one is produced. On the contrary, the Anti-Stokes scattering occurs from an excited vibrational state $v = 1$ that relaxes to the ground state $v = 0$ through a virtual state transition, leading to a scattered photon with higher energy than the incoming one. The intensity difference among the two Raman signal is related to the relative populations of the highest occupied vibration energy states, favoring the Stokes process over Anti-Stokes. The Stokes/Anti-Stokes intensity ratio increases with temperature that promote the population of the unoccupied excited vibrational states for a larger fraction of molecules.
The quantum mechanical model of Raman scattering describes the Stokes/Anti-Stokes intensity ratio by considering the phonon population per energy level according to Bose-Einstein statistic:

$$\frac{I_{Stokes}}{I_{Anti-Stokes}} = \frac{I_{\omega_0-\omega_k}}{I_{\omega_0+\omega_k}} = \frac{(\omega_0-\omega_k)^4}{(\omega_0+\omega_k)^4} exp\left(\frac{\hbar\omega_k}{kT}\right) \tag{4.29}$$

where $k$ is the Boltzmann constant. Equation 4.29 provides the relationship among the Raman intensity ratio and the proper temperature of the system (T) [175].

Raman spectroscopy is a non-invasive useful tool to obtain the molecular composition of either liquid or solid state systems by exciting the typical vibration transitions through the scattering processes. The focused enhancement of the Raman signal has opened a new route for sensing devices, as further discussed in chapter 5.

### 4.4.2 Raman coherent backscattering measurements

The observation of a strongly enhanced first-order Raman signal in Si NWs suggested that fascinating optical effects can also be obtained from the multiple scattering of Raman light. Indeed, as demonstrated below, we have observed for the first time an unexpected coherent backscattering of the Raman light (RCBS) [172].
This phenomenon observed for inelastic scattering is in strict analog with the elastic (Rayleigh) coherent backscattering described in the previous paragraph.

#### Theoretical description

The physical mechanism underlying the observation of a RCBS is rather complex. Spontaneous Raman scattering usually manifest as a spatial incoherent process. Therefore, no coherent superposition of Raman photons is generally observed even in the backscattering direction for lengths and time scales higher than the phonon coherence ones. However, Raman scattering still preserves fixed phase relations with respect to the incoming radiation and some works recently demonstrated either the spatial and temporal coherence of spontaneous Raman by near-field [173] and transient coherent ultrafast phonon spectroscopy [177], respectively. A simple interpretation for the observation of Raman coherent backscattering can be given by considering Rayleigh-Raman hybrid scattering paths [172], as depicted in fig. 4.11. Let's assume that an arbitrary scattering path P-S starts as a Rayleigh wave $(\overrightarrow{k_i}, \omega_i)$ scattered at the $r_1$ position (black halo) and then undergoes to a Raman scattering event at the $r_i$ position (red halo). The Raman wave is then scattered multiple times and is eventually expelled from the sample at the $r_n$ position as a Raman wave $(\overrightarrow{k_s}, \omega_s)$.

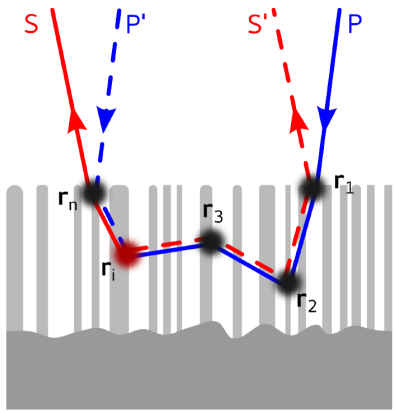


*Figure 4.11: Schematic illustration for the hybrid Rayleigh-Raman scattering interpretation supporting the observation of coherent Raman backscattering.*

According to the reciprocity theorem, for any of these hybrid Rayleigh-Raman scattering path there exists a reciprocal path P'-S' (dashed lines) for which a Rayleigh wave $(\overrightarrow{k_i'}, \omega_i')$ is scattered from the sample at $r_n$, giving origin to a Raman event at the same coordinate $r_i$ and finally outcome from the sample as a Raman wave $(\overrightarrow{k_s'}, \omega_s')$ from the point $r_1$. Within the coherence time the same phonon mode is available for both reciprocal paths and the two Raman scattering events occur at the same position $r_i$. A frequency shift $\omega_s - \omega_i$ is obtained per each hybrid path due to the annihilation/creation of a phonon.
The hybrid Rayleigh-Raman scattering path distribution can then be considered as a random walk for the Raman scattered light. For each hybrid path there exists a reverse hybrid path obtained by reversing the propagation direction $(\overrightarrow{k_s'} = -\overrightarrow{k_i}, \overrightarrow{k_i'} = -\overrightarrow{k_s})$ and trading the Rayleigh-Raman random walks. The scattering cross-sections corresponding to the two reciprocal hybrid processes are:

$$\sigma_D \propto |\widehat{e_i} R(\omega_i, \omega_s) \widehat{e_s}|^2 \tag{4.30}$$

$$\sigma_R \propto |\widehat{e_s} R(\omega_i, \omega_s) \widehat{e_i}|^2 \tag{4.31}$$

being $\widehat{e_i}, \widehat{e_s}$ the polarization versors and $\mathbf{R}(\omega_i, \omega_s)$ the two-rank Raman tensor.

The reciprocal hybrid waves accumulate a random phase difference within their path, making the direct and reverse Raman waves mutually incoherent. Such dephasing mechanism is related to the Raman scattering position along the path and therefore is more pronounced for longer paths. In general their polarization is also not preserved due to the occurrence of an inelastic scattering event at the position $r_i$. However, when the Stokes shift is small compared to the Rayleigh wavelength then both polarization and phase coherence between the hybrid paths are preserved. Indeed, the same phonon mode ($\omega_q$, $\overrightarrow{q} = \overrightarrow{k_i} - \overrightarrow{k_s}$) is equally available for both scattering paths when the incoming photon is backscattered at frequencies that are not that different from each other ($\omega_i \sim \omega_s$, or equivalently $|\overrightarrow{k_i}| = |\overrightarrow{k_s}|$). For such condition the Raman tensor $\mathbf{R}(\omega_i, \omega_s)$ is symmetric with respect to the exchange of the polarization versors $\widehat{e_i}, \widehat{e_s}$ leading to the exact same probability of the occurrence for the reciprocal paths ($\sigma_D = \sigma_R$). The Raman tensor symmetry is demonstrated for those crystals having inversion symmetry, and in particular for silicon [178, 179]. This way the path reciprocity is restored enabling the coherent superposition of the outgoing backscattered Raman fields. The $\omega_i \sim \omega_s$ condition washes out the random phase jump introduced by the creation/annihilation of a phonon when considering the phase difference between reciprocal paths, which is valid when the dwell time for the two reciprocal paths is much shorter than the phonon coherence time [180, 181]. The short transport mean free path and the strong Si NW absorption lead to the estimation of a dwell time of the order of a few femtoseconds for an average total scattering path of a few microns, far below the Si phonon coherence time in crystalline silicon ($\sim$ 1 ps).

Therefore, Si NWs multiple Raman scattering can be described by hybrid Rayleigh-Raman scattering paths assuming that the reciprocity and the coherence with the pump beam is preserved [172]. The Raman-enhanced backscattering is due to the interference of the Raman waves coherently generated in multiple scattering processes. The small frequency difference between Raman and Rayleigh waves accumulated along the hybrid path introduces a dephasing term $\Delta\phi$. A phase difference $\Delta\varphi = \frac{\omega_n - \omega'_n}{c}|r_n - r_{n+1}|$ is developed among the reciprocal paths between each scattering step, where c is the speed of light.

The total dephasing $\Delta\phi$ among reciprocal path is given by summing each phase differences $\Delta\varphi_n$ accumulated along the n scattering events. The total dephasing can be expressed as:

$$\Delta\phi = |\sum_n \Delta\varphi_n| = |\sum_n \frac{\omega_n - \omega'_n}{c}|r_n - r_{n+1}|| \tag{4.32}$$

Therefore, the constructive interference in the backscattering direction is observed when the phase difference accumulated along the entire multiple scattering path between reciprocal hybrid paths P-S and P'-S' is well below $2\pi$. This dephasing mechanism in the coherent contribution of multiple Raman scattering affects the light diffusion probability across the disordered NW forest, altering the Raman coherent backscattering. In the presence of dephasing the diffusion probability of light wave is varied by a $\langle e^{i\Delta\phi(t)}\rangle$ factor, where $\Delta\phi(t)$ is the phase difference between reciprocal paths [158, 182]. This phase difference is a random variable whose average is generally a decaying function of time $\langle e^{i\Delta\phi(t)}\rangle = e^{-\frac{t}{\tau_d}}$. The cut-off time $\tau_d$ is associated to a cut-off length $L_d = \sqrt{D\tau_d}$ describing the loss of phase coherence. The evaluation of the $\langle e^{i\Delta\phi(t)}\rangle$ factor has been given according to the statistical description of coherent Raman backscattering in terms of hybrid Rayleigh-Raman reciprocal paths. This average phase factor can then be expressed as:

$$\langle e^{i\Delta\phi(t)}\rangle \sim e^{i\langle\Delta\phi\rangle - \frac{\langle\delta\Delta\phi^2\rangle}{2}} = e^{\frac{i3D\Delta kt}{2l_t}} e^{\frac{-3D\Delta k^2 t}{2}} = e^{i\frac{t}{\tau_{d1}}} e^{-\frac{t}{\tau_{d2}}} \tag{4.33}$$

where $D = \frac{cl_t}{3}$ is the light diffusion constant. This average phase factor is a complex function of a fast oscillating term $\tau_{d1} = \frac{2l_t}{3Dk\Delta k}$ derived from the $\langle\Delta\phi\rangle$ dephasing contribution and a slow exponentially decaying term $\tau_{d2} = \frac{2}{3Dk\Delta k^2}$ derived from the dephasing variance $\langle\delta\Delta\phi^2\rangle$. In order to account for the Raman dephasing two dependent characteristic dephasing lengths have been introduced:

$$l_{d1} = c\tau_{d1} = \frac{2}{\Delta k} \tag{4.34}$$

$$l_{d2} = c\tau_{d2} = \frac{2}{\Delta k^2 l_t} = \frac{l_{d1}^2}{2l_t} \tag{4.35}$$

Where $l_{d1}$ is a phase-matching length allowing the coherent superposition of reciprocal hybrid paths with both constructive and destructive interference contributions.

These constructive and destructive terms have a relative phase difference of about $2n\pi$ (in-phase paths) and $\frac{(2n+1)\pi}{2}$ (out-of-phase paths), respectively. In contrast, $l_{d2}$ sets a cut-off for long scattering paths whose Raman coherence is lost due to random fluctuations in the phase difference between hybrid paths.

In order to account for the dephasing, $l_{d1}$ and $l_{d2}$ have been included both in the extinction $\kappa_{ext}$ and diffusion $\alpha$ coefficients figuring in $\gamma_c$ (eq. 4.17) as follows:

$$\kappa_{ext} = \frac{1}{l_t} + \frac{1}{l_i} + i\frac{1}{l_{d1}} + \frac{1}{l_{d2}} \tag{4.36}$$

$$\alpha = \sqrt{\left(\frac{1}{L_a^2} + \frac{1}{L_{d1}^2} + \frac{1}{L_{d2}^2} + q_b^2\right)} \tag{4.37}$$

where two new diffusion lengths $L_{d1} = \sqrt{\frac{il_t l_{d1}}{3}}$ and $L_{d2} = \sqrt{\frac{l_t l_{d2}}{3}}$ have been defined, followed by the absorption length $L_a = \sqrt{\frac{l_t l_i}{3}}$ and the scattering vector $q_b = ksin\psi$. It is important to remark that the diffusive background coefficient $\gamma_l$ depends on the diffusive extinction coefficient $\kappa_{ext_D} = \frac{1}{l_t} + \frac{1}{l_i}$ that is dephasing independent. Both $\gamma_c$ and $\gamma_l$ account for the inelastic contribution (as discussed in par. 4.2) as a function of the inelastic mean free path ($l_i = c\tau_i$):

$$\gamma_l \propto \int_0^\infty dt \frac{1}{t^{\frac{3}{2}}} \left(1 - e^{-\frac{t}{\tau_t}}\right) e^{-\frac{t}{\tau_i}} \tag{4.38}$$

$$\gamma_c \propto \int_0^\infty dt \frac{1}{t^{\frac{3}{2}}} \left(1 - e^{-\frac{t}{\tau_t}}\right) e^{-\frac{t}{\tau_i}} e^{-\frac{3D\Delta k^2 t}{2}} e^{-\frac{(kl_t\psi)^2}{3\tau_t}} cos\left(\frac{3Dkt}{2l_t}\right) \tag{4.39}$$

The hybrid Rayleigh-Raman angular backscattering profile has been fitted by introducing a new fitting function generalized for the Raman coherent backscattering enhancement (CBE):

$$CBE(\psi) = 1 + \frac{(E_{exp} - 1)\gamma_c}{(E-1)\gamma_l} \tag{4.40}$$

where the $E_{exp}$ is the experimental enhancement factor obtained from the backscattering measurements that is always reduced compared to the predicted theoretical 2 value due to the single scattering and stray light contribution. The theoretical enhancement factor $E = \frac{\gamma_c + \gamma_l}{\gamma_l}$ is instead evaluated from the fit.

This expression for the fitting function has the great advantage to allow the estimation of the RCBS enhancement factor $E = E_{Raman}$ as a fitting parameter for the backscattering cone. Any spurious effects which may reduce the measured intensity is then excluded with this considerations. Equation 4.40 is a function of two new fitting parameters $l_{d1}$ and $l_{d2}$ that are included in the $\gamma_c$ term only. The dephasing mechanism affects the Raman backscattering cone profile by broadening its angular width and reducing the peak intensity compared to the Rayleigh cone. This latter equation can be adopted for both Raman and Rayleigh scattering by setting both dephasing lengths to infinite in the latter case.
In the exact backscattering direction ($\psi = 0$), the time integral of the diffused and coherent bistatic coefficients are easily expressed as a function of the scattering path lengths:

$$\gamma_l(\psi = 0) \propto \int_0^\infty dl \frac{1}{l^{\frac{3}{2}}} \left(1 - e^{-\frac{l}{l_t}}\right) e^{-\frac{l}{l_i}} \qquad (4.41)$$

$$\gamma_c(\psi = 0) \propto \int_0^\infty dl \frac{1}{l^{\frac{3}{2}}} \left(1 - e^{-\frac{l}{l_t}}\right) e^{-\frac{l}{l_i}} e^{-\frac{l}{l_{d2}}} cos\left(\frac{l}{l_{d1}}\right) \qquad (4.42)$$

Strongly scattering materials satisfy the $l_{d1} > l_t$ condition that implies $l_{d2} \gg l_{d1}$ and the coherence function ($\gamma_c$) is a damped cosine [172]. For $\psi = 0$, the enhancement factor $E = \frac{\gamma_c + \gamma_l}{\gamma_l}$ depends only on $l_i, l_t, l_{d1}$ and the related $l_{d2}$. The theoretical enhancement factor in the exact backscattering direction ($\psi = 0$) is equal to the 2-limit only for Rayleigh backscattering for which the condition $\frac{\gamma_c}{\gamma_l} = 1$ is satisfied. Whereas, $E = E_{Raman} < 2$ is always observed for Raman scattering since $\frac{\gamma_c}{\gamma_l} < 1$ in this case. Indeed, the dephasing affects only the coherent contribution to the bistatic coefficient $\gamma_c$. Unlike Rayleigh scattering, the Raman enhancement $E_{Raman}$ is strongly dependent on $l_{d1}$, whereas the $l_{d2}$ dependence is expected to be weaker since typically $l_{d2} \gg l_{d1}$ in our samples. Thus lower enhancement factors correspond to lower dephasing lengths. However, a direct relationship between $l_{d1}$ and $E_{Raman}$ involves the effect of the inelastic (absorption) mean free path $l_i$. The manifestation of Raman coherent backscattering in strongly scattering materials is indeed determined by the absorption of the system.

The reason for this counter-intuitive behavior is provided by coherence function governing the interference of multiply scattered Raman waves. Equation 4.42 proves that the coherence function $\gamma_c$ would rapidly converge to zero in the absence of optical absorption. The damped oscillations as a function of the scattering path length would suppress the coherent term with respect to the diffused (incoherent) one in absent of the absorption $l_i$. On the other hand, the absorption excludes the long scattering paths from the integration limit for both coherent and diffuse terms. This way the coherent term of the backscattered intensity enhancement can emerge over the diffuse one.

The absorption term is necessary for the observation of coherence effect in the multiple scattering of spontaneous Raman. Whereas the absence of absorption, would strongly increase the interaction length of the light with the matter, paving the way towards interesting nonlinear effects [183, 184].

## Experimental evidences

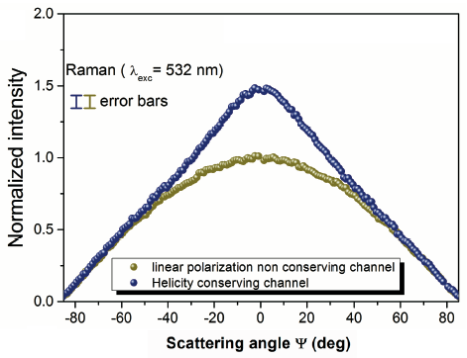


*Figure 4.12: Angular profile for the Raman scattering intensities are reported for the circular polarization conserving channel (blue dots) and the linear non conserving one averaged between s and p polarization (yellow dots) for Au-synthesized NW array of 2.6 $\mu m$ length. The measurements have been performed by exciting at the 532 nm excitation line of a solid state laser.*

Figure 4.12 reports the angular profile for the (blue dots) helicity conserving and (yellow dots) linear (s-p average) non conserving channel of Raman scattered light measured for a 2.6 $\mu m$ long array of Au-synthesized Si NWs. The displayed RCBS measurements have been obtained by exciting the system at the 532 nm line of a solid state laser for normal incidence angle ($\theta = 0°$). Two additional notch and long pass filters specific for the excitation wavelength were implemented in the collection arm (fig. 4.6) in order to exclude any elastic scattering and photoluminescence contributions to the RCBS measurements. A clear enhancement nearby the backscattering direction ($\psi = 0$) is also observed for the Raman helicity conserving channel. Whereas, a Lambertian diffusing behavior measured for the polarization non conserving channel. The RCBS measurements reported in fig. 4.12 demonstrates the macroscopic manifestation of coherent effects for Raman light in strongly scattering random Si NWs.

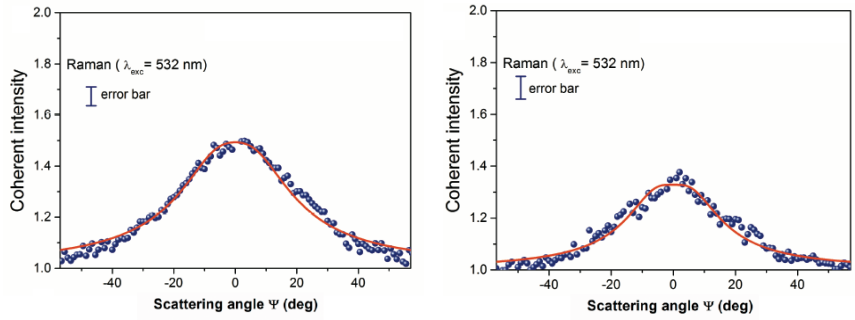


*Figure 4.13: Raman coherent backscattering cones after the normalization to the diffusive background signals are plotted in blue dots for (a) Au- and (b) $AgNO_3$-synthesized Si NWs, respectively. The red continuous lines correspond to the respective fitting functions reported in eq. 4.40.*

Figure 4.13 displays the coherent Raman backscattering enhancement (RCBE) obtained from the normalization to the diffusive background for (a) Au- and (b) Ag-synthesized NWs, respectively plotted as blue dots. Both data were fitted according to the hybrid Rayleigh-Raman backscattering model reported in eq. 4.40. The refractive index $n_{eff}$, the coefficient $a$ describing the internal reflection at the boundaries and the absorption mean free path $l_i$ have been set as fixed parameters for the RCBS fits. Also the transport mean free path ($l_t$) and the effective length ($L_{eff}$) obtained from the corresponding Rayleigh fit of the experimental CBS cones have been set as fixed fit parameters. Whereas, the Raman enhancement factor ($E_{Raman}$) and the dephasing length ($l_{d1}$) are now introduced as new fitting parameters (note that $l_{d2} = \frac{l_{d1}^2}{2l_t}$ is an evaluated parameter). The RCBS theoretical predictions very well fit the Raman enhancement experimental data when both dephasing and absorption terms are considered and the estimated coefficients are reported in table 4.1. It must be noted that $E_{Raman}$ is the theoretical enhancement factor evaluated from the fit according to eq.4.40, not to be confused with the experimental enhancement factor $E_{exp}$ shown in the backscattering measurements. Remarkably, both Si NW arrays present the typical coherent backscattering enhancement profile also for Raman light.

| $\lambda_{exc}$ = **532 nm** | | |
|---|---|---|
| Si NWs from | **Au-film** | **$AgNO_3$ salts** |
| $\mathbf{n_{eff}}$ | 1.36 ± 0.14 | 1.73 ±0.25 |
| **a** | 1.5 | 2.3 |
| $\mathbf{l_i}$ ($\mu$m) | 8.1 | 3.8 |
| **CBS fitting parameters** | | |
| $\mathbf{l_t}$ ($\mu$m) | 0.17 ± 0.02 | 0.48 ± 0.02 |
| $\mathbf{L_{eff}/l_t}$ | 17 ± 5 | 5 ± 0.2 |
| **RCBS fitting parameters** | | |
| $\mathbf{E_{Raman}}$ | 1.62 ± 0.08 | 1.28 ± 0.07 |
| $\mathbf{l_{d1}}$ ($\mu$m) | 3.4 ± 0.3 | 2 ± 0.4 |
| $\mathbf{l_{d2}}$ ($\mu$m) | 1.40 ± 0.14 | 1.36 ± 0.14 |

*Table 4.1: CBS and RCBS fitting parameters according to the hybrid Rayleigh-Raman model calculated from backscattering profiles of Au-synthesized Si NW array displayed in fig. 4.14.*

The main characteristic lengths responsible for the RBCS cones are different for the two samples (see table 4.1). The dephasing length $l_{d1}$ is characteristic of the same Raman mode and assumes similar values for the two cases. Indeed, the slight variation of this parameter is only related to the small difference in the refractive index of the two materials. In order to observe the Raman coherent backscattering the condition $l_{d1} > l_t$ must be verified. Figure 4.13(a) shows a more pronounced RCBS profile and a higher enhancement since $l_{d1}/l_t \gg 1$.Conversely, the ratio $l_{d1}/l_t$ is smaller for $AgNO_3$-fabricated NWs due both to the smaller dephasing length and a longer transport mean free path associated experimentally measured from the Rayleigh CBS. Such a smaller ratio makes the observation of phenomena more complex, resulting in a less pronounced RBCS cone.

To further investigate the role of dephasing and absorption in the hybrid Rayleigh-Raman backscattering mechanism both Rayleigh and Raman enhancements have been explored as a function of different laser wavelengths on the same array of Au-synthesized Si NWs. The angular enhancement profiles are reported as a function of the incident wavelength ((a) 488 nm, (b) 532 nm and (c) 785 nm) for both Rayleigh (blue dots) and Raman (yellow dots) backscattering (fig. 4.14).

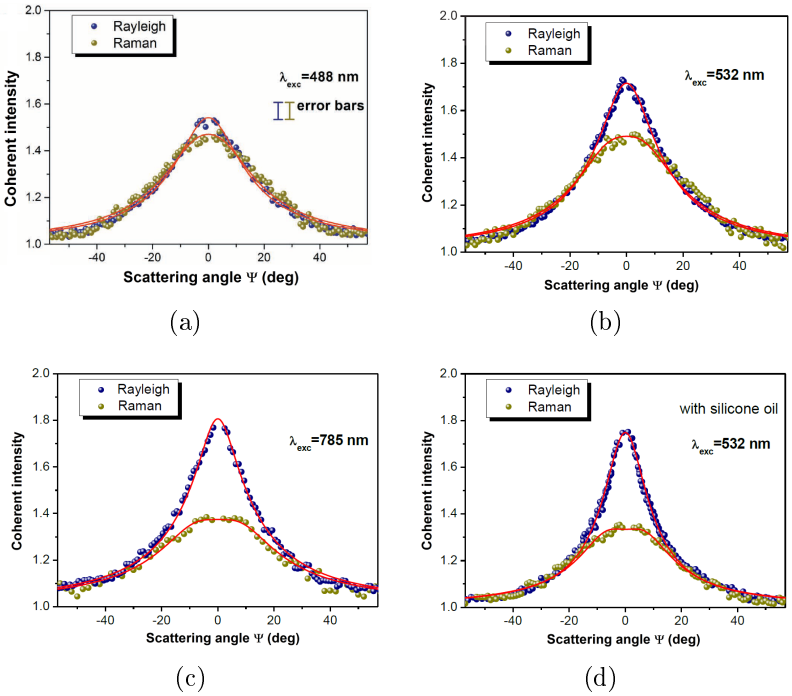


*Figure 4.14: Rayleigh (blue dots) and Raman (yellow dots) coherent backscattering cones measured in Au-synthesized Si NWs at different excitation wavelength: (a) 488 nm, (b) 532 nm and (c) 785 nm, while (d) is measured at the 532 nm excitation wavelength for the same sample infiltrated with silicone oil. The red solid lines are the fits obtained from the hybrid Rayleigh-Raman model (eq. 4.40) whose fitting parameters are reported in table 4.2.*

The experimental data have been fitted according to hybrid Rayleigh-Raman model (red solid lines) presented in the theoretical section (eq. 4.40). A quite good match is observed between the fits and experimental data at all the examined wavelengths for RCBS and CBS (by setting $l_{d1} = l_{d2} = \infty$), demonstrating the validity of the theoretical model in either cases. All the free fitting parameters have been measured from the CBS and RCBS cones displayed in fig. 4.14 and are resumed per each wavelength in the following table 4.2. It is worth to notice that $n_{eff}$, $a$ and $l_i$ were kept fixed, while $E_{Raman}$ is the theoretical Raman enhancement factor evaluated from the fit. The effect of the dephasing is clearly unveiled by comparing the Raman and Rayleigh enhancements.

| $\lambda_{exc}$ (nm) | 488 | 532 | 785 | 532 (oil) |
|---|---|---|---|---|
| **CBS and RCBS fixed parameters** | | | | |
| $\mathbf{n_{eff}}$ | 1.40 ± 0.14 | 1.36 ±0.14 | 1.32 ±0.13 | 1.72 ±0.17 |
| **a** | 1.6 | 1.5 | 1.4 | 2.3 |
| $\mathbf{l_i}$ ($\mu$m) | 4.8 | 8.1 | 86.5 | 8.1 |
| **CBS fitting parameters** | | | | |
| $\mathbf{l_t}$ ($\mu$m) | 0.15 ± 0.02 | 0.17 ±0.02 | 0.19 ±0.02 | 0.22 ±0.02 |
| $\mathbf{L_{eff}/l_t}$ | 18 ± 6 | 17 ±5 | 13 ±0.5 | 9 ±0.5 |
| **RCBS fitting parameters** | | | | |
| $\mathbf{E_{Raman}}$ | 1.75 ± 0.08 | 1.62 ±0.08 | 1.44 ±0.07 | 1.45 ±0.07 |
| $\mathbf{l_{d1}}$ ($\mu$m) | 3.9 ± 0.4 | 3.4 ±0.3 | 5.6 ±0.5 | 2.9 ±0.3 |
| $\mathbf{l_{d2}}$ ($\mu$m) | 50 ± 10 | 34 ±7 | 81 ±13 | 19 ±4 |

*Table 4.2: CBS and RCBS fitting parameters according to the hybrid Rayleigh-Raman model calculated from backscattering profiles of Au-synthesized Si NW array displayed in fig. 4.14.*

The Rayleigh enhancement is higher than the Raman one per each wavelength ($E_{Rayleigh} > E_{Raman}$), which is agreement with the theoretical prediction. The coherent coefficient $\gamma_c$ differs from the diffusive one $\gamma_l$ only for the presence of the damped cosine dephasing term: $e^{-\frac{l}{l_{d2}}} cos\left(\frac{l}{l_{d1}}\right)$. Thus in the presence of dephasing the Raman enhancement for $\psi = 0$ reduces to $E = \frac{\gamma_c+\gamma_l}{\gamma_l}$ accordingly to eq. 4.42, which is always smaller than two since $\gamma_c < \gamma_l$. Raman and Rayleigh cones (fig. 4.14) show the same trends for backscattering angles above $|\psi| \geq 20°$, attesting the robustness of the observation of Raman coherent backscattering in strongly scattering Si NWs.

The refractive index changes when the wavelength is varied, affecting both the absorption and the dephasing length $l_{d1}$ (see table 4.2). The Raman enhancement factor depends mutually on absorption and dephasing length. The absorption efficiency of Si NWs drastically decreases when moving towards wavelengths close to material energy bandgap, corresponding to an increment in material typical absorption length ($l_i$) from a few $\mu m$ up to a few tens of $\mu m$. When absorption decreases the coherent term is reduced due to the integration of the damped oscillating term over a wider integration region, as for fig. 4.14 (c) ($l_i = 86.5\mu m$). This occurrence reduces the Raman enhancement and also rounder and more flattened RCBS tips are observed.

Indeed, as absorption decreases a stronger difference is appreciated between Rayleigh and Raman cones. The highest absorption conditions is here displayed at 488 nm (fig. 4.14 (a)) where the CBS and RCBS show almost the same exact trend and the enhancement factors are slightly different. The higher Raman enhancement is observed at this wavelength ($E_{Raman} = 1.75$ as evaluated from the fit) where the strong material absorption prevents the dephasing term of $\gamma_c$ to be averaged to zero.

Finally, the attenuation of multiple scattering of light in presence of an index-matching medium has also been considered. The refractive index difference at the Si NW/air interface is reduced when silicon oil (refractive index 1.46) is infiltrated into the array. This way, the refractive index fluctuations are attenuated into the NW layer. The index-matching condition reduces the scattering strength of the system by increasing the mean free path for both elastic and inelastic scattered light. Figure 4.14 (d) compares Rayleigh (blue dots) and Raman (yellow dots) coherent backscattering enhancement cones for the same Au-synthesized Si NWs sample infiltrated with silicone oil. Indeed, the Rayleigh CBE squeezes in the presence of oil ($FWHM_\psi$ is reduced) due to a mean free path increment from 170 nm to about 220 nm. On the other hand, a variation is observed for the Raman cone width and the effect of oil introduction is the Raman enhancement factor reduction from $1.62 \pm 0.08$ to $1.45 \pm 0.07$. This reduction can be ascribed to the longer transport mean free paths and to the shorter dephasing length $l_{d1}^{oil} = 2.9 \pm 0.3\ \mu m$ that strongly affect the probability to observe the effect.

To better understand the interplay between the absorption and dephasing lengths on the RCBS enhancement factor the $E_{Raman}$ has been investigated as a function of the $l_i, l_{d1}$ normalized for the transport mean free paths $l_t$. Figure 4.15(a) shows the contour plot of the theoretical Raman enhancement expressed as a function of the normalized dephasing and absorption lengths (the highest enhancement is shown in yellow). This way, the Raman enhancement dependence have been reduced to only two parameters by normalizing for $l_t$.

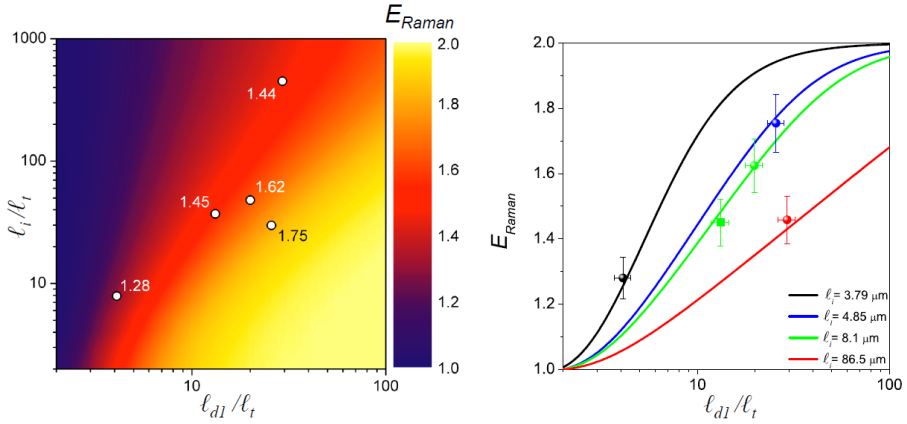


*Figure 4.15: (a) Color scaled contour plot of the theoretical coherent Raman enhancements (at $\psi = 0$) reported as a function of the dephasing length (x axis) and inelastic mean free path (y axis) expressed in units of transport mean free path and plotted in logarithmic scale. The experimental $E_{Raman}$ values obtained from the fit are shown with white dots. (b) Theoretical trends of coherent Raman enhancement plotted as a function of dephasing length in units of $l_t$ for different inelastic mean free paths. The solid dots and the error bars represent the experimental data for Au-synthesized Si NWs Raman enhancement factor measured at 488 (blue), 532 with (green square) and without oil (green dot) and 785 nm (blue), respectively), while $E_{Raman}$ for Ag-synthesized NWs excited at 532 nm is displayed as a black circle.*

When the dephasing length $l_{d1}$ is fixed, $E_{Raman}$ decreases by increasing the absorption length $l_i$. As shown in fig. 4.15(a), the Raman enhancement decreases from $1.75 \pm 0.08$ to $1.44 \pm 0.07$ when $\frac{l_i}{l_t}$ pass from 20 to 500 for a fixed value of $\frac{l_{d1}}{l_t} = 20$. The dependence of $E_{Raman}$ for a fixed absorption length $l_i$ is better visualized fig. 4.15(b), showing that $E_{Raman}$ has the opposite trend that what previously considered, increasing accordingly to the dephasing length $l_{d1}$ increment. Significant Raman enhancement factors are observed only when the condition $l_{d1} > l_i$ is satisfied, requiring absorption length of about a few microns for the typical vibrational frequencies in solid-state materials. This unusual behavior is determined by integral expression of the bistatic coherent coefficient (eq.4.42) given by

an oscillating term multiplied by the The coherent term is a damped cosine defined as a function of the scattering path length that rapidly average to zero in the absence of optical absorption suppressing the enhancement of the backscattered intensity with respect to the diffused one. Indeed, the presence of absorption leads to a cutoff of the integral at long scattering paths for both coherent and diffused contributions, allowing the observation of the coherent over the diffused background.

## 4.5 Conclusion

The diffusion of light in presence of multiple scattering has been described in this chapter according to the random walk approach. The fundamental aspects of coherent backscattering of elastic scattered (Rayleigh) light have been highlighted. This phenomenon is observed for highly scattering media and we demonstrated the occurrence of coherent backscattering for Si NWs having either a fractal and non-fractal arrangement. Indeed, coherent backscattering in NW arrays manifests due to the coherent superposition of reciprocal paths for multiple scattered light, leading to an enhancement factor for elastic backscattered light up to 1.8 for both fractal and non fractal Si NW arrays when measuring the helicity conserving channel. The coherent backscattering cone has been fitted according to the finite slab model and transport mean free paths as low as $l_t \sim 150$ nm have been calculated from the fits, attesting the strong scattering strength of our Si NWs. The coherent backscattering properties of Si NWs has been further tested for inelastic Raman scattering, demonstrating the first experimental evidence of coherent Raman backscattering. The Raman enhanced cone is due to the constructive interference in backscattering direction of Raman shifted waves that are coherently generated in a multiple scattering process. The occurrence of multiple Raman scattering within the Si NWs has been exploited by considering hybrid Rayleigh-Raman scattering paths for which reciprocity and the coherence between the pump beam and Raman scattered waves are preserved. A new model accounting for the dephasing mechanism has been adopted when hybrid scattering paths are considered, arising from the small frequency difference between Raman and Rayleigh waves. The Raman coherent backscattering enhancement has been investigated as a function of the excitation wavelength and compared to the Rayleigh case to show the differences among the two phenomena. Finally, the correlation among the fit parameters and the optical response of the system has been demonstrated. The possibility to control the transport of light within disordered media is extremely appealing and opens new frontiers for several applications in optics, photonics and photovoltaics. These results are of great interest, allowing for a better understanding of light management from multiple scattering in random disordered media.

# Chapter 5

# Surface-Enhanced Raman Spectroscopy sensors based on silicon nanowires


**Abstract**

*The high aspect ratio of Si NWs arrays has a great potential for many applications and in particular for Si-based sensors. For this purpose the huge NW surface-to-volume ratio has been coupled to plasmonic effects decorating the array with metal nanoparticles (NPs).*

*Si NWs have been synthesized by metal-assisted chemical etching (MACE) by using a silver salts bath and then decorated with silver nanoparticles (NPs) produced by pulsed laser deposition (PLD).*
*Both NW synthesis and decoration techniques are performed at room temperature with a low-cost and Si implementable technology.*
*Moreover, by using this approach Si NWs have been fully decorated along all their length without the need of any post-deposition annealing process. The great potentialities of PLD metal decoration of Si NWs for SERS applications are demonstrated.*
*SERS characterizations of Ag-decorated Si NWs are reported as a function of rhodamine 6G (R6G) molar concentration in aqueous solution, demonstrating a very low limit of detection down to* $10^{-8}$ *M. Furthermore, a SERS enhancement factor of* $10^8$ *has been estimated that is one order of magnitude higher with respect to a similarly decorated Si flat surface.*

## 5.1 Decoration of silicon nanowires with silver nanoparticles

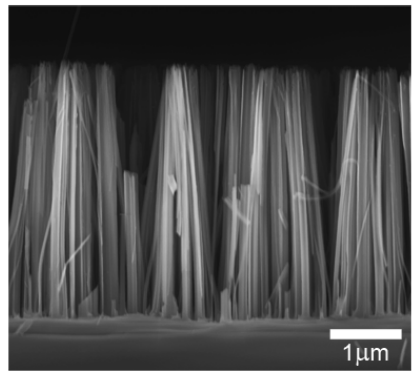


*Figure 5.1: Cross-section SEM microscopy of 3 µm long Si NW array.*

Silicon nanowires have been synthesized by metal assisted chemical etching by using a silver salts solution composed of 40% silver nitrate ($AgNO_3$ 0.05 M), 40% of deionized water and 20% of HF has been used [8]. This method has been already presented in chapter 1 and the evolution of the etching process is similar to the one occurring for Au film assisted MACE.
Si NWs synthesized by Ag salts precursor present a higher spacing among adjacent wires with respect to Au-fabricated ones, resulting in a better control over the nanoparticles decoration distribution. Figure 5.1 displays a SEM microscopy of vertically aligned, 3.4 $\mu m$ long Si NW array realized on a (100)-oriented, p-type silicon substrate by silver salts metal assisted chemical etching. Si NWs synthesized by Ag salts-MACE have bigger diameters, ranging from 30 up to 80 nm and do not emit light due to quantum confinement. Nevertheless, such NWs have the same doping of the starting Si wafer and do not present any metallic traces inside the wire. The structural properties of the array, in particular NW length, can be varied with great accuracy according to the etching conditions [42]. Two Si NW arrays having length of 1.7 $\mu m$ and 3.4 $\mu m$ have been realized by using an etching time of 11 min and 25 min, respectively [185].

The high aspect-ratio of Si NWs has been then combined with plasmonic effect by Ag nanoparticles (NPs) decoration in order to obtain high sensitivity surface enhanced Raman spectroscopy (SERS) substrates.

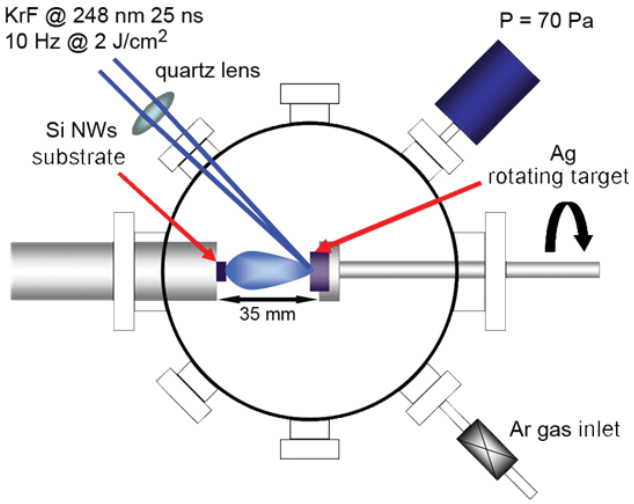


*Figure 5.2: Representative scheme of the pulsed laser deposition experimental setup used for Si NW decoration with Ag NPs.*

Si NW decoration with silver nanoparticles is realized by pulsed laser deposition (PLD), whose setup is represented in fig. 5.2.
During the decoration process a KrF excimer laser at the 248 nm laser line having a pulse width of 25 ns is focused through a quartz lens onto a pure silver target. In order to avoid excessive surface damaging the Ag target is kept on rotation by the rotating holder. Si NWs samples have been positioned at a distance of 35 mm from the Ag target and the deposition has been performed at room temperature in an Ar-rich atmosphere at the pressure of 0.7 mbar (70 Pa). The high energy laser beam impinges on the sample at a repetition rate of 10 Hz and a 2 $J/cm^2$ energy density. The laser vaporizes the material and a dense plasma plume containing Ag ions is produced [186, 187]. In the presence of the Ar environment the plasma undergoes to an isothermal expansion forming a shock wave propagating on the normal axis with respect to the target surface [188]. Under the considered gas pressure condition the in-flight agglomeration of

Ag NPs is favored at the plasma/gas interface [189]. The Ag NPs produced on-flight subsequently land onto the Si NW surface covering the whole wire length.
PLD is a very reliable physical deposition technique for nanostructures that is fully compatible with Si technology. Indeed, the Ag nanoparticles density and morphology can be easily controlled with high accuracy by optimizing the PLD process parameters [190]. Many chemical processes are also widely available for metal nanoparticles synthesis. Nevertheless, those processes generally require the aid of a chemical shell in order to avoid post-deposition clustering and stabilize the NP solution [191]. By contrast, PLD synthesized Ag NPs are free from any chemical capping shell. Therefore, the NPs can be chemically bonded to the NW substrate and further functionalized to selectively bind to target molecules only [77, 192]. The PLD decoration parameters have been optimized in order to fully decorate the NWs along all of their length, from the top to the base. Two different PLD deposition cycles of 45,000 and 60,000 laser pulses have been used on short ($1.7\mu m$) and long length ($3.4\mu m$) Si NW arrays in order to exploit the realization of different Ag NP morphologies and optical responses.
For clarity the 1.7 $\mu m$ short Si NWs decorated with 45,000 and 60,000 PLD pulses are from now on labeled as **sample 1** and **sample 2** respectively, while **sample 3** and **sample 4** correspond to the 3.4 $\mu m$ long ones decorated with 45,000 and 60,000 pulses, as resumed later in table 5.1. The chosen parameters are justified considering that the NP density and distribution vary by increasing the number of laser pulses, whereas different NW lengths determine a different planar arrangement. The Ag NPs dimensions and spacing are two crucial parameters that define the SERS performances.
Therefore, the morphology of decorated NWs have been deeply investigated by both SEM and TEM microscopy in order to characterize the Ag NP distribution along the wire length. Figure 5.3 shows a comparison among the SEM plan-views of (a) as-prepared and (b) Ag decorated NWs reported for sample 4. A higher resolution SEM image of a decorated wire section is reported in the inset of fig. 5.3(b), better showing the presence of Ag nanoparticles along all the wire surface.

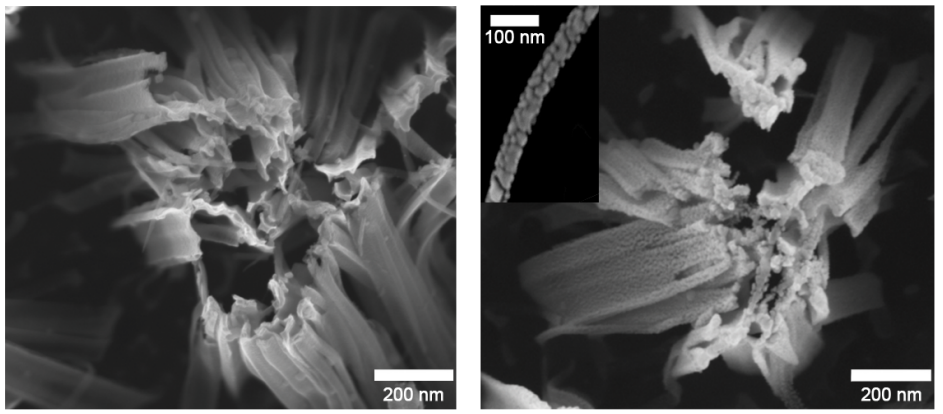


(a) (b)

*Figure 5.3: SEM plan-view characterization of silicon nanowires performed on sample 4 (3.4 μm long array) (a) before and (b) after Ag NP PLD decoration by using 60,000 laser pulses. The inset displays an SEM image of an Ag decorated wire segment.*

As visible from the figures, after the decoration the Si NWs surface is fully covered with a dense distribution of Ag NPs. Moreover, it can be observed that the PLD process does not cause any damage to the NW arrays. As a representative example, sample 1 SEM cross-section overview is reported in fig. 5.4(a), displaying that Si NWs are evenly covered from the top to the bottom with a dense and uniform distribution of narrowly spaced NPs.
Meanwhile, the higher resolution SEM cross-sections showing the top, central and bottom regions of sample 1 are reported in fig. 5.4 (b), (c) and (d) respectively. A first glance of fig. 5.4 reveals that the NP distribution is different along the wire length. In fact, the top section presents a dense amount of bigger Ag clusters. Whereas their density and dimension decrease towards the wire basement, where smaller and isolated NPs are clearly distinguished. Each sample has also been investigated by TEM in order to confirm the statistical results obtained from SEM measurements. Decorated Si NW have been scratched from the bulk substrate and transferred on a TEM grid for analysis. In fig. 5.4 (e) is reported a TEM microscopy corresponding to the bottom section of a decorated wire (sample 1).

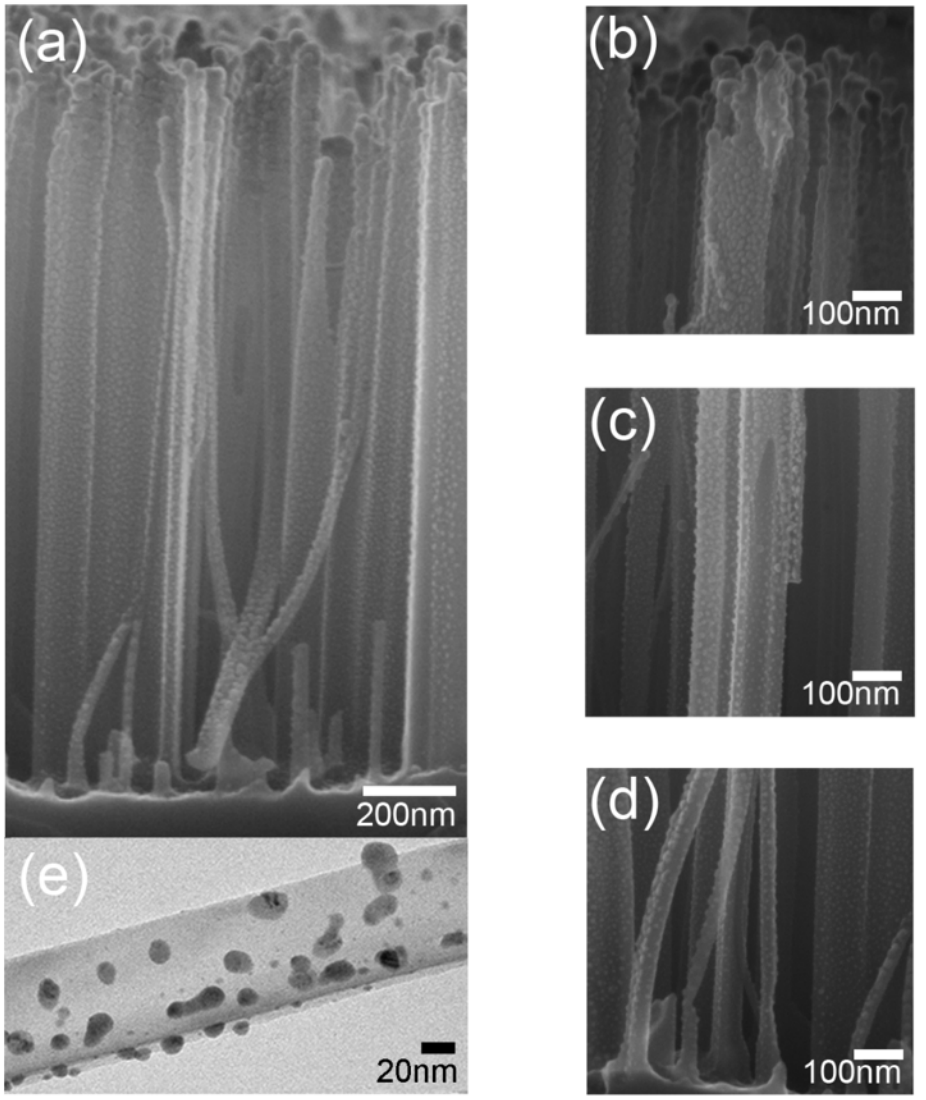


*Figure 5.4: (a) Plain SEM cross-section of Ag decorated Si NW sample 1. The high resolution SEM images correspond respectively to the (b) top, (c) center and (d) bottom sections of the wires. (e) TEM microscopy displaying the bottom section of an isolated Ag decorated Si nanowire [171].*

The TEM analysis shows an Ag NP size distribution ranging on the order of a few nanometers. Moreover, a huge amount of tiny isolated particles with a radius smaller than 2 nm is also observed, whose presence is not detectable by SEM investigation. Although these nanoparticles are present in high number, their presence does not determine any evident influence on the optical behavior of the system.

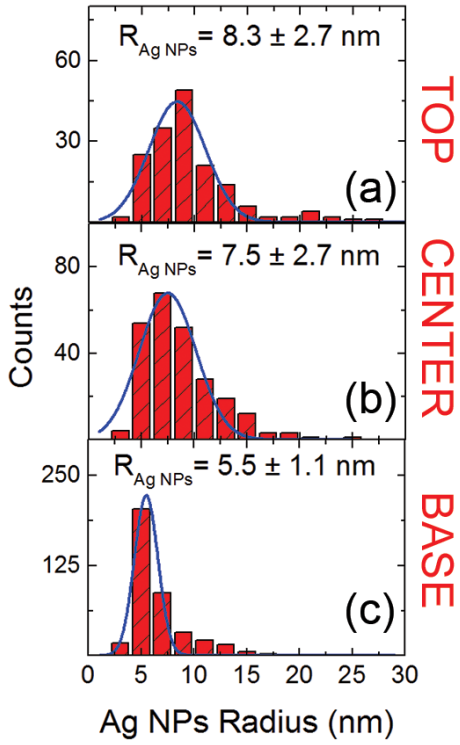


*Figure 5.5: Ag NP radius statistical analysis reported for sample 1 for the (a) top , (b) center and (c) bottom sections of the wires respectively.*

The SEM and TEM images have been analyzed by using Gatan Digital Microscopy in order to estimate the statistical distribution of Ag NPs mean size and first-neighbor distance for each wire section (top, center, bottom) of the total ensemble of samples. A total area of approximately 600x600 $nm^2$ has been investigated per each section in order to acquire a significant statistical ensemble of particles. The Ag NPs have been identified and selected through the software by adjusting the image contrast.

Finally, the selected Ag NP radii have been measured by pixel counting obtaining a frequency count statistics whose distribution was then fitted with a Gaussian function. In fig. 5.5 is reported the NP radius statistical analysis for sample 1 (estimated from fig. 5.4 (b-d)) for the (a) top, (b) center and (c) bottom region, respectively.
As demonstrated from the images, the formation of coalesced Ag NPs is clearly attested on NW tips where bigger nanoclusters display a mean radius of $8.3 \pm 2.7$ nm (fig. 5.5(a)). NW central section shows a dense and more uniform coverage, characterized by small and well separated Ag NPs having a mean radius of $7.5 \pm 2.7$ nm (fig. 5.5(b)). While even smaller and isolated Ag NPs can be distinguished in the bottom section having a mean radius of about $5.5 \pm 1.1$ nm (fig. 5.5(c)). The comparison of the radius statistics along the same sample demonstrates that the gaussian peak shifts towards smaller values from the tip to the NW basement. A similar behavior is appreciated for all decorated samples.

Another crucial parameter for SERS applications is the average edge-to-edge distance between Ag NPs. The interparticle distances have been measured connecting first neighbor NPs through linear segments digitally drawn on the SEM image by using an image editing software (Photoshop). The segment lengths have been measured by Gatan Digital Microscopy software and the interparticles distance statistics analyzed by using the same procedure adopted to calculate the mean radius.

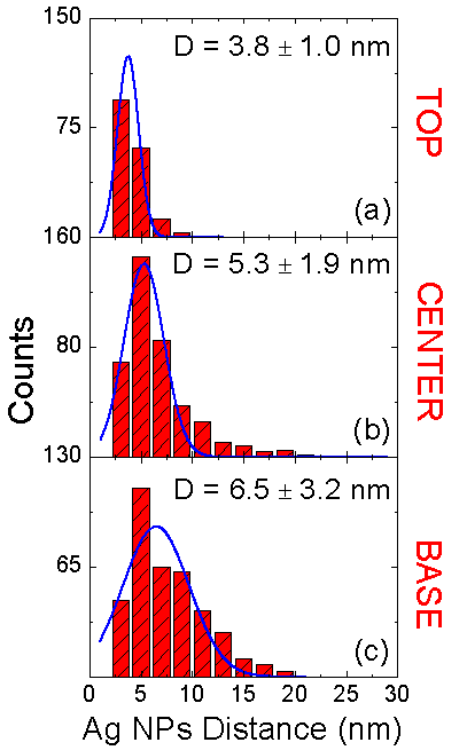


*Figure 5.6: Statistical analysis on first-neighbor Ag NP mean distance reported for sample 1 respectively for the (a) top , (b) center and (c) bottom sections of the wires.*

A mean interparticle distance of $3.8 \pm 1.0$ nm, $5.3 \pm 1.9$ nm and $6.5 \pm 3.2$ nm has been measured for sample 1 respectively from the top, center and bottom regions, as reported from the bar graph in fig. 5.6 (a), (b) and (c).
As far as the interparticle distance distribution is concerned, the NP mean distance increases from the top to the bottom of the wires showing exactly the opposite behavior recorded for the radius. The same trend is observed for all the decorated samples.
All the statistical results on Ag NP morphological characterization (mean radius and distance) are resumed in tab. 5.1 for the top, center and bottom sections of each sample.

| | | Sample 1 | Sample 2 | Sample 3 | Sample 4 |
|---|---|---|---|---|---|
| NW length ($\mu m$) | | 1.7 | 1.7 | 3.4 | 3.4 |
| Laser pulses | | 45,000 | 60,000 | 45,000 | 60,000 |
| Ag NP mean | top | $8.3 \pm 2.7$ | $11.3 \pm 4.3$ | $7.3 \pm 4.7$ | $10.4 \pm 3.0$ |
| radius r (nm) | center | $7.5 \pm 2.7$ | $7.4 \pm 2.2$ | $5.2 \pm 2.7$ | $7.6 \pm 3.8$ |
| | bottom | $5.5 \pm 1.1$ | $6.9 \pm 2.2$ | $4.6 \pm 2.5$ | $5.7 \pm 1.5$ |
| Ag NP mean | top | $3.8 \pm 1.0$ | $3.0 \pm 1.0$ | $4.3 \pm 2.0$ | $8.6 \pm 4.7$ |
| distance (nm) | center | $5.3 \pm 1.9$ | $4.8 \pm 1.8$ | $5.1 \pm 2.0$ | $11.5 \pm 9.4$ |
| | bottom | $6.5 \pm 3.2$ | $6.0 \pm 3.0$ | $9.8 \pm 6.0$ | $13.6 \pm 12.2$ |

*Table 5.1: Statistical results on Ag NPs mean radius and first neighbor distance along the top, center and bottom region of the Ag-decorated NW samples.*

Indeed, the results of the structural characterization reported in tab. 5.1 demonstrate that the Ag nanoparticles mean size decreases from the top to the bottom sections of the wire. This phenomenon observed for all samples suggests a relation to the deposition process itself. Initially Ag NPs formation by PLD process occurs during the flight, before reaching the sample surface. Therefore, NPs with the same mean radii arrive onto the three different sections of the wires. Later on however, the Ag NPs size distribution changes along the NW length.

The formation of coalesced nanoclusters with bigger size occurs at the top region that is the most exposed to the incoming particle beam. Only a fraction of the incident NPs is able to reach the center of the NWs and even a smaller portion arrives to the bottom. This process is responsible for the different NP radius and distance distributions observed along the wires length, regardless either of the NWs length or PLD pulses.

As far as the Ag NP mean distance distribution is concerned, it increases from the top to the bottom for all samples, an opposite behavior with respect to the radius. Once again the explanation lies within the decoration mechanism. Indeed, the formation of bigger and coalesced cluster having narrow spacing is induced on the top region, since it is the first one to be exposed to the NP beam. The decoration process leads to an occlusion of the gap between adjacent

nanowires, reducing the number and the diameter of the NPs impinging to the bottom of the wires that shows a bigger distance among neighbor nanoparticles. Furthermore, results in table 5.1 show that by keeping the same NW length and increasing PLD pulse number an increment of the NPs radius is reported for each wire section, as shown for both samples 1 and 2 and samples 3 and 4. This phenomenon related to the increment of Ag NPs impinging on the sample, favoring the coalescence of smaller NPs into bigger ones.
By contrast, using the same number of pulses and increasing the NW length, as for samples 1 and 3 or for samples 2 and 4, the Ag NP mean dimension slight decreases. In fact, by using longer NWs the probability that different Ag NPs are in a close position and coalesce is highly reduced. Indeed longer NWs show a higher value for the mean NPs distance. Therefore, we are able to control the size, distribution, distance and the coverage of the Ag NPs easily by varying either the NW length or the pulse number of the PLD process. This aspect is crucial for sensing application since the NP distribution strongly affects the SERS performances of the substrates.

## 5.2 Surface-Enhanced Raman Spectroscopy

A brief explanation of SERS phenomenon is given in the following section by using the simplified model of a *free electron gas* (Drude Model). According to Drude model, electrons in a metal can move freely along the space and are not bound either conditioned by the positive ions lattice. At a first approximation, the crystalline lattice is considered fixed and phonons or ion vibrations are here neglected. The conduction electrons in a metal generate a *free-electron plasma*, or simply a *plasmon*, whose properties strongly influence the overall optical response of the material. Generally, the plasma resonances can be obtained in the visible range for metal nanostructures. Therefore, under specific conditions the interesting coupling effects among plasma charges and external electromagnetic field can be observed. This plasma resonance condition is identified by considering the metal dielectric function $\epsilon(\omega)$.

According to Drude model, $\epsilon(\omega)$ can be written as follow:

$$\epsilon(\omega) = \epsilon_\infty \left(1 - \frac{\omega_p^2}{\omega^2 + i\gamma\omega}\right) \tag{5.1}$$

where $\omega$ is the frequency of the external electric field $E(\omega)$, $\epsilon_\infty$ describes the collective optical response of the positive ions background, $\gamma$ is a damping factor due to surface scattering attenuation processes and $\omega_p$ is defined as the plasma frequency. The plasma frequency can be regarded as the natural oscillation frequency of the electron plasma and therefore is defined as:

$$\omega_p = \sqrt{\frac{ne^2}{m\epsilon_0\epsilon_\infty}} \tag{5.2}$$

where $n$, $m$ and $e$ are the electron concentration, mass and charge value respectively. While $\epsilon_0$ is the dielectric function in vacuum condition.
A plasma wavelength $\lambda_p$ associated to plasma frequency is also defined:

$$\lambda_p = \frac{2\pi c}{\omega_p} \tag{5.3}$$

The dielectric function of the conduction electrons in a metal $\epsilon(\omega)$ defined in eq. 5.1 can be decomposed in the sum of a real and an imaginary part: $\epsilon(\omega) = Re(\epsilon(\omega)) + iIm(\epsilon(\omega))$. Where $Re(\epsilon(\omega))$ and $Im(\epsilon(\omega))$ are respectively related to the metal polarizability and absorption dissipation term, corresponding to:

$$Re(\epsilon(\omega)) = \epsilon_\infty \left(1 - \frac{\omega_p^2}{\omega^2 + \gamma^2}\right) = \epsilon_\infty \left(1 - \frac{\omega_p^2}{\omega^2}\left(\frac{1}{1 + \frac{\gamma^2}{\omega^2}}\right)\right) \tag{5.4}$$

$$Im(\epsilon(\omega)) = \frac{\epsilon_\infty \gamma}{\omega}\left(\frac{\omega_p^2}{\omega^2 + \gamma^2}\right) = \epsilon_\infty \gamma \frac{\omega_p^2}{\omega^3}\left(\frac{1}{1 + \frac{\gamma^2}{\omega^2}}\right) \tag{5.5}$$

In the approximation $\gamma \ll \omega$, the plasma frequency expression $\omega_p$ reported in eq. 5.2 is obtained imposing that $Re(\epsilon(\omega_p)) \sim 0$.
Therefore, for incoming wavelengths longer than $\lambda_p$, or equivalently for $\omega < \omega_p$, the real part of the dielectric function assumes negative values: $Re(\epsilon(\omega)) < 0$. At the same time, if $\omega$ is not too small

the absorption term becomes negligible $Im(\epsilon(\omega)) \sim 0$. When both conditions are satisfied it is possible to have a wide range of optical responses, plasma resonances included. Typically, for most metals the bulk plasma frequency is observed in the near UV region of the spectrum, thus the interesting range $\omega < \omega_p$ corresponds to the visible.

In order to understand the correlation among the dielectric function and the plasma resonances, we focus our attention to the case of a small metal sphere of radius $a$ interacting with an external electromagnetic field having amplitude $E_0$ and wavelength $\lambda$. When $a \ll \lambda$ we are in the Mie regime and the metal particle is not influenced by the field amplitude oscillations, perceiving it as a uniform electromagnetic field only.
This condition can be expressed as $a/\lambda < 0.1$ and is generally valid for nanometric metal NPs in the presence of visible radiation. Indeed, it is equivalent to the electrostatic problem of a sphere surrounded by a medium with relative dielectric function $\varepsilon_M$ and immersed in an uniform electric field. The problem can be solved exactly considering the Maxwell equations and the Mie theory for nanoparticle optical response [193, 194].
The Maxwell equation system can be solved by assuming the quasi-static approximation as a consequence of the small particle dimensions. Therefore, a final expression for the electric field inside the sphere $E_{in}$ as a function of the incident field $E_0$ is obtained:

$$E_{in} = E_0 \frac{3\varepsilon_M}{\epsilon(\omega) + 2\varepsilon_M} \tag{5.6}$$

According to eq. 5.6, when $\epsilon(\omega) \sim -2\varepsilon_M$ the internal field dramatically increases. Therefore, when the incident radiation frequencies $\omega$ satisfy both the conditions:

$$Re(\epsilon(\omega)) \sim -2\varepsilon_M \tag{5.7}$$

$$Im(\epsilon(\omega)) \sim 0 \tag{5.8}$$

the internal field $E_{in}$ is strongly amplified.

The above relations define the *resonance conditions* between the metal internal field and the incident field. When the resonance condition is matched, a *Localized Surface Plasmon Resonance* (LSPR) responsible for the SERS effect is observed. The LSPR is a coherent oscillation of the surface conduction electrons established when the exciting electromagnetic radiation frequency $\omega$ matches the natural frequency of the surface electrons oscillating against the restoring force of positive ions (see fig. 5.7).

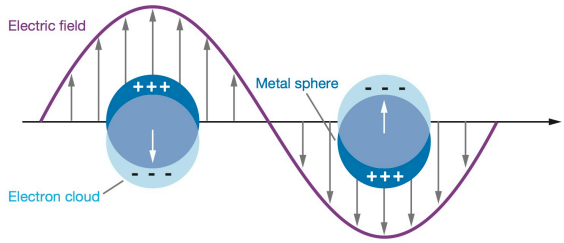


*Figure 5.7: Diagram of a localized surface plasmon oscillation.*

Thus, the resonance conditions produce a resonant coupling among the external electric field and the typical metallic plasmon.
Some important parameters must be taken into account in order to match the plasmon resonance, as the electron density of the metal, the metal particle dimension and its optical features ( $Re(\epsilon(\omega))$ and $Im(\epsilon(\omega))$). In this sense, gold and silver present very good optical properties and for this reasons they are the most widely used metals for plasmon applications [195]. Indeed, Au and Ag have very similar electronic densities and dielectric function real parts ($Re(\epsilon(\omega))$) trends. On the other hand, for $\lambda \leq 700$ nm Au imaginary part $Im(\epsilon(\omega))$ has a higher absorption with respect to Ag due to its interband electronic transitions. While for $\lambda \geq 700$ nm the two imaginary parts return comparable. Furthermore, the metal NP size and shape have a key role in the LSPR achievement. Indeed, by increasing the particles diameters major detrimental effects occur: a change of the polarizability and a LSPR red-shift resulting in an oscillation damping and in an overall widening of the resonance [196]. Moreover, multipolar plasmon resonances arise when the condition $a/\lambda < 0.1$ is shifted, that are less efficiently coupled to the electromagnetic field with respect to the dipole ones [176].

Finally, the symmetrical spherical shape also guarantees a good distribution of the plasmon resonances on the surface. Indeed, the symmetry breaking can result in a complicated involution of the amplified fields eventually leading to the observation of more than one resonance. Thus, even the shape and the metal NP orientation with respect the incident field assume a great importance. A further crucial aspect for application is that when the metal NPs are resonant with respect to the incoming radiation they can strongly amplify the local electric field by several orders of magnitude. Indeed, when metal nanostructures, as for spherical NPs, are narrowly separated from one another on the order of a few nanometers their induced dipoles start to interact. The NPs are therefore optically coupled and the generated electric fields strongly affect the local fields configuration producing a resonance energy shift. In the end, the local field intensity is strongly amplified by several orders of magnitude in the area between neighbor NPs. These interparticle regions where a local field enhancement is observed are commonly called *hot-spots* (as shown in fig. 5.8 (a)) [70]. The amplification factors sharply decrease far away from the hot-spots regions.

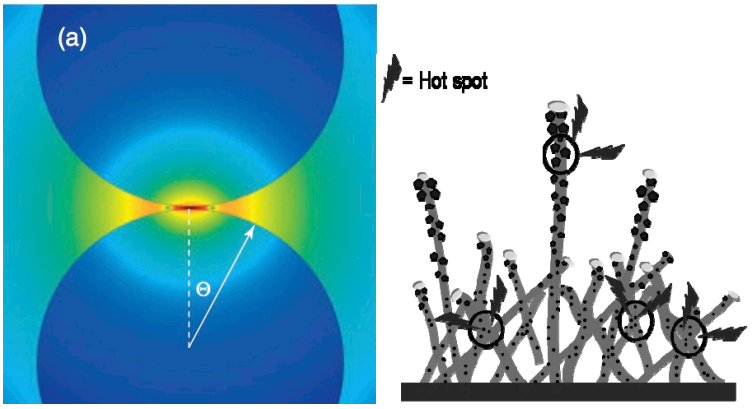


(a) (b)

*Figure 5.8: (a) Simulation of an hot-spot region formation between two metal NPs showing the field enhancement in a false color scale. (b) High density hot-spots distribution scheme on a Si NWs substrate [197, 196].*

As far as molecule spectroscopy is concerned, a molecule adsorbed on the hot-spot area experiences a dramatic amplification of its emission signal and in particular its Raman spectra is strongly enhanced. The *Surface Enhanced Raman Spectroscopy (SERS)* is an effect based on the properties of metal NPs of enhancing the detection of molecular Raman signals that would not be observed otherwise [198, 199, 200].

The Raman signal is a clear fingerprint of molecular species associated to their vibrational states. Nevertheless, Raman is a very low probable effect with respect to others radiative processes like fluorescence. Therefore, the local enhancement effect induced by metal NPs represents a new frontier for molecular SERS detection.
Molecule detection sensitivity and efficiency can be highly increased by increasing the free exposed area. Si NWs represent a very promising material for sensing and SERS application due to their huge surface-to-volume ratio. Indeed, it is possible to drastically increase the hot-spots density by metal decoration of NWs, further increasing both sensing sensitivity and power amplification. The probability that a target molecule is absorbed in an hot-spot active area is very high, as shown in fig. 5.8 (b), thus leading to the detection of extremely low concentration of molecules on decorated Si NW arrays with respect to the corresponding flat substrate.

SERS phenomenon is a linear effect, meaning that the intensity is proportional to the incident field intensity ($E_0$) and to the molecular Raman cross section ($\sigma_R$) increased by an enhancement factor (EF). In general, the EF is defined as the ratio between the Raman intensity of a molecular sample on a SERS substrate and the Raman intensity of the same sample on a non-SERS substrate. In literature the EF is associated to two main multiplicative terms, the chemical enhancement factor and the electromagnetic enhancement factor (EM). The first one is smaller than the EM factor and it only contributes with $1 \div 2$ orders of magnitude to the overall amplification [201], whereas EM is the most important factor generally responsible for $8 \div 10$ orders of magnitude amplification of the emitted radiation. It is related to the coupling effect among the incident field, the Raman signal and the localized plasmon resonance on the SERS substrate.
Therefore, it can be divided in two main contributions: one for the incident radiation which is locally enhanced and the other for the

Raman radiation which is in turn also amplified. So, it is evident that SERS EF is strongly dependent on parameters like the excitation wavelength, the scattering geometry, the SERS-active substrate and the molecular properties. It is worth noticing that EM EF can also be described by the $|E|^4$ *approximation*. It considers a molecular analyte adsorbed on a metal NP surface and a laser beam focused on the nanostructure, as shown in fig. 5.9.

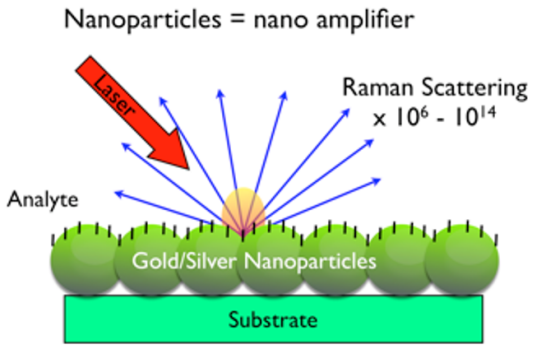


*Figure 5.9: Representative scheme displaying the local field amplification of the analyte Raman signal occurring when a laser beam is focused on a substrate covered with resonant metal nanoparticles.*

When the incident field $\mathrm{E}_0(\omega_L)$ has a frequency $\omega_L$ close to the plasmon resonance frequency of the material, then it can resonantly excite the localized plasmon oscillation on the substrate. As a consequence, the antenna effect gives rise to hot-spot regions where the incident field is locally greatly amplified: $\mathrm{E}_{loc}(\omega_L)$. The two fields are connected by the following relation:

$$E_{loc}(\omega_L) = \Gamma_{exc}(\omega_L) E_0 \tag{5.9}$$

where $\Gamma_{exc}(\omega_L)$ is the amplification factor which strongly amplifies the incident field. Thus, the enhanced field acts like a more powerful laser on the molecule, exciting its Raman scattering $\mathrm{E}_{Raman}(\omega_R)$ more efficiently. In addition, the Raman signal itself is amplified by the hot-spot action by a factor $\Gamma_{rad}(\omega_R)$ resulting from the cavity coupling. As a consequence, the final SERS field emission results:

$$E_{SERS}(\omega_R) = \Gamma_{rad}(\omega_R) E_{Raman} \tag{5.10}$$

Using the definition of signal intensity $I \propto |E|^2$ it is evident that the overall EF is the product of both amplification terms

$$EF = \Gamma^2_{exc}(\omega_L)\Gamma^2_{rad}(\omega_R) \tag{5.11}$$

In addition, using the first definition of EF and the two relations 5.9 and 5.10 it is possible to write:

$$EF \sim \frac{I_{SERS}}{I_{Raman}} = \left|\frac{E_{loc}(\omega_L)}{E_0(\omega_L)}\right|^2 \times \left|\frac{E_{SERS}(\omega_R)}{E_{Raman}(\omega_R)}\right|^2 \sim \left|\frac{E_{loc}(\omega_L)}{E_0(\omega_L)}\right|^4 \tag{5.12}$$

resulting from the reasonable approximation $\Gamma_{exc}(\omega_L) \sim \Gamma_{rad}(\omega_R)$ when the condition $\omega_L \sim \omega_R$ is satisfied. Indeed, the plasmon resonance is generally much larger than the Stokes shift, meaning that it interacts at the same way with the incoming and the outcoming radiation.
The relation 5.12 represents the $|E|^4$ approximation and it gives a good value of the overall amplification order of magnitude. The simplyfied model explained in this section gives a satifying overview of the SERS phenomenon. Although, a more complete explanation can be obtained taking into account the complex molecular Raman answer, the polarization effects and possible further frequency dependence of the $\Gamma$ factors. All these aspects are objects of current research in the SERS field and are generally grouped as "beyond $|E|^4$ model" considerations [202].

## 5.3 Optical characterization of Si NW SERS sensors

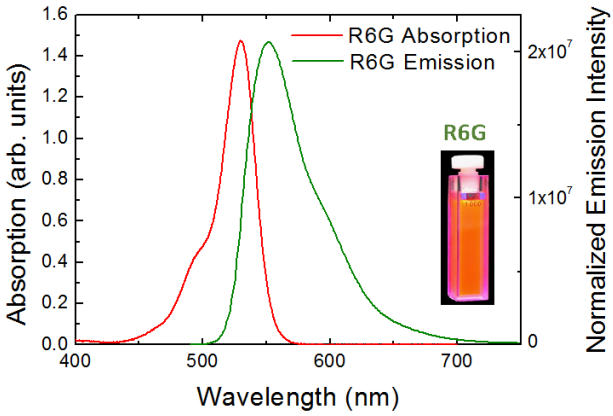


*Figure 5.10: Typical absorption and emission spectra of rhodamine 6G (R6G) organic dye molecule chosen as probe for SERS measurements. The inset shows a photo of a vials containing a fluorescent solution of* $10^{-3}M$ *of rhodamine in water [203].*

The SERS activity of Ag NPs decorated Si NWs has been tested by using rhodamine 6G (R6G) as probe molecules, an organic dye often adopted in literature [204, 205].
The absorption (red line) and emission spectra (green line) of R6G dispersed in ethanol are presented in fig. 5.10. Where an absorption band ranging between 450 and 550 nm is clearly observed and characterized by two absorption peaks centered at 490 nm and 525 nm for R6G dimer and monomer aggregates respectively. Furthermore, a broad visible fluorescence band is observed from 500 nm to 650 nm, obtained from the superposition of two emission peaks at 550 nm and 600 nm from the monomer and dimer emission contributions. The strong R6G fluorescence is also observed by the naked eye, as shown from the inset displaying a photo of a vials containing a rhodamine solution.
Therefore, the high fluorescence emission and the very low R6G Raman cross-section ($\sigma = 10^{-29} cm^2$) make the molecule detection by Raman spectroscopy quite impossible on standard substrates for concentrations below $10^{-2}$ M [202].

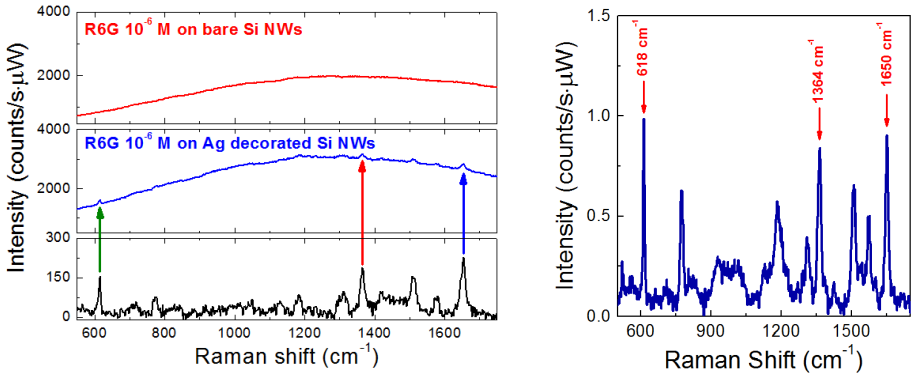


(a) (b)

*Figure 5.11: (a) Raman/SERS spectra of* $10^{-6}M$ *concentration of R6G acquired at the 514.5 nm excitation wavelength for bare (red line) and Ag-decorated Si NWs (sample 1) (blue line) respectively. In black is reported the SERS spectrum obtained under the same condition when the fluorescence background is subtracted. The three lines indicate the reference R6G Raman peaks at 618 (green), 1364 (red) and 1650 (blue)* $cm^{-1}$*, whose intensities have been used to compare samples performances as plotted in the histogram reported in fig. 5.12.*
*(b)SERS spectrum of* $10^{-6}$ *M of rhodamine 6G (R6G) acquired on decorated NW sample 1. labelrho*

Rhodamine 6G has hence been inserted on Si NWs decorated with Ag nanoparticles. Upon the Ag NP decoration of Si NWs by PLD process all samples have been prepared for SERS measurements. Decorated NWs were first treated by UV cleaning process for 10 minutes in order to remove any possible organic contamination. The cleaning procedure has been optimized in order to effectively remove contaminants and avoid the formation of an AgO shell around the NPs. The contaminants and AgO presence have been excluded by preliminary Raman spectroscopy before immersing the Ag-decorated Si NW samples in the rhodamine solution. The NWs samples have been soaked for 150 min in an aqueous solution with rhodamine concentration ranging from $10^{-4}$ up to $10^{-9}$ M and then left to dry in air.
SERS measurements have been performed by focusing through a 50x LWD objective (NA = 0.5) the 514 nm line of an $Ar^{+}$ on the samples surface with a pump power of 510 $\mu$W.

The radiation has been collected in a back scattering configuration and analyzed with a micro-Raman spectrometer coupled with a CCD detector. All spectra have been normalized to the laser power and acquisition time. Figure 5.11(a) shows the Raman spectra of bare Si NWs (in red) and Ag decorated Si NWs sample 1 (in blue) in the presence of $10^{-6}$ M of rhodamine obtained under the same experimental conditions. From a first comparison it can be observed that only R6G fluorescence signal is detected on bare Si NWs, while the typical rhodamine Raman peaks are observed in the presence of Ag NP decorated NWs (blue line).
In the following graph is repoted in black the SERS spectrum of Ag decorated NW sample 1 at the $10^{-6}$ M concentration of R6G obtained by subtracting the fluorescence background (red) from the Raman spectrum (blue). This spectrum displays the three typical rhodamine peaks at 618, 1364 and 1650 $cm^{-1}$, respectively highlighted by green, red and blue arrows and whose intensities have been used as references to test the sample performances.

An enlargement of the R6G Raman spectrum is reported in fig. 5.11(b), showing several typical peaks that simplify the molecule detection and characterization. Indeed as highlighted in fig. 5.11(b), three major narrow peaks can be identified at 618, 772 and 1120 $cm^{-1}$ respectively associated to the C-C-C ring in-plane and out-of-plane bending modes and C-H in-plane bending vibrations. Moreover, the presence of typical C-C symmetric stretching modes bands are observed for at 1190, 1364, 1509, 1572 and 1650 $cm^{-1}$ [206]. In fig. 5.12 is reported a comparison among the three reference peak intensities (618, 1364 and 1650 $cm^{-1}$) for the different sample decorations. The error bars take into account of noise fluctuations of the flat part of the spectrum which are considered as the peak intensity indetermination. From this analysis can be concluded that sample 1 ( 1.7 $\mu m$, 45,000 pulses) and sample 4 (3.4 $\mu m$, 60,000 pulses) are the best performing samples for the same R6G concentration.
In particular, Ag NPs on sample 1 are optically coupled and form hot spots that resonantly match the optimal SERS efficiency conditions at the 514.5 nm excitation.

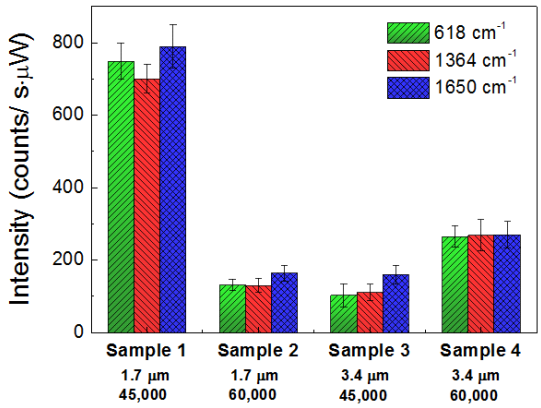


*Figure 5.12: The histogram reports the intensitiy of the three reference R6G Raman peaks at 618 (green), 1364 (red) and 1650 (blue) $cm^{-1}$ used to compare samples performances.*

The different optical behavior can be explained considering the Ag NP morphology variations reported in tab. 5.1. In comparison to sample 1 the variations of the NP dimension (as for sample 2), the NP distribution along the NW length (for sample 3) or the inter-particle distance (for sample 4) result in a lower SERS efficiency due to a plasmon resonance shift, to lower hot-spots density, or to a less efficient optical coupling between the NPs, respectively.
Moreover, sample 4 Ag NPs show the typical plasmon resonance of a spherical and *isolated distribution* of nanoparticles that are therefore weakly coupled [207]. It can be concluded that Ag NP mean radius and average distance play a crucial role in terms of LSPR peak width and position and thus for SERS efficiency [202]. In order to better explain the observed behavior we have characterized the plasmon resonances in our samples. A plasmon resonance peak is observed when the collective oscillation excitation of electrons is promoted by the incoming excitation wavelength on the metal samples surface. When the resonance condition between the incident electric field and the conduction band electrons coherent oscillation is matched, a strong local field enhancement responsible for the SERS phenomenon is observed. The morphological differences among the samples appreciated from the structural characterization determine different SERS responses for each material.

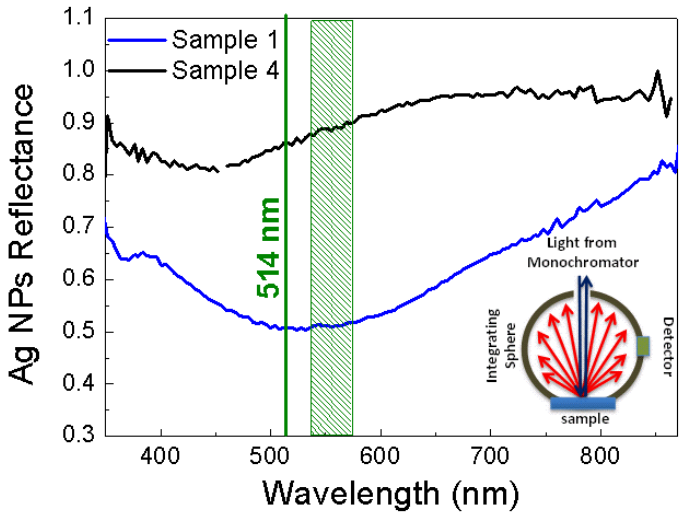


*Figure 5.13: Ag NP Reflectance spectra reported as a function of the exciting wavelength for samples 1 (blue line) and samples 4 (black line). The reflectance minima identify the LSPR peaks associated to the decoration process. The green line marks the 514.5 nm excitation wavelength adopted for SERS analysis, while the dashed box highlights the rhodamine active Raman range expressed in nanometer (550 - 1750 $cm^{-1}$). The inset shows a representative scheme of the experimental setup used for the diffused reflectance measurements [171].*

Indeed, the local surface plasmon resonance (LSPR) peak position is strictly dependent on the metal species and surface properties, in particular is highly affected by the mean dimensions and distances of NPs. It is not possible to perform transmission measurements on silicon since the substrate is not transparent in the visible range where our plasmon resonances lye. Therefore all samples reported in tab. 5.1 have been optically characterized by reflectivity measurements in order to obtain the LSPR peak position associated to the decoration morphology. The reflectance spectra have been acquired by using a a double-beam spectrophotometer equipped with an integrating sphere in diffuse reflectance configuration avoiding the specular reflected light components and allowing the measurement of the diffused light only, as shown from the inset displayed in fig. 5.13. It is worth noticing that the surface plasmon oscillations depend only on

the metallic structure and are not affected by the Si substrate. On the other hand, Si NW dense arrays strongly influences the overall optical response of the substrates resulting in a strong light absorption due to occurrence of efficient in-plane multiple scattering through the structure, as already demonstrated in the previous chapters (par. 3.3).
To take into account only for the Ag NPs contribution the reflectance spectra have been normalized to the corresponding as-prepared Si NWs one, avoiding any substrate influence. The Ag NPs diffused reflectance has been normalized according to the following relationship:

$$I_{AgNP} = \frac{I_{NWdecorated}}{I_{NWbare}} \tag{5.13}$$

where $I_{NWdecorated}$ and $I_{NWbare}$ are the diffused reflectance intensities from the Ag NP decorated and bare Si NW substrates, respectively. The Ag NP reflectance spectra are reported in fig. 5.13 for the best SERS performing samples, respectively samples 1 (blue line) and samples 4 (black line). A reflectance minimum attests a strong absorption associated to the surface plasmon resonance associated typical of the material. Sample 1 reflectance (blue line) shows a broad minimum from 400 nm to 700 nm corresponding to a LSPR peak centered at about 540 nm. A similar behavior is observed for sample 4 (black line) that presents a LSPR peak at 450 and a plasmon resonance range between 350-600 nm.
Therefore it is possible to match the resonance conditions needed to observe SERS enhancement by using 514 nm as exciting wavelength that is very close to the plasmon peaks for all samples.

Another crucial parameter for SERS sensing is the enhancement factor (EF) induced by metal NPs. The EF is typically defined as the SERS and Raman intensities ratio evaluated per molecule. As well known in the literature, the R6G Raman signal is hardly detectable on standard samples even for higher concentrations. Therefore, in order to calculate the EF a comparison among the Raman and the fluorescence cross sections, $\sigma_R$ and $\sigma_R$, has been made.

The signal intensities ratio per molecule and per watt power can also be defined as the the following cross sections ratio:

$$\frac{I_{SERS}}{I_F} = EF\frac{I_{Raman}}{I_F} \approx EF\frac{\sigma_{Raman}}{\sigma_F} \approx EF \times 10^{-9} \quad (5.14)$$

$$\Rightarrow EF = 10^9\frac{I_{SERS}}{I_F} \quad (5.15)$$

where $I_{SERS}$ and $I_F$ are the SERS and fluorescence background intensities estimated for decorated nanowires, as measured from fig. 5.11(a). The rhodamine Raman cross section is of about $\sigma_R = 10^{-29}$ $cm^2$ and can be increased up to $\sigma_{RR} = 10^{-25}$ $cm^2$ when the resonance conditions is matched ($\lambda_{exc} = 514.5$ nm) [198].
The fluorescence cross section evaluated at the same wavelength is about $\sigma_R = 10^{-16}$ $cm^2$ [208, 209]. As a consequence, a $10^{-9}$ factor is obtained from $\frac{I_{Raman}}{I_F}$ ratio, as expressed in equation 5.15.

EF values of approximately $3 \cdot 10^8$ and $10^8$ have been calculated from this equation for sample 1 and 4, respectively, demonstrating the strong potential of the Ag NP decorated Si NWs as SERS active substrates. Indeed, Ag decorated Si NW enhancement factors are about one order of magnitude higher with respect to $EF = 1.9 \cdot 10^7$ value obtained for Ag NPs deposited by PLD on a flat glass surface measured according to the same procedure [202, 210]. A result that is due to the higher hot spots density distributed along the nanowires vertical array, leading to the formation of a better 3D architecture with respect to the 2D case. The most important applications of the SERS active substrates is the realization of a molecular sensor. In order to test the sensitivity of the sensors the lower limit of detection (LOD) has been evaluated as the smallest concentration of the target analyte that is still distinguished from the noise level [211]. For this purpose SERS measurements as a function of the R6G molar concentration in aqueous solutions, ranging from $10^{-9}$M to $10^{-4}$ M, were performed for sample 1 as shown in fig. 5.14.

SERS spectra averaged on ten different points of the samples have been acquired at the 514.5 nm excitation wavelength and normalized to the acquisition time and laser power making it possible the comparison among each other. Moreover, the fluorescence background has been subtracted in order to better estimate the SERS signals as a function of the concentration.

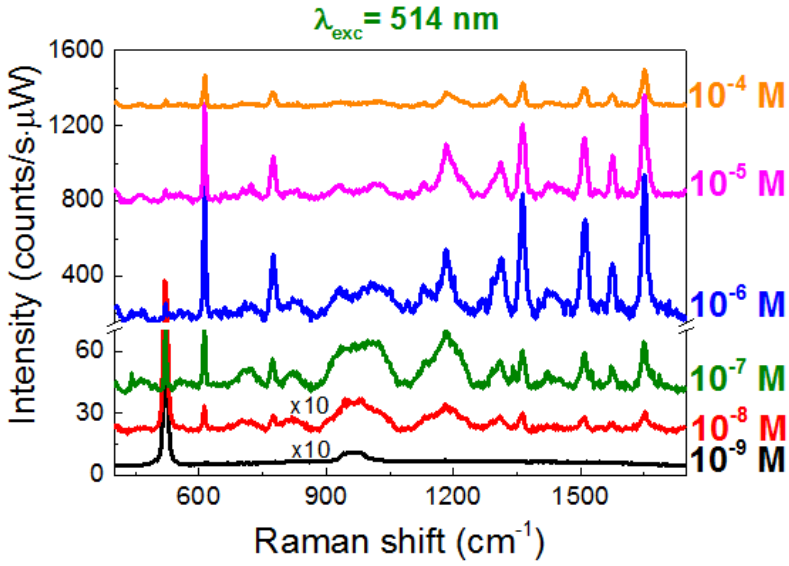


*Figure 5.14: (a) SERS spectra acquired for sample 1 for different R6G concentrations ranging from* $10^{-4}$ *to* $10^{-9}$ *M by exciting the system at the 514.5 nm line of an* $Ar^{+}$ *laser. All spectra have been normalized to the fluorescence background [171].*

From fig. 5.14, no SERS signals are detectable for the $10^{-9}$M R6G concentration. Whereas R6G characteristic signals are present above $10^{-8}$M concentration, establisting the LOD of the system. The local intensity variations has been taken into account by calculating the standard deviation for each set of measurements in order to test the uniformity of the SERS performances across the sensing surface. The intensity fluctuations of the three R6G peaks are lower than 15% per each concentration, a value that matches the criteria of reproducibility on large areas for SERS substrates: typically better than 20% [212, 213]. The SERS spectra are composed of the superposition of R6G SERS peaks and fluorescence broad band. This fluorescence background can be considered as a noise for SERS signal detection. In order to estimate the noise influence on SERS measurements the R6G reference peaks (618 $cm^{-1}$, 1364 $cm^{-1}$ and 1650 $cm^{-1}$) have been measured as a function of R6G concentration. Figure 5.15 shows the three vibrational modes intensities plotted on a logarithm scale for R6G concentration from $10^{-9}$M to $10^{-4}$M.

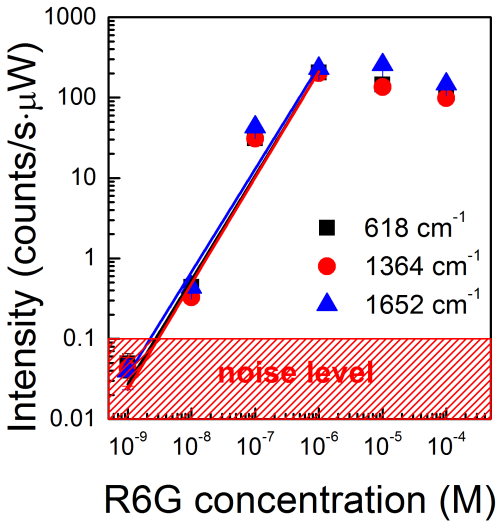


*Figure 5.15: The intensities of the 618 $cm^{-1}$, 1364 $cm^{-1}$ and 1650 $cm^{-1}$ peaks are reported as function of the R6G concentration ($10^{-9}$ - $10^{-4}M$) and linearly fitted up to $10^{-6}M$ [171].*

The peak intensity errors has been estimated by considering the intensity fluctuations measured on a flat region of the Raman spectra. As it is revealed from this analysis, the three peaks intensities are not visible at the lowest concentration of $10^{-9}$M (fig. 5.14) and SERS signals are covered by the noise background. Figure 5.15 reports that the R6G peak intensities linearly increase from $10^{-8}$M to $10^{-6}$M. Whereas they slightly decrease for concentrations between $10^{-5}$M to $10^{-4}$M. This signal saturation is reasonably ascribed to the saturation of the available SERS active sites by the adsorbed R6G molecules.
Indeed, although SERS active substrates amplify the overall molecular emission signal, above concentration of $10^{-6}$M the competing fluorescence process increases significantly due to the increment of the non-adsorbed R6G molecules number. Therefore, a reduction of the SERS exciting radiation is observed when the incoming light is absorbed by such molecules. The low LOD ($10^{-8}$M) and the high performances of Ag decorated Si NWs promote this material as a very promising SERS active substrate for molecule detection.

## 5.4 Conclusion

In this chapter, the realization and characterization of high performances Si NW-based SERS substrates has been exploited. Si NW arrays with different morphological features and lengths have been fabricated by silver salts MACE and decorated with Ag NPs produced by PLD. This strategy leads to an efficient coupling of the huge NW aspect ratio and Ag plasmonic effects by using two low-cost and Si-technology compatible techniques.
A detailed structural characterization on Ag decorated NWs demonstrated that the Ag NP size and distance distribution can be controlled according to two parameters: NW lengths or PLD pulse number. Moreover, a uniform and dense decoration of Si NW arrays with chemically-free metal NPs has been obtained overall the wire lengths, regardless of NW morphology and PLD parameters. The different SERS behaviors of decorated samples have been explained by a careful comparison between the morphological and optical characterization.

Ag decorated Si NW substrates have then been immersed in a rhodamine 6G aqueous solution to test the SERS performances. The SERS spectra clearly reveal that the detection power of the decorated substrates is enhanced by a $10^8$ factor that is more than one order of magnitude with respect to the Ag NP deposition on a Si flat substrate obtained with a similar procedure.
Furthermore, a low limit of detection down to concentrations as low as $10^{-8}$M of R6G have been observed, strongly attesting the great potential of Ag NP decorated Si NWs as powerful 3D SERS sensors for molecular detection.

# References


[1] Waldrop, M. M. *et al.*, "More than Moore", *Nature* **530** 147 (2016).

[2] Canham, L. T., "Silicon quantum wire array fabrication by electrochemical and chemical dissolution of wafers", *Applied Physics Letters* **57** 10 (1990).

[3] Reichardt, N. C. *et al.*, "Glyconanotechnology", *Chem. Soc. Rev.* **42**, 4358–4376 (2013).

[4] Delley, B. *et al.*, "Size dependence of band gaps in silicon nanostructures", *Applied Physics Letters* **67** 16 (1995).

[5] Kovalev, D. *et al.*, "Breakdown of the $k$-conservation rule in si nanocrystals", *Phys. Rev. Lett.* **81** (1998).

[6] Delley, B. *et al.*, "Quantum confinement in si nanocrystals", *Phys. Rev. B* **47** (1993).

[7] Garnett, E. *et al.*, "Light trapping in silicon nanowire solar cells", *Nano Letters* **10** 3 (2010).

[8] Peng, K. *et al.*, "Dendrite-assisted growth of silicon nanowires in electroless metal deposition", *Advanced Functional Materials* **13** 127 (2003).

[9] Wagner, R. S. *et al.*, "Vapor–liquid–solid mechanism of single crystal growth", *Applied Physics Letters* **4** 89 (1964).

[10] Schmidt, V. *et al.*, "Silicon nanowires: A review on aspects of their growth and their electrical properties", *Advanced Materials* **21** 2681 (2009).

[11] Kim, B. *et al.*, "Kinetics of individual nucleation events observed in nanoscale vapor–liquid–solid growth", *Nanotechnology* **322** 1070 (2008).

[12] Park, Y.-S. *et al.*, "Annealed au-assisted epitaxial growth of si nanowires: Control of alignment and density", *Langmuir* **31** 14 (2015).

[13] Nebol'sin, V. A. and Shchetinin, A. A., "Role of surface energy in the vapor–liquid–solid growth of silicon", *Inorganic Materials* **39** 9 (2003).

[14] Cui, Y. *et al.*, "Diameter-controlled synthesis of single-crystal silicon nanowires", *Applied Physics Letters* **78** 15 (2001).

[15] Mouchet, C. *et al.*, "Growth of one-dimensional si/sige heterostructures by thermal cvd", *Nanotechnology* **19** 33 (2008).

[16] Pan, Z. W. *et al.*, "Temperature-controlled growth of silicon-based nanostructures by thermal evaporation of sio powders", *The Journal of Physical Chemistry B* **105** 13 (2001).

[17] Shi, W. S. *et al.*, "Synthesis of large areas of highly oriented, very long silicon nanowires", *Advanced Materials* **12** 18 (2000).

[18] Schubert, L. *et al.*, "Silicon nanowhiskers grown on (111)si substrates by molecular-beam epitaxy", *Applied Physics Letters* **84** 24 (2004).

[19] Zhang, Y. F. *et al.*, "Diameter modification of silicon nanowires by ambient gas", *Applied Physics Letters* **75** 13 (1999).

[20] Hanrath, T. and Korgel, B., "Supercritical fluid–liquid–solid (sfls) synthesis of si and ge nanowires seeded by colloidal metal nanocrystals", *Advanced Materials* **15** 5 (2003).

[21] Holmes, J. D., Johnston, K. P., Doty, R. C., and Korgel, B. A., "Control of thickness and orientation of solution-grown silicon nanowires", *Science* **287** 5457 (2000).

[22] Tan, T. Y. *et al.*, "Is there a thermodynamic size limit of nanowires grown by the vapor-liquid-solid process?", *Applied Physics Letters* **83** 6 (2003).

[23] Dubrovskii, V. G. *et al.*, "Growth kinetics and crystal structure of semiconductor nanowires", *Physical Review B* **78** 235301 (2008).

[24] den Hertog, M. I. *et al.*, "Control of gold surface diffusion on si nanowires", *Nano Letters* **8** 1544 (2008).

[25] Dupré, L. *et al.*, "Gold contamination in vls-grown si nanowires: Multiwavelength anomalous diffraction investigations", *Chemistry of Materials* **24** 4511 (2012).

[26] Perea, D. E. *et al.*, "Direct measurement of dopant distribution in an individual vapour-liquid-solid nanowire", *Nature Nanotechnology* **4** 5 (2009).

[27] Koren, E. *et al.*, "Measurement of active dopant distribution and diffusion in individual silicon nanowires", *Nano Letters* **10** 1163 (2010).

[28] Hsu, C.-M. *et al.*, "Wafer-scale silicon nanopillars and nanocones by langmuir–blodgett assembly and etching", *Applied Physics Letters* **93** 13 (2008).

[29] Vieu, C. *et al.*, "Electron beam lithography: resolution limits and applications", *Applied Surface Science* **164** 1–4 (2000).

[30] Koops, H. W. P. *et al.*, "High-resolution electron-beam induced deposition", *Journal of Vacuum Science & Technology B* **6** 1 (1988).

[31] Heuberger, A. *et al.*, "X-ray lithography using synchrotron radiation and ion-beam shadow printing", *Proceedings SPIE* **0393** November 7 (1983).

[32] Morton, K. J. *et al.*, "Wafer-scale patterning of sub-40 nm diameter and high aspect ratio (>50:1) silicon pillar arrays by nanoimprint and etching", *Nanotechnology* **19** 34 (2008).

[33] Yang, J. K. W. *et al.*, "Understanding of hydrogen silsesquioxane electron resist for sub-5-nm-half-pitch lithography", *Journal of Vacuum Science & Technology B* **27** 6 (2009).

[34] Juhasz, R. *et al.*, "Controlled fabrication of silicon nanowires by electron beam lithography and electrochemical size reduction", *Nano Letters* **5** 2 (2005).

[35] Walavalkar, S. *et al.*, "Tunable visible and near-IR emission from sub-10 nm etched single-crystal si nanopillars", *Nano Letters* **10** 4423 (2010).

[36] Li, Z. *et al.*, "Fabrication of single-crystal silicon nanotubes with sub-10 nm walls using cryogenic inductively coupled plasma reactive ion etching", *Nanotechnology* **27** 36 (2016).

[37] Huang, Y. F. *et al.*, "Metal-assisted chemical etching of silicon: A review", *Advanced Materials* **23** 285 (2011).

[38] Li, X. *et al.*, "Metal-assisted chemical etching in hf/h2o2 produces porous silicon", *Applied Physics Letters* **77** 16 (2000).

[39] Harada, Y., , *et al.*, "Catalytic amplification of the soft lithographic patterning of si. nonelectrochemical orthogonal fabrication of photoluminescent porous si pixel arrays", *Journal of the American Chemical Society* **123** 36 (2001).

[40] Peng, K. *et al.*, "Metal-particle-induced, highly localized site-specific etching of si and formation of single-crystalline si nanowires in aqueous fluoride solution", *Chemistry – A European Journal* **12** 30 (2006).

[41] Peng, K. *et al.*, "Simultaneous gold deposition and formation of silicon nanowire arrays", *Journal of Electroanalytical Chemistry* **558**, 35 – 39 (2003).

[42] Peng, K. *et al.*, "Uniform axial-orientation alignment of one-dimensional single-crystal silicon nanostructure arrays", *Angewandte Chemie International Edition* **44** 2737 (2005).

[43] Chang, S.-W. *et al.*, "Metal-catalyzed etching of vertically aligned polysilicon and amorphous silicon nanowire arrays by etching direction confinement", *Advanced Functional Materials* **20** 24 (2010).

[44] Cui, Y. *et al.*, "High performance silicon nanowire field effect transistors", *Nano Letters* **3** 2 (2003).

[45] Goldberger, J. *et al.*, "Silicon vertically integrated nanowire field effect transistors", *Nano Letters* **6** 5 (2006).

[46] Warren, E. L. *et al.*, "Silicon microwire arrays for solar energy-conversion applications", *The Journal of Physical Chemistry C* **118** 2 (2014).

[47] Cui, Y. *et al.*, "Nanowire nanosensors for highly sensitive and selective detection of biological and chemical species", *Science* **293** 1289 (2001).

[48] Patolsky, F. *et al.*, "Nanowire sensors for medicine and the life sciences", *Nanomedicine* **1** 1 (2006).

[49] Chan, C. K. *et al.*, "High-performance lithium battery anodes using silicon nanowires", *Nature Nanotechnology* **3** 31 (2008).

[50] Bogart, T. D. *et al.*, "Lithium ion battery peformance of silicon nanowires with carbon skin", *ACS Nano* **8** 1 (2014).

[51] Ren, J. G. *et al.*, "A silicon nanowire-reduced graphene oxide composite as a high-performance lithium ion battery anode material", *Nanoscale* **6** (2014).

[52] Heinzig, A. *et al.*, "Reconfigurable silicon nanowire transistors", *Nano Letters* **12** 1, 119–124 (2012).

[53] Colace, L. *et al.*, "Germanium near infrared detector in silicon on insulator", *Applied Physics Letters* **91** 2 (2007).

[54] Zhang, J. *et al.*, "Advances in ingaas/inp single-photon detector systems for quantum communication", *Light: Science & Applications* **4** e286 (2015).

[55] Lin, C.-H. *et al.*, "Metal-insulator-semiconductor photodetectors", *Sensors* **10** 10 (2010).

[56] Crouch, C. *et al.*, "Comparison of structure and properties of femtosecond and nanosecond laser-structured silicon", *Applied Physics Letters* **84** 11 (2004).

[57] Pengyu, F. *et al.*, "An invisible metal–semiconductor photodetector", *Nature Photonics* **6** 380 (2012).

[58] Lo, Y. *et al.*, "Silicon-nanowire detectors exhibit high sensitivity to ir light", *SPIE Newsroom* **October** 7 (2010).

[59] Zhang, A. *et al.*, "Ultrahigh responsivity visible and infrared detection using silicon nanowire phototransistors", *Nano Letters* **10** 6 (2010).

[60] Kalem, S. *et al.*, "Near-IR photoluminescence from si/ge nanowire-grown silicon wafers: effect of hf treatment", *Applied Physics A* **112** 3 (2013).

[61] Priolo, F. *et al.*, "Silicon nanostructures for photonics and photovoltaics", *Nature Nanotechnology* **9** 19 (2014).

[62] Irrera, A. *et al.*, "Quantum confinement and electroluminescence in ultrathin silicon nanowires fabricated by a maskless etching technique", *Nanotechnology* **23** 075204 (2012).

[63] Barbagiovanni, E. G. *et al.*, "Quantum confinement in si and ge nanostructures", *Journal of Applied Physics* **111** 3 (2012).

[64] Franzò, G. *et al.*, "Electroluminescence of silicon nanocrystals in mos structures", *Applied Physics A* **74** 1 (2002).

[65] Marigo, N., "The chinese silicon photovoltaic industry and market: a critical review of trends and outlook", *Progress in Photovoltaics: Research and Applications* **15** 2 (2007).

[66] Fraunhofer Institute for Solar Energy Systems, I. "Photovoltaics report", October, 20 (2016). https://www.ise.fraunhofer.de.

[67] Tian, B. *et al.*, "Coaxial silicon nanowires as solar cells and nanoelectronic power sources", *Nature* **449** 885 (2007).

[68] Segal, E. and Bussi, Y. "11 - semiconducting silicon nanowires and nanowire composites for biosensing and therapy". In *Semiconducting Silicon Nanowires for Biomedical Applications*. Woodhead Publishing (2014).

[69] Zheng, G. *et al.*, "Multiplexed electrical detection of cancer markers with nanowire sensor arrays", *Nature Biotechnology* **23** 10 (2005).

[70] Kneipp, K. *et al.*, "Single molecule detection using surface-enhanced Raman scattering (SERS)", *Physical Review Letters* **78** 1667 (1997).

[71] Fang, C. *et al.*, "Metallization of silicon nanowires and SERS response from a single metallized nanowire", *Chemistry of Materials* **21** 15 (2009).

[72] Sun, Y., "Silver nanowires - unique templates for functional nanostructures", *Nanoscale* **2** (2010).

[73] Qiu, T. *et al.*, "Surface-enhanced raman characteristics of ag cap aggregates on silicon nanowire arrays", *Nanotechnology* **17** 23 (2006).

[74] Mulazimoglu, E. *et al.*, "Enhanced localized surface plasmon resonance obtained in two step etched silicon nanowires decorated with silver nanoparticles", *Applied Physics Letters* **103** 143124 (2013).

[75] Li, C. P. *et al.*, "Silicon nanowires wrapped with au film", *The Journal of Physical Chemistry B* **106** 28 (2002).

[76] Zhang, M. L. *et al.*, "A high-efficiency surface-enhanced Raman scattering substrate based on silicon nanowires array decorated with silver nanoparticles", *Journal of Physical Chemistry C* **114** 5 (2010).

[77] Yasseri, A. *et al.*, "Growth and use of metal nanocrystal assemblies on high-density silicon nanowires formed by chemical vapor deposition", *Applied Physics A* **82** 659 (2006).

[78] Voss, R. F. *et al.*, "Percolation and fractal properties of thin gold films", *The Mathematics and Physics of Disordered Media: Percolation, Random Walk, Modeling and Simulation Lecture Notes in Mathematics. Berlin Heidelberg: Springer* **1035** 153 (1983).

[79] Piscanec, S. *et al.*, "Raman spectroscopy of silicon nanowires", *Physical Review B* **68**, 241312 (2003).

[80] Richter, H. *et al.*, "The one phonon Raman spectrum in microcrystalline silicon", *Solid State Communications* **39** 5 (1981).

[81] Campbell, I. H. *et al.*, "The effects of microcrystal size and shape on the one phonon Raman spectra of crystalline semiconductors", *Solid State Communications* **58** 10 (1986).

[82] Shao, M. *et al.*, "Nitrogen-doped silicon nanowires: synthesis and their blue cathodoluminescence and photoluminescence", *Applied Physics Letters* **95** 143110 (2009).

[83] Demichel, O. *et al.*, "Recombination dynamics of spatially confined electron-hole system in luminescent gold catalyzed silicon nanowires", *Nano Letters* **9** 2575 (2009).

[84] Guichard, A. R. *et al.*, "Temperature-dependent auger recombination dynamics in luminescent silicon nanowires", *Physical Review B* **78** 235422 (2008).

[85] Valenta, J. *et al.*, "Coexistence of 1d and quasi-0d photoluminescence from single silicon nanowires", *Nano Letters* **11** 3003 (2011).

[86] Irrera, A. *et al.*, "Size-scaling in optical trapping of silicon nanowires", *Nano Letters* **11** 4879 (2011).

[87] Artoni, P. *et al.*, "Temperature dependence and aging effects on silicon nanowires photoluminescence", *Optics Express* **20** 1483 (2012).

[88] Lo Faro, M. J. *et al.*, "A room temperature light source based on silicon nanowires", *Thin Solid Films* (2015).

[89] D'Andrea, C. *et al.*, "Silicon nanowires: synthesis, optical properties and applications", *Physica Status Solidi C* **11** 1622 (2014).

[90] Wu, Y. *et al.*, "Controlled growth and structures of molecularscale silicon nanowires", *Nano Letters* **4** 433 (2004).

[91] Cullis, A. G. *et al.*, "The structural and luminescence properties of porous silicon", *Journal of Applied Physics* **82** 909 (1997).

[92] Dal Negro, L. *et al.*, "Light emission efficiency and dynamics in silicon-rich silicon nitride films", *Applied Physics Letters* **88** 233109 (2006).

[93] Irrera, A. *et al.*, "Visible and infrared emission from Si/Ge nanowires synthesized by metal-assisted wet etching", *Nanoscale Research Letters* **74** 2 (2014).

[94] Hertel, T., "Carbon nanotubes: a brighter future", *Nature Photonics* **4** 77 (2010).

[95] Baughman, R. H. *et al.*, "Carbon nanotubes - the route toward applications", *Science* **297** 787 (2002).

[96] Hong, S. *et al.*, "Nanotube electronics: a flexible approach to mobility", *Nature Nanotechnology* **2** 207 (2007).

[97] Shu, Q. *et al.*, "Hybrid heterojunction and photoelectrochemistry solar cell based on silicon nanowires and double-walled carbon nanotubes", *Nano Letters* **9** 4338 (2009).

[98] Shu, Q. *et al.*, "Efficient energy conversion of nanotube/nanowire based solar cells", *Nature Nanotechnology* **46** 5533 (2010).

[99] Jorio, A. *et al.*, "Polarized Raman study of single-wall semiconducting carbon nanotubes", *Physical Review Letters* **85** 2617 (2000).

[100] O'Connell, M. J. *et al.*, "Band gap fluorescence from individual single-walled carbon nanotubes", *Science* **297** 593 (2002).

[101] Iijima, S. *et al.*, "Single-shell carbon nanotubes of 1-nm diameter", *Nature* **363** 603 (1993).

[102] Kataura, H. *et al.*, "Optical properties of single-wall carbon nanotubes", *Synthetic Metals* **103** 2555 (1999).

[103] Bachilo, S. M. *et al.*, "Structure-assigned optical spectra of single-walled carbon nanotubes", *Science* **298** 2361 (2002).

[104] Liu, C. *et al.*, "Tandem extraction strategy for separation of metallic and semiconducting swcnts using condensed benzenoid molecules effects of molecular morphology and solvent", *Nano Letters* **9** 2575 (2009).

[105] Liu, C. H. *et al.*, "Chemical approaches towards single-species single-walled carbon nanotubes", *Nanoscale* **2** 1901 (2010).

[106] Bonaccorso, F. *et al.*, "Density gradient ultracentrifugation of nanotubes: interplay of bundling and surfactants encapsulation", *Journal of Physical Chemistry C* **114** 17267 (2010).

[107] Li, Z. *et al.*, "Solubilization of single-walled carbon nanotubes using a peptide aptamer in water below the critical micelle concentration", *Langmuir* **31** 11 (2015).

[108] SouthWestNanoTechnology-SG76SWCNT. "http://www.swentnano.com".

[109] Weisman, R. B. *et al.*, "Dependence of optical transition energies on structure for single-walled carbon nanotubes in aqueous suspension: An empirical kataura plot", *Nano Letters* **3** 1235 (2003).

[110] Haroz, E. H. *et al.*, "Curvature effects on the E33 and E44 exciton transitions in semiconducting single-walled carbon nanotubes", *Physical Review B* **77** 125405 (2008).

[111] Lo Faro, M. J. *et al.*, "Silicon nanowire and carbon nanotube hybrid for room temperature multiwavelength light source", *Scientific Reports* **5** 16753 (2015).

[112] Dresselhaus, M. S. *et al.*, "Raman spectroscopy of carbon nanotubes", *Physical Review Letters* **409** 47 (2005).

[113] Dinh, L. N. *et al.*, "Optical properties of passivated si nanocrystals and siox nanostructures", *Physical Review B* **54** 5029 (1996).

[114] Lesne, A. and Lagues, M. *Scale Invariance: From Phase Transitions to Turbulence*. Springer, (2012).

[115] Brown, J. H. *et al.*, "The fractal nature of nature: power laws, ecological complexity and biodiversity", *Philosophical Transactions of the Royal Society of London B: Biological Sciences* **357** 1421 (2002).

[116] Smith, T. G. J. *et al.*, "Fractal methods and results in cellular morphology — dimensions, lacunarity and multifractals", *Journal of Neuroscience Methods* **69** 2 (1996).

[117] Mandelbrot, B., "How long is the coast of Britain? Statistical self-similarity and fractional dimension", *Science* **156** 3775 (1967).

[118] Krachmalnicoff, V. *et al.*, "Fluctuations of the local density of states probe localized surface plasmons on disordered metal films", *Physical Review Letters* **105** 183901 (2010).

[119] Laverdant, J. *et al.*, "Polarization dependent near-field speckle of random gold films", *Physical Review B* **77** (2008).

[120] Broadbent, S. R. *et al.*, "Percolation processes", *Mathematical Proceedings of the Cambridge Philosophical Society* **53** 03 (1957).

[121] Hammersley, J. M., "Percolation processes: Lower bounds for the critical probability", *The Annals of Mathematical Statistics* **28** 3 (1957).

[122] Smith, G. B. *et al.*, "Percolation in nanoporous gold and the principle of universality for 2D to hyperdimensional networks", *Physical Review B* **78** 165418 (2008).

[123] Andersson, T. G., "The initial growth of vapour deposited gold films", *Gold Bulletin* **15** 1 (1982).

[124] Smirnov, S. *et al.*, "Critical percolation in the plane: conformal invariance, cardy's formula, scaling limits", *Comptes Rendus de l'Académie des Sciences - Series I - Mathematics* **333** 3 (2001).

[125] Brasil, A. M. *et al.*, "Numerical characterization of the morphology of aggregated particles", *Aerosol Science* **32** 489 (2001).

[126] Mukai, T. *et al.*, "Radiation pressure forces of fluffy porous grains", *Astronomy and Astrophysics* **262** 1 (1992).

[127] Fazio, B. *et al.*, "Strongly enhanced light trapping in a two-dimensional silicon nanowire random fractal array", *Light: Science & Applications* **5** e16062 (2016).

[128] Karperien, A. "Fraclac is for digital image analysis". http://rsb.info.nih.gov/ij/plugins/fraclac/FLHelp/Introduction.htm. 1999-2013.

[129] Plotnick, R. E. *et al.*, "Lacunarity analysis: a general technique for the analysis of spatial patterns", *Physival Review E* **53** 5461 (1996).

[130] Bozzola, A. *et al.*, "Photonic light-trapping versus lambertian limits in thin film silicon solar cells with 1D and 2D periodic patterns", *Optics Express* **20** S2 (2012).

[131] Holmberg, V. C. *et al.*, "Optical properties of silicon and germanium nanowire fabric", *Journal of Physical Chemistry C* **116** 636 (2012).

[132] Mendes, M. J. *et al.*, "Broadband light trapping in thin film solar cells with self-organized plasmonic nano-colloids", *Nanotechnology* **26** 13 (2015).

[133] Mendes, M. J. *et al.*, "Plasmonic light enhancement in the near-field of metallic nanospheroids for application in intermediate band solar cells", *Applied Physics Letters* **95** 7 (2009).

[134] Podolskiy, V. A. *et al.*, "Giant optical responses in microcavity-fractal composites", *Laser Physics* **11** 26 (2001).

[135] Viani, F. *et al.*, "Design of a uhf rfid/gps fractal antenna for logistics management", *Journal of Electromagnetic Waves and Applications* **26** 4 (2012).

[136] Bruggemann, D. A. G. *et al.*, "Berechnung verschiedener physikalischer konstanten von heterogen substanzen", *Annals of Physics* **24** 636 (1935).

[137] Aspnes, D. E. *et al.*, "Dielectric functions and optical parameters of si, ge, gap, gaas, gasb, inp, inas, and insb from 1.5 to 6.0 ev", *Physics Review B* **27** 985 (1983).

[138] Huang, Y. F. *et al.*, "Improved broadband and quasi-omnidirectional anti-reflection properties with biomimetic silicon nanostructures", *Nature Nanotechnology* **2** 770 (2007).

[139] Kuga, Y. *et al.*, "Retroreflectance from a dense distribution of spherical particles.", *Journal of the Optical Society of America A* **8** 831 (1984).

[140] Van Albada, M. P. *et al.*, "Observation of weak localization of light in a random medium", *Physical Review Letters* **55** 2692 (1985).

[141] Wolf, P. E. *et al.*, "Weak localization and coherent backscattering of photons in disordered media", *Physical Review Letters* **55** 2696 (1985).

[142] Muskens, O. L. *et al.*, "Large photonic strength of highly tunable resonant nanowire materials", *Nano Letters* **9** 930 (2009).

[143] Stockman, M. I. *et al.*, "Inhomogeneous eigenmode localization, chaos, and correlations in large disordered clusters", *Physics Review E* **56** 6494 (1997).

[144] Waterman, P., "Symmetry, unitarity, and geometry in electromagnetic scattering", *Physics Review D* **3** 825 (1971).

[145] Borghese, F., "Multiple electromagnetic scattering from a cluster of spheres", *Aerosol Science and Technology* **3** 227 (1984).

[146] Borghese, F. *et al.*, "Scattering from model nonspherical particles", *2nd ed. Berlin Heidelberg: Springer-Verlag* (2007).

[147] Mishchenko, M. I., "Scattering, absorption, and emission of light by small particles", *Cambridge: Cambridge University Press* (2002).

[148] Wiersma, D. S. *et al.*, "Disordered photonics.", *Nature Photonics* **7** 188 (2013).

[149] Lagendijk, A. *et al.*, "Fifty years of anderson localization", *Physics Today* **62** 8 (2009).

[150] Savo, R. *et al.*, "Walk dimension for light in complex disordered media", *Physical Review A* **90** 2 (2014).

[151] Yoo, K. M. *et al.*, "Coherent backscattering of light from biological tissues", *Applied Optics* **29** 3237 (1990).

[152] Segev, M. *et al.*, "Anderson localization of light", *Nature Photonics* **7** 197 (2013).

[153] Sheng, P., "Introduction to wave scattering, localization and mesoscopic phenomena", *Springer* (2010).

[154] Riboli, F. *et al.*, "Engineering of light confinement in strongly scattering disordered media", *Nature Materials* **13** 720 (2014).

[155] Derode, A. *et al.*, "Dynamic coherent backscattering in a heterogeneous absorbing medium: Application to human trabecular bone characterization", *Applied Physics Letters* **87** 114101 (2005).

[156] Sahimi, M. *Heterogeneous Materials I - Linear Transport and Optical Properties*, volume 1. Springer, (2003).

[157] Gantmakher, V. F., "Electrons and disorder in solids", *Oxford University Press* **130** (2005).

[158] Maret, G. *et al.*, "Multiple light scattering from disordered media. the effect of brownian motion of scatterers", *Zeitschrift für Physik B Condensed Matter* **65** 4 (1987).

[159] Kuga, Y. *et al.*, "Retroreflectance from a dense distribution of spherical particles", *Optical Society of America A* **8** 831 (1984).

[160] Van Albada, M. P. *et al.*, "Observation of weak localization of light in a random medium", *Physical Review Letters* **55** 2692 (1985).

[161] Wiersma, D. S., "The physics and applications of random lasers", *Nature Physics* **4** 359 (2008).

[162] Cao, H. *et al.*, "Microlaser made of disordered media", *Applied Physics Letters* **76** 21 (2000).

[163] Muskens, O. L. *et al.*, "Broadband enhanced backscattering spectroscopy of strongly scatteringmedia", *Optics Express* **16** 2 (2008).

[164] Potton, R. J., "Reciprocity in optics", *Reports on Progress in Physics* **67** 5 (2004).

[165] Carminati, R. *et al.*, "Reciprocity, unitarity, and time-reversal symmetry of the $\boldsymbol{S}$ matrix of fields containing evanescent components", *Physical Review A* **62** (2000).

[166] Akkermans, E. *et al.*, "Coherent backscattering of light by disordered media: Analysis of the peak line shape", *Physical Review Letters* **56** 1471 (1986).

[167] Akkermans, E. *et al.*, "Theoretical study of the coherent backscattering of light by disordered media", *Journal de Physique France* **49** 77 (1988).

[168] Van der Mark, M. B. *et al.*, "Light scattering in strongly scattering media: Multiple scattering and weak localization", *Physical Review B* **37** 3575 (1988).

[169] Lenke, R. and Maret, G. *Multiple scattering of light: coherent backscattering and transmission. Scattering in polymeric and colloidal systems.* Amsterdam: Gordon and Breach, (2000).

[170] Peng, K. Q. *et al.*, "Dendrite-assisted growth of silicon nanowires in electroless metal deposition", *Advanced Functional Materials* **13** 127 (2003).

[171] D'Andrea, C. *et al.*, "Decoration of silicon nanowires with silver nanoparticles for ultrasensitive surface enhanced Raman scattering", *Nanotechnology* **27** 375603 (2016).

[172] Fazio, B. *et al.*, "Coherent backscattering of Raman light", *Nature Photonics* **12** 78 (2017).

[173] Beams, R. *et al.*, "Spatial coherence in near-field raman scattering", *Physical Review Letters* **113** 186101 (2014).

[174] Otto, A., "Theory of first layer and single molecule surface enhanced raman scattering", *Physica Status Solidi A* **188** 1455 (2001).

[175] Keresztury, G. *Introduction to the Theory and Practice of Vibrational spectroscopy.* John Wiley and Sons, (2002).

[176] Le Ru, E. C. and Etchegoin, P., "Principles of surface-enhanced Raman scattering", *Elsevier* (2007).

[177] Waldermann, F. C. *et al.*, "Measuring phonon dephasing with ultrafast pulses using raman spectral interference", *Physical Review B* **78** 155201 (2008).

[178] Loudon, R., "The Raman effect in crystals", *Advances in Physics* **13** 423 (1964).

[179] Yu, P. and Cardona, M., "Fundamentals of semiconductors", *Springer* (2010).

[180] Letcher, L. *et al.*, "Effects of high carrier densities on phonon and carrier lifetimes in si by time-resolved anti-stokes Raman scattering", *Applied Physics Letters* **90** 252104 (2007).

[181] Henry, A. S. *et al.*, "Spectral phonon transport properties of silicon based on molecular dynamics simulations and lattice dynamics", *Journal of Computational and Theoretical Nanoscience* **5** 1 (2008).

[182] Akkermans, E. & Montambaux, G., "Mesoscopic physics of electrons and photons", *Cambridge University Press* (2007).

[183] Raymond Ooi, C. H. *et al.*, "Theory of femtosecond coherent anti-stokes Raman backscattering enhanced by quantum coherence for standoff detection of bacterial spores", *Physical Review A* **72** 023807 (2005).

[184] Hokr, B. H. *et al.*, "Bright emission from a random Raman laser", *Nature Communications* **5** 4356 (2014).

[185] Zhang, M. L. *et al.*, "Preparation of large-area uniform silicon nanowires arrays through metal-assisted chemical etching", *Journal of Physical Chemistry C* **112** 4444 (2008).

[186] Scuderi, D. *et al.*, "Interaction of a laser-produced plume with a second time delayed femtosecond pulse", *Applied Physics Letters* **86** 071502 (2005).

[187] D'Andrea, C. *et al.*, "The controlled pulsed laser deposition of ag nanoparticle arrays for surface enhanced Raman scattering", *Nanotechnology* **20** 245606 (2009).

[188] Fazio, E. *et al.*, "Ag nanocluster synthesis by laser ablation in ar atmosphere: a plume dynamics analysis", *Laser and Particle Beams* **27** 281 (2009).

[189] Fazio, E. *et al.*, "Growth process of nanostructured silver films pulsed laser ablated in high-pressure inert gas", *Applied Surface Science* **255** 9676 (2009).

[190] Patrone, L. *et al.*, "Photoluminescence of silicon nanoclusters with reduced size dispersion produced by laser ablation", *Journal of Applied Physics* **87** 3829 (2000).

[191] Guzmán, M. G. *et al.*, "Synthesis of silver nanoparticles by chemical reduction method and their antibacterial activity", *International Scholarly and Scientific Research & Innovation* **2** 7 (2008).

[192] He, Y. *et al.*, "Silicon nanowires-based highly-efficient sers-active platform for ultrasensitive DNA detection", *Nano Today* **6** 2 (2011).

[193] Mie, G., "Contributions to the optics of turbid media, particularly of colloidal metal solutions", *Annals of Physics* **25** 377 (1908).

[194] Bohren, C. F. and Huffman, D. R., "Absorption and scattering of light by small particles", *Wiley, New York* (1983).

[195] Yang, X. *et al.*, "Ultrasensitive and recyclable sers substrate based on au-decorated si nanowire arrays", *Dalton Transactions* **42** 14324 (2013).

[196] Etchegoin, P. G. and Le Ru, E. C., "Basic electromagnetic theory of SERS", *Surface Enhanced Raman Spectroscopy: Analytical, Biophysical and Life Science Applications, Wiley* (2011).

[197] Galopin, E. *et al.*, "Silicon nanowires coated with silver nanostructures as ultrasensitive interfaces for surface-enhanced Raman spectroscopy", *ACS Applied Materials & Interfaces* **1** 7 (2009).

[198] Nie, S. *et al.*, "Probing single molecules and single nanoparticles by Surface-Enhanced Raman Scattering", *Science* **275** 1102 (1997).

[199] Le Ru, E. C. and Etchegoin, P., "Rigorous justification of the $|E|^4$ enhancement factor in surface enhanced Raman spectroscopy", *Chemical Physics Letters* **1423** 63 (2006).

[200] Moskovits, M., "Surface-enhanced spectroscopy", *Reviews of Modern Physics* **57** 783 (1985).

[201] Otto, A., "Surface-enhanced Raman scattering: 'classical' and 'chemical' origins", *Topics in Applied Physics, Springer-Verlag, Berlin* **4** (1984).

[202] Fazio, E. *et al.*, "SERS activity of pulsed laser ablated silver thin films with controlled nanostructure", *Journal of Raman Spectroscopy* **42** 1298 (2011).

[203] Kubin, R. *et al.*, "Fluorescence quantum yields of some rhodamine dyes", *Journal of Luminescence* **27** 4 (1982).

[204] Lu, R. *et al.*, "A 3D-SERS substrate with high stability: Silicon nanowire arrays decorated by silver nanoparticles", *CrystEngComm* **15** 6207 (2013).

[205] Shao, M. W. *et al.*, "Ag-modified silicon nanowires substrate for ultrasensitive surface enhanced Raman spectroscopy", *Applied Physics Letters* **93** 233118 (2008).

[206] Yang, Y. *et al.*, "Ag dendritic nanostructures for rapid detection of polychlorinated biphenyls based on surface-enhanced Raman scattering effect", *Journal of Applied Physics* **107** 044315 (2010).

[207] Kreibig, U. and Vollmer, M., "Optical properties of metal clusters", *Springer, Berlin* (1995).

[208] Hildebrandt, P. *et al.*, "Surface-enhanced Resonance Raman Spectroscopy of Rhodamine 6G adsorbed on colloidal silver", *Journal of Physical Chemistry* **88** 24 (1984).

[209] Kneipp, K. *et al.*, "Population pumping of excited vibrational states by spontaneous surface-enhanced Raman scattering", *Physical Review Letters* **76** 2444 (1996).

[210] Fazio, E. *et al.*, "Raman spectroscopy of organic dyes absorbed on pulsed laser deposited silver films", *Applied Surface Sci* **278** 259 (2013).

[211] Cottat, M. *et al.*, "High sensitivity, high selectivity SERS detection of MnSOD using optical nanoantennas functionalized with aptamers", *Journal of Physical Chemistry C* **119** 15532 (2015).

[212] Jiang, Z. Y. *et al.*, "Silicon-based reproducible and active surface-enhanced Raman scattering substrates for sensitive, specific and multiplex DNA detection", *Applied Physics Letters* **100** 203104 (2012).

[213] Xu, Z. *et al.*, "Large-area, uniform and low-cost dual-mode plasmonic naked-eye colorimetry and SERS sensor with handheld Raman spectrometer", *Nanoscale* **8** 6162 (2016).

# Curriculum Vitae

Maria José Lo Faro was born in Catania (CT) on September 8th, 1987.

**Education**

**Post-doc position**
at CNR-IPCF (Messina) since November 2016
Supervisor: Dr. A. Irrera

**PhD in Material Science & Nanotechnology**
at the University of Catania from November 2013 to November 2016
Thesis title: **Silicon Nanowires: the Route from Synthesis towards Applications**
Supervisors: Prof. F. Priolo, Dr. A. Irrera

**Visiting Research** at École Normale Supérieure (Paris)
working from February to June 2016 (during the PhD course)
at the Laboratoire Kastler-Brossel in the group of Prof. S. Gigan
Project: "*Wavefront-shaping & optical microscopy on Silicon nanowires light emission*" in the laboratories

2013 **Master Degree in Physics** [110/110] cum laude
at the University of Catania, dissertation entitled:
*"Innovative p-n coaxial junction based on Si nanowires"*
Supervisors: Prof. F. Priolo, Dr. A. Irrera, Dr. P. Musumeci

2011 **Bachelor Degree in Physics** [110/110]
at the University of Catania, dissertation entitled:
*"Microscopic & Nanoscopic imaging techniques"*
Supervisor: Prof. G. Piccitto

**Collaboration with the following institutions:**

- Matis CNR-IMM, Catania, Italy
- CNR-IPCF Messina, Italy
- Laboratoire Kastler-Brossel (ENS) Paris, France
- University of Bari, Chemistry Department, Italy
- University of Pavia, Physics Department, Italy

**Oral presentations:**

1. **Materials 2016 (CNSMI)**
   December 12-16th 2016, Aci Castello
   Symposium: *Solid state lightening and LEDs*

2. **European Material Research Society (E-MRS) - Spring meeting**
   May 1-6th 2016, Lille (France)
   Symposium DD: *Light interaction with nanomaterials*

3. **European Material Research Society (E-MRS) - Spring meeting**
   May 1-6th 2016, Lille (France)
   Symposium M: *Silicon compatible materials and integrated devices for photonics and optical sensing*

4. **Material Research Society (MRS) - Fall meeting**
   November 29th - December 4th 2015, Boston (US)
   Symposium P: *Synthesis and applications of nanowires and hybrid 1D-0D/2D/3D semiconductor nanostructures*

5. **Italian National Conference on Condensed Matter Physics (FISMAT)**
   September 28th - October 2nd 2015, Palermo
   Symposium: *Advanced Optical Materials*

6. **European Material Research Society (E-MRS) - Spring meeting**
   May 11-15th 2015, Lille (France)
   Symposium K: *Transport and photonics in group IV-based nanodevices*

7. **IEEE Nanotechnology Materials and Devices Conference (NMDS)**
   October 12-15 2014, Aci Castello
   Symposium: *Photonic materials and devices*

8. **Convegno Italiano delle Tecnologie Fotoniche (FOTONICA)**
   May 12-14 2014, Napoli
   Symposium B3: *Lighting*

**Poster presentations:**

---

1. **School on "Materials for Energy and Sustainability" (ISMES IV)**
   July 13-20th 2015, Golden (US)

2. **Microscopy Semiconducting Materials (MSM XIX)**
   March 29 - 2 April 2015, Cambridge (UK)

3. **International School "Materials for Renewable Energy"**
   July 12-18 2014, Erice

**School, lecture and congress participation:**

---

1. **International Conference on Enhanced Spectroscopy (ICES)**
   October 12-15th 2015, Messina

2. **Lectures on how to lunch a Start-up and contest participation**
   Project "GiftD" - 2014
   Scuola Superiore di Catania

3. **Lectures on "Nanoplasmonics & Nanophotonics"**
   Proff. Andreani, Galli - A.A. 2013-2014
   Scuola Superiore di Catania

4. **Corso di lezioni su "Project Management"**
   Proff. Stella, Puglisi - A.A. 2013-2014
   University of Catania

5. **Lectures on "Third generation organic dye PV cells based"**
   Dott.ssa La Ganga - A.A. 2013-2014
   University of Catania

# List of publications

Research performed within this PhD course resulted in the following publications:

1. **Coherent backscattering of Raman light**
   B. Fazio, A. Irrera, S. Pirotta, C. D'Andrea, S. Del Sorbo, **M. J. Lo Faro**, P. Gucciardi, M. A. Iatì, R. Saija, M. Patrini, P. Musumeci, C. Vasi, D. S. Wiersma, M. Galli, F. Priolo
   Nature Photonics, in press
   DOI: 10.1038/nphoton.2016.278

2. **Strongly enhanced light trapping in a two-dimensional random fractal array of silicon nanowires**
   B. Fazio, P. Artoni, M. A. Iatì, C. D'Andrea, **M. J. Lo Faro**, S. Del Sorbo, S. Pirotta, P. Gucciardi1, P. Musumeci, C. Vasi, R. Saija, M. Galli, F. Priolo, A. Irrera
   Light: Science & Applications, Vol. 5, e16062 (2016)
   DOI: 10.1038/lsa.2016.62

3. **Silicon nanowires and carbon nanotubes hybrid for room temperature multiwavelength light source**
   **M. J. Lo Faro**, C. D'Andrea, E. Messina, B. Fazio, P. Musumeci, R. Reitano, G. Franzò, P. Gucciardi, C. Vasi, F. Priolo, F. Iacona, A. Irrera
   Scientific Reports, Vol. 5, 16753 (2015)
   DOI: 10.1038/srep16753

4. **Decoration of silicon nanowires with silver nanoparticles for ultrasensitive surface enhanced Raman scattering**
   C. D'Andrea, **M. J. Lo Faro**, G. Bertino, P. M. Ossi, F. Neri, S. Trusso, P. Musumeci, M. Galli, N. Cioffi, A. Irrera, F. Priolo, B. Fazio
   Nanotechnology, Vol. 27, n. 37, p.375603 (2016)
   DOI:10.1088/0957-4484/27/37/375603

5. **A room temperature light source based on silicon nanowires**
   **M. J. Lo Faro**, C. D'Andrea, E. Messina, B. Fazio, P. Musumeci, G. Franzò, P. Gucciardi, C. Vasi, F. Priolo, F .Iacona, A. Irrera
   Thin solid Films, Vol. 613, pp. 59-63 (2015)
   DOI:10.1016/j.tsf.2015.11.028

6. **Functionalization of silicon nanowire arrays by silver nanoparticles for the laser desorption ionization mass spectroscopy analysis of vegetable oils**
   R. A. Picca, C. D. Calvano, **M. J. Lo faro**, B. Fazio, S. Trusso, P. M. Ossi, F. Neri, C. D'Andrea, A. Irrera, N. Cioffi
   Journal of Mass Spectrometry, Vol. 51, n. 9, pp.849-856 (2016)
   DOI:10.1002/jms/3826

7. **Silicon nanowires: synthesis, optical properties and applications**
   C. D'Andrea, **M. J. Lo Faro**, P. Musumeci, B. Fazio, F. Iacona, G. Franzò, P. Gucciardi, C. Vasi, F. Priolo, A. Irrera
   Physica Status Solidi C, Vol. 11, n.11-12, pp. 1622-1625 (2014)
   DOI: 10.1002/pssc.201400052

8. **Metal-decorated silicon nanowires for laser desorption-ionization mass spectrometry**
   N. Cioffi, R. A. Picca, **M. J. Lo Faro**, C. D. Calvano, B.Fazio, M. C. Sportelli, S. Trusso, P. M. Ossi, F. Neri, C. D'Andrea, A. Irrera
   SPIE Newsroom, 18 September (2015)
   DOI: 10.1117/2.1201509.006086

9. **Nanowires di silicio. Promotori per LDI-MS**
   R. A. Picca, C. D. Calvano, M. C. Sportelli, C. D'Andrea, **M. J. Lo Faro**, B. Fazio, A. Irrera, N. Cioffi
   La Chimica e L'industria (2014)

**Outcoming publications**

10. **Silicon nanowires: Synthesis, structural properties and photonic applications**
    A. Irrera, **M. J. Lo Faro**, C. D'andrea, B. Fazio, R. A. Picca, N. Cioffi, S. Trusso, G. Franzò, P. Musumeci, F. Priolo, F.Iacona
    Semiconductor Science and Technology - Invited Topical Review, submitted

11. **Selective label-free photoluminescence biosensor based on silicon nanowires**, submitted

12. **Copper Iodide & Silicon nanowires solar cell**
    M. J. Lo Faro et al., submitted

# Acknowledgments

I would like to express a special thanks to my supervisors Prof. Francesco Priolo and Dr. Alessia Irrera who welcomed me in their group, you have been amazing mentors for me and I am really grateful to you both for giving me such opportunity.

I owe a special appreciation to Dr. Paolo Musumeci, for his scientific and specially non-scientific advice, help and encouragements, thank you for all our uncountable moments. A special acknowledgment goes to my closest friends and collaborators Dr. Cristiano D'andrea and Dr. Antonio Leonardi who assisted me during experiments and thought me how to work in an amazing research team.
During this PhD Alessia gave me the opportunity to collaborate both with Matis IMM CNR of Catania and IPCF CNR of Messina. It wasn't always easy for me to be here and there at the same time, but I really feel honored about the interaction with all the researchers, the administrative and technician staff of the two groups. I wish to thank you all for your precious support, I would have been lost without it and I truly apologize for the stalking times.

I am particularly grateful to Prof. Tony Terrasi for his teaching and the great time we shared together; to Dr. Fabio Iacona for his advice and valuable remarks; to Prof. Riccardo Reitano, Dr. Maria Miritello and Dr. Giorgia Franzò for optical characterizations and stimulating discussions; to Dr. Lucia Romano, Prof. Salvo Mirabella for the RBS knowledge and their assistance; to Dr. Francesco Ruffino, Dr. Giacomo Torrisi and Dr. Antonella Gentile for sputtering support; to Dr. Manuel Mendes for the tips and tricks he shared with me and specially for the time passed together in the lab.

I wish to thank all the researchers of the Matis IMM CNR group that I didn't mentioned before for all the encouragement, the knowledge and the time we shared together in these past years. Thanks to all my colleagues Cristiano, Antonio, Giulia, Adriana, Gabriele, Manuel, Seweryn, Paolo, Ruy, Guillaume, Stefano, Antonella, Vicky, Giacomo, Maria, Eric & Enrica, Viviana, Giuseppe, Marta, Daniele, Simona and Saro with whom I shared a lot of funny and crazy moments and who were always there during these years.

I cannot avoid thanking Dr. Primo Furno, Giusy Schillaci and Patrizia Pappalardo for their excellent work and the friendship they showed me (evviva i mulingiana party).
I wish to thank Prof. Nicola Cioffi and his team of the University of Bari for all the measurements and the ongoing collaboration.

I would like to express all my gratitude to the CNR IPCF Director Dr. Cirino Vasi for who gave me the opportunity to work in his institute labs, side by side with his team of incredibly experienced researchers. I also very grateful to him for his availability. The interaction with all the CNR IPCF researchers allowed me to grow as a scientist and improved my level of knowledge. Thank you for your scientific advice as well as life ones, they were important to me.

To Alessia Irrera I owe all my gratitude, the knowledge and the years of effort she devoted me are far beyond any expression. You were always there, guiding and teaching me in every step of this PhD experience and making me feel a part of your family. I will be always grateful to you for sharing with me your research skills, your brilliant ideas and specially for the precious life lessons you though me. I cherish all those unforgettable working and non-working moments spent together and promise to use your teaching for what has yet to come.

I also owe my gratitude to Dr. Barbara Fazio for her friendship and for sharing with me her incredible knowledge on Raman, light scattering and optical setup. Dr. Cristiano D'Andrea thought me all about spectroscopy, thank you for your patience and support. My special appreciation Dr. Nello Trusso for sharing his experience on deposition processes with me, I enjoyed working in the lab with you. I thank all the members of the Nanosoftlab group, in particular Dr. Onofrio Maragò, Dr. Antonella Iatì, Dr. Maria Grazia Donato and Dr. Pietro Gucciardi for the valuable discussions and the lunches shared together. A special mention to Dr. Gaetano Di Marco and Dr. Pino Calogero for the uncountable support and availability. I can honestly say that I've been your crux and delight, thank you for the patience, all the measurements and the chemistry lessons. I cannot forget the one who endorsed me with a cosmic superpower and who probably had the strongest influence on my character after Alessia, thank you Dr. Princi for your school of life and precious technological support. I am deeply grateful to Nino, Elena, Donatella, Viviana, Nancy, Sebastiano and Alessandro for their friendship and help. I am also thankful to all the CNR IPCF Direction and administrative staff for their availability and clever work, specially Giovanna Toscano for her guidance in bureaucratic matter, her friendship, the shared love for animals and her amazing cooking. Last but not at all least, I owe my research work to the excellent technician staff of both IMM and IPCF CNR groups, many thanks to Carmelo Percolla, Giuseppe Pantè, Salvo Tatì, Giuseppe Lupò, Pippo Gismondo, Pippo Spinella and to Mimmo D'arrigò for your technical help, I shared with you my best moments.
A special thanks to Carmelo Percolla, the evaporator is still working only because of you. I really value your experienced knowledge and treasure your lesson on the evaporator that we almost unmounted pieces by pieces once. A final appreciation to Mimma, for the kindness she demonstrated me day by day.
The new e-beam evaporator/sputtering system bought from Kenosistec improved the samples productivity of my research activity. I acknowledge the experties of all the Kenosoistec staff, specially for Giovanni Barbieri, Simone Colucci, Carlo Aliberti and Fiorenzo Ammendola for their availability and support.

I am specially indebted to Prof. Sylvain Gigan for his availability, scientific advice and above all your happiness and kindness.
Many thanks to his collaborators Dr. Giorgio Volpe, Dr. Samuel Grésillon and Dr. Romolo Savo for the scientific discussion and help, I really learned a lot through assistance. All my gratitude goes to the Gigan team who welcomed me in the LKB lab: Baptiste, Mickael, Markus, Tengfei, Jonathan, Tom, Romolo, Thomas, Hugo, Ulisse and Antoine for the patience, the knowledge and the friendship they demonstrated me.

During the time spent in Paris I met a lot of incredible people who stayed by my side, some of them visited me during the summer and I thank them all, in particular the C7 survivors Yoon Seok and Hannah, my B5 friends Laura, Natacha, Mendes, Maro and all the other guys for their friendship, the valuable scientific discussions and the shared vision of game of throne! You all showed me that I have a lot to work on to improve myself. I cannot avoid thanking all those people I met during schools and conferences that are now important to me, specially Kaki & Doug, Nathan "the allumina dancer" and Aaron the Daddy :) hope to see you soon.
Vorrei ringraziare di cuore tutti i miei colleghi ed amici che ci sono sempre stati da ogni parte del mondo, specialmente Franco, Alessandro, Simona Filice, Adriana, Valentina e specialmente Martina, la mia amica di tutta una vita. Grazie a tutte le mie compagne di GAG e Fit, Cinzia, Evelyn, Veronica, soprattutto grazie alla mia patata Glenda che è mitica. Doveroso ringraziare Teresa che ormai da 3 anni e mezzo mi dona i più bei momenti di relax attraverso estrenuanti fatiche, ma la adoro sempre.
Ringrazio ancora la mascotte del nostro gruppo, Sofia, per la sua affettuosità e per il tempo trascorso insieme che mi ha fatto rivivere i bei momenti della mia infanzia.

Infine non ho parole per ringraziare la mia famiglia, anche se non ve lo dimostro abbastanza vi voglio un gran bene.

Grazie alla mia Mamma, al mio Papino, al mio fratellino ed al mio Amino, grazie della pazienza, dell'onnipresente supporto e del vostro affetto:
"Possiamo non avere tutto insieme, ma insieme abbiamo tutto".
Sono fortunata ad avere questa grande famiglia che mi supporta e sostiene sempre, grazie a tutti gli Zii e Zie, alla mia famiglia acquisita Salvo, Sergio, Gildo, Mauri, Hao ed infine Salvo B. Grazie alle persone che mi hanno amata e che oggi non ci sono più, papà Francesco e la mia Nonnina. Grazie ancora alle persone che non ho menzionato ma che in qualche modo mi hanno portato ad essere la persona che sono oggi.
Dulcis in fundo ringrazio Manuele che c'è sempre stato, la distanza è relativa ma il nostro amore è reale, quindi infinito.